

# **Tailoring Critical Wave Sequences for Response-Based Design**

vorgelegt von  
Diplom-Ingenieur  
Marco Klein  
aus Berlin

Von der Fakultät V - Verkehrs- und Maschinensysteme  
der Technischen Universität Berlin  
zur Erlangung des akademischen Grades

Doktor der Ingenieurwissenschaften  
- Dr.-Ing. -

genehmigte Dissertation

Promotionsausschuss:

Vorsitzender: Prof. Dr.-Ing. Andrés Cura Hochbaum  
Berichter: Prof. Dr.-Ing. Günther F. Clauss  
Berichter: Prof. Dr.-Ing. Paul Uwe Thamsen

Tag der wissenschaftlichen Aussprache: 27.04.2015

Berlin 2015

D 83



## Acknowledgement

This thesis is based on my research activity for the project EXTREME SEAS at the Ocean Engineering Division at Technische Universität Berlin. I wish to express my gratitude to all the people who encouraged me to research on this topic and supported me over the last years.

Special thanks go to my promoter and supervisor Prof. Dr.-Ing. Günther F. Clauss. His expertise and enthusiasm inspired me. I appreciate very much the cooperation over the last years which are characterized by great freedom in my research work as well as excellent technical and personal support. Many thanks also to my second promoter Prof. Dr.-Ing. Paul Uwe Thamsen who took time and interest in my work as well as to the chairman of the doctoral committee, Prof. Dr.-Ing. Andrés Cura Hochbaum.

I would like to thank my colleagues from the Ocean Engineering Division for a uniquely cooperative and pleasant working atmosphere. In particular, Christian Schmittner who aroused my interest for research in the field of ocean engineering. In addition, I would like to thank Matthias Dudek, Sascha Kosleck, Florian Sprenger for countless valuable discussions, support of my research and last but not least for the friendship. Special thanks go to Kornelia Tietze for all the administrative support she gave to me – I am greatly indebted to her. I appreciate the cooperation with our technical staff, namely Manfred Bernt, Haiko de Vries, Karsten Kowalski and Peter Longerich, who prepared and supported the model tests. Special thanks also to the team of student research assistants for their support during the model testing series and preparation of the results.

The European Commission is appreciated for funding the research project Extreme Seas, under the Grant agreement no. 234175. In this context, I would like to thank the project partners for outstandingly successful cooperation and, especially, Dr. Elzbieta M. Bitner-Gregersen for coordinating the project. In addition, I would like to thank Prof. Carlos Guedes Soares for being the technical coordinator of the project as well as for the friendly cooperation for many years. Special thanks go to Miguel Onorato for the pleasant and fruitful teamwork, who was always willing to share his expertise. I will never forget his enthusiastic happiness as the very first breather-type freak wave has been reproduced in our seakeeping basin.

But I owe the greatest debt of gratitude to my beloved wife Jessica, who is always on my side for better or worse. I appreciate very much her interest and support for my research which provided the indispensable basis for this thesis. Last but not least, I thank my parents Edeltraud and Paul for their imperturbable belief in me as well as my older brother Stephan.



## **Abstract**

What is the worst case scenario offshore structures are exposed to during their lifetime – the highest rogue wave or a wave group of certain frequency?

The choice of such environmental design conditions, to be considered in the design process, is a delicate question. Reliability criteria, such as operation in moderate sea states as well as survival in extreme conditions, are typically linked with a design wave (group), limiting characteristic sea state or a rogue wave. Thereby, operational efficiency and survival are complementing characteristics for offshore structures to be carefully balanced in the design process. The identification of environmental design conditions for the assessment of offshore structures is still a key issue.

In this thesis, two innovative concepts in the field of tailoring critical wave scenarios for response-based design are presented. Intention of this work is to develop efficient methods for the deterministic identification and evaluation of critical design conditions. The first concept comprises the application of analytical breather solutions of the non-linear Schrödinger-type equation as innovative experimental design freak waves. The second concept, a response-based identification tool, is developed as a new design wave concept for the deterministic identification of critical wave sequences and responses, respectively.

The breather solutions offer the fast generation of freak waves of certain frequency and are intended as “one for all” critical design wave sequence in terms of an outstanding situation to be investigated for any kind of offshore structure. The general applicability of breather solutions, the formation process and characteristics are firstly determined and reviewed against the “New Year Wave”, a classical real-world freak wave. The potential span of application is demonstrated by integrating the breather solution into an irregular sea state, resulting in a freak wave (at target location) within a random wave field. Hereupon, this new class of freak waves is for the first time used in sea-keeping tests showing that the breather solutions might provide new perspectives in the methodology of examining marine structures against rogue waves.

The response-based identification tool offers the identification and evaluation of critical design conditions addressing particular design questions of specific offshore structures, i.e. the obtained wave sequences represent outstanding situations for particular offshore structures and system responses. The basic principle of this procedure is characterized by deterministic tailoring of short wave sequences to obtain a certain maximum response level. Two typical design examples are presented: The first application addresses extreme ship response in terms of the maximum vertical

---

wave bending moment of a chemical tanker and the second application deals with a multi-body offshore operation in terms of an offshore LNG transfer system. The objective of both applications is to identify wave sequences which lead to a critical response value for a certain design sea state. The obtained results are reviewed against classical design wave concepts and validated by experiments.

## Zusammenfassung

Ist die größte Welle die gefährlichste oder eine Wellengruppe in einem für die Struktur ungünstigen Frequenzbereich? Die Identifizierung von Worst-Case-Szenarien beim Entwurf von meerestechnischen Konstruktionen stellt eine große Herausforderung dar und kann nicht global beantwortet werden, da verschiedene Entwurfskriterien (limitierende Körperbewegungen, lokale oder globale Belastungen) und Operationszustände (Transit, Operation, Survival) zu unterschiedlichen Ergebnissen hinsichtlich der kritischen Wellensequenzen führen werden. Bereits in der Planungsphase sollten diese entwurfskritischen Wellensequenzen identifizierbar sein, wobei numerische Simulationen durch maßgeschneiderte Modellversuche zu validieren sind.

Diese Arbeit präsentiert zwei innovative Entwurfswellenkonzepte für die deterministische Identifizierung und Evaluierung kritischer Seegangszustände, die eine extreme Systemantwort der meerestechnischen Struktur zur Folge haben. Das erste Konzept führt die sogenannten Breather-Lösungen der nichtlinearen Schrödinger Gleichung als maßgeschneiderte Extremwellen im Entwurfsprozess ein. Das zweite Entwurfswellenkonzept ist ein vollständig automatisierter antwortbasierter Identifizierungsalgorithmus zur deterministischen Ermittlung kritischer Seegangszustände.

Die Breather-Lösungen ermöglichen eine schnelle Erzeugung von Extremwellen beliebiger Wellenlängen, wodurch sie auf die zu untersuchende meerestechnische Struktur maßgeschneidert werden können. Gleichzeitig können beliebige maximale Wellenhöhen bis zur physikalischen Wellenbrechgrenze justiert werden. Aufgrund ihrer flexiblen Anwendbarkeit stellen die Breather-Lösungen eine universelle Entwurfswelle für jegliche meerestechnische Konstruktion dar, um die Auswirkungen von Extremwellen systematisch untersuchen zu können. Die versuchstechnische Anwendbarkeit der analytischen Breather-Lösungen, deren Ausbreitungsverhalten und kinematische bzw. dynamische Eigenschaften werden als erstes ermittelt und im Vergleich zur „New Year Wave“, einer im natürlichen Seegang registrierten Extremwelle, begutachtet. Das große versuchstechnische Potenzial der Breather-Lösungen wird durch die Integration eines Breathers in einen zufälligen irregulären Seegang herausgestellt. Abschließend werden mit dieser neuen Klasse von Extremwellen zum ersten Mal Seegangsversuche zur systematischen Analyse der Welle-Struktur-Wechselwirkung durchgeführt.

Der antwortbasierte Identifizierungsalgorithmus ermöglicht die deterministische Identifizierung und Analyse von kritischen Seegangszuständen hinsichtlich spezifischer Entwurfskriterien. Die ermittelten kritischen Wellensequenzen stellen somit

---

ungünstige bzw. gefährliche Situationen für die zu untersuchende meerestechnische Konstruktion und deren Strukturantwort dar. Das Grundprinzip der Methode beruht auf der Kombination von (beliebigen) Welle-Struktur-Analyseprogrammen mit einem Optimierungsalgorithmus, um maßgeschneidert die vordefinierte kritische Systemantwort und somit die zugrunde liegende Wellensequenz zu ermitteln. Um den großen Anwendungsbereich des Verfahrens zu demonstrieren, werden zwei typische Anwendungsbeispiele präsentiert. Das erste Anwendungsbeispiel befasst sich mit der maximalen Schiffsantwort am Beispiel des vertikalen Biegemomentes eines Chemietankers. Das zweite Beispiel adressiert den LNG Transfer zwischen einer Terminal Barge und einem LNG Tanker als Mehrkörperproblem. Die Ergebnisse werden denen klassischer Entwurfsverfahren gegenübergestellt und kritisch bewertet. Die Untersuchungen beinhalten umfassende numerische Analysen sowie deren Validierung durch gezielte Modellversuche.

# Contents

<b>Abstract</b>	<b>iii</b>
<b>Zusammenfassung</b>	<b>v</b>
<b>List of Figures</b>	<b>x</b>
<b>List of Tables</b>	<b>xi</b>
<b>1. Introduction</b>	<b>1</b>
<b>2. Water Wave Problem</b>	<b>9</b>
2.1. Potential Flow . . . . .	9
2.2. Stokes Wave Theory . . . . .	11
2.3. Standard Model of Ocean Waves . . . . .	12
2.3.1. Statistical Analysis . . . . .	16
2.3.2. Wave Generation . . . . .	18
2.4. Non-Linear Schrödinger-Type Equation . . . . .	22
2.4.1. Envelope Soliton Solution . . . . .	24
2.4.2. Breather Solutions . . . . .	25
2.5. WAVETUB . . . . .	30
<b>3. Extreme Waves</b>	<b>33</b>
3.1. New Year Wave . . . . .	34
3.2. Breather Solutions . . . . .	40
3.3. New Year Wave vs. Breather Solution . . . . .	51
3.4. Tailored Breather Solution . . . . .	56
<b>4. Wave-Structure-Interaction</b>	<b>59</b>
4.1. Hydrodynamic Analysis . . . . .	60
4.1.1. Hydrodynamic Transparent Structures . . . . .	61
4.1.2. Hydrodynamic Compact Structures . . . . .	61
4.2. WAMIT . . . . .	62
4.3. IST Code . . . . .	63
4.4. Standard Model of Offshore Structure Response . . . . .	64
4.4.1. Stochastic Frequency Domain Investigations . . . . .	65
4.4.2. Deterministic Time Domain Investigations . . . . .	67
4.5. Design Wave Concepts . . . . .	67

<b>5. Extreme Responses</b>	<b>71</b>
5.1. Breather-Type Freak Waves as Experimental Design Waves . . . . .	71
5.2. Response-Based Identification Tool . . . . .	76
5.2.1. Extreme Ship Response . . . . .	78
5.2.2. Multi-Body Offshore Operation . . . . .	86
<b>6. Conclusions</b>	<b>99</b>
<b>Bibliography</b>	<b>102</b>
<b>List of Abbreviations</b>	<b>115</b>
<b>Nomenclature</b>	<b>117</b>
<b>A. Test Facilities</b>	<b>125</b>
A.1. Seakeeping Basin at TUB . . . . .	125
A.1.1. Multi-Body Offshore Operation . . . . .	125
A.1.2. Chemical Tanker . . . . .	125
A.2. Seakeeping Basin at CEHIPAR . . . . .	130
<b>B. Derivation of the Non-Linear Schrödinger-Type Equation</b>	<b>131</b>

## List of Figures

2.1.	Definition of the coordinate system. . . . .	10
2.2.	Breaking wave height and regions of validity of various gravity water waves theories. . . . .	12
2.3.	Standard model of ocean waves. . . . .	14
2.5.	Envelope of the Akhmediev breather in time and space. . . . .	26
2.6.	Envelope of the Kusnetzov-Ma breather in time and space. . . . .	27
2.7.	Envelope of the Peregrine breather in time and space. . . . .	28
2.8.	Higher-order Akhmediev-Peregrine breather. . . . .	29
2.9.	Illustration of the mathematical model of WAVETUB. . . . .	31
3.1.	Comparison of the measured model wave train at target location and the New Year Wave sequence recorded at the Draupner platform. . . . .	34
3.2.	Schematic sketch of the experimental setup. . . . .	35
3.3.	Spatial development of the New Year Wave. . . . .	36
3.4.	Progress of the wave heights and velocity-dependent development of the wave crests. . . . .	37
3.5.	Progress of the mean energy. . . . .	39
3.6.	Energy envelope of the wave group. . . . .	40
3.7.	Theoretical Kusnetzov-Ma breather development in time and space. . . . .	41
3.8.	Formation of the highest wave. . . . .	43
3.9.	Development of different Kusnetzov-Ma breathers. . . . .	45
3.10.	WAVETUB vs. Experiment. . . . .	47
3.11.	WAVETUB results for the three carrier frequencies with the smallest initial steepness. . . . .	48
3.12.	WAVETUB results for the $T_c = 1.4s$ breather with the smallest initial steepness. . . . .	50
3.13.	New Year Wave vs. Peregrine breather. . . . .	51
3.14.	Horizontal particle velocity of New Year Wave and Peregrine breather. . . . .	53
3.15.	Dynamic pressure of New Year Wave and Peregrine breather. . . . .	54
3.16.	Horizontal velocity and dynamic pressure profile under New Year Wave crest and Peregrine breather wave crest. . . . .	55
3.17.	Integration of a Peregrine breather into an irregular sea state. . . . .	57
3.18.	Comparison between the real-world New Year Wave and the tailored Peregrine breather at target location. . . . .	57
4.1.	Standard model of offshore structure response. . . . .	65
4.2.	Examples of design wave concepts. . . . .	70
5.1.	Model test results of the breather-type freak wave investigations. . . . .	73

5.2.	Comparison of the experimental results in breather-type freak waves and the New Year Wave. . . . .	75
5.3.	General scheme of the new critical design wave concept. . . . .	76
5.4.	Initial input: JONSWAP energy density spectrum. . . . .	79
5.5.	Progress of the objective function. . . . .	80
5.6.	Optimization results. . . . .	82
5.7.	Optimized critical wave sequence vs. MLER/MLRW pendant. . . . .	83
5.8.	Results of the random phase realizations. . . . .	84
5.9.	Results of the random phase realizations compared to the optimization results. . . . .	85
5.10.	Comparison of model test results and numerical simulations. . . . .	86
5.11.	The <i>MPLS20</i> concept: Turret moored terminal barge and a shuttle carrier in tandem configuration. . . . .	87
5.12.	RAO of the relative vertical motion. . . . .	89
5.13.	Operational range for the multi-body offshore system at the location Haltenbanken (Norwegian Sea). . . . .	90
5.14.	Critical Wave Episode. . . . .	91
5.15.	Result of the phase distribution optimization. . . . .	93
5.16.	Result of the response-based identification tool. . . . .	96
5.17.	Comparison of the identified critical wave sequences. . . . .	97
5.18.	Comparison between numerical calculations and measurements. . . . .	98
A.1.	TUB seakeeping basin. . . . .	126
A.2.	Model test setup of the multi-body offshore system. . . . .	127
A.3.	Model test setup of the chemical tanker model. . . . .	127
A.4.	Suspension system test in regular waves. . . . .	129
A.5.	Suspension system test in irregular waves. . . . .	129
A.6.	CEHIPAR seakeeping basin. . . . .	130

## **List of Tables**

2.1. Linear superposition method of field variables for natural seaways. . .	15
3.1. Summary of the main characteristics of the three freak waves. . . . .	38
3.2. Overview of the investigated parameters of the Kusnetzov-Ma breather solution. . . . .	42
3.3. Properties of the measured breather-type freak waves. . . . .	44
5.1. Overview of the parameter used for the optimization procedure. . .	80
A.1. Main Dimensions of the LNG Carrier and the Terminal. . . . .	128
A.2. Main Dimensions of the Chemical Tanker. . . . .	128



## 1. Introduction

Offshore structures are exposed to harsh wave environments causing short-term (e.g. peak loads in extreme conditions) as well as long-term effects (e.g. fatigue during lifetime) to be considered in the design process. This thesis focusses exclusively on short-term wave events leading to a critical situation in terms of structure response. All aspects are affected – from efficient and economic operation in moderate sea states to survival in extreme conditions. The precise identification of such critical situations is indispensable for the complete evaluation of the design. Main objective is the identification of the maximum response to be considered in the design of the structure as well as the determination of the applicability and annual downtime, respectively.

For the evaluation of offshore structures, simple and fast linear to fully non-linear methods are available. The computational time needed per simulation increases significantly with increasing complexity of the applied numerical method, limiting a holistic application at an advanced level up to now. As a consequence, the most commonly used methods are based on linear transfer functions as this is an efficient procedure for the fast holistic evaluation of a design. In particular, the linear stochastic analysis enables the fast evaluation of the operability of a design for certain sea areas. This is an important benchmark for offshore structures which are forced to work in defined sea areas without the possibility of bad weather avoidance.

### Design Wave Concepts

Extreme conditions such as critical wave sequences leading to an extreme response value are particularly challenging. The fundamental question is the identification of the underlying critical wave group to be considered for detailed investigation.

Different approaches are introduced for the deterministic identification of critical (design) wave sequences. Torhaug et al. (1998) introduced the Critical Wave Episode (CWE) approach where the maximum linear response is determined for a set of irregular sea states with random phase distributions. The wave sequences which lead to the highest response within an irregular sea state are called CWE. Afterwards, a set of CWE's, the mean of several CWE's or the CWE leading to the maximum response are used for non-linear simulations for extreme value estimation. More accurate and sophisticated methods are based on conditioning of the wave sequence and response, respectively, using probabilistic analysis. These wave sequences are obtained by linear conditioning of short wave sequences leading to a predefined maximum response which are also subsequently used for detailed non-linear investigations. The predefined response is commonly inferred

from linear short-term or long-term statistics. These methods allow the estimation of extremes of the non-linear response statistics by performing only short non-linear simulations with the identified wave sequences. In doing so, the fundamental assumption is that the non-linear response is only a correction of the linear response. Tromans et al. (1991) presented a New Wave model based on the standard model of ocean waves, which has been extended by Friis-Hansen and Nielsen (1995). The most probable wave crest elevation, also called Most Likely storm Wave (MLW profile), is determined by conditioning the amplitudes and phases based on probabilistic analysis. Applying the MLW approach on the response spectra instead of wave spectra results in the Most Likely Extreme Response (MLER) concept (Adegeest et al., 2000), leading to the underlying Most Likely Response Wave (MLRW) (Adegeest et al., 2000; Dietz, 2004). Combining the MLRW profile with an irregular random background wave will produce the Conditional Random Response Wave (CRRW) (Dietz, 2004). Alford (2008) introduced a different approach which basically manipulates the phases of the linear response spectrum by means of optimizing procedures to obtain linear extreme values in the early design stage.

However, the development of design wave concepts is still under research and the introduced concepts based on linear theory should be validated under different severe conditions when non-linear effects are significant (Drummen et al., 2009).

## Freak Waves

Freak waves are outstanding events for any kind of offshore structure and are, therefore, of particular interest. The most famous freak wave in history is the so-called “New Year Wave” (NYW). The NYW was registered in the North Sea at the Draupner jacket platform on January 1<sup>st</sup>, 1995 (Haver and Anderson, 2000). The measurement of this extraordinarily high single wave, which had been dismissed as cock-and-bull story before, removed any doubt regarding the existence of freak waves. This considerably attributed to its prominent position in the ocean engineering community. Freak wave observation and occurrence, respectively, had already been discussed before (Kjeldsen, 1990; Sand et al., 1990), but the giant single wave, measured at the Draupner platform, with  $H_{max} = 25.63m$  ( $H_{max}/H_s = 2.15$ ) and a crest height of  $\zeta_c = 18.5m$  ( $\zeta_c/H_{max} = 0.72$ ) represented an outstanding event and milestone for the ocean engineering community. The increasing number of such extreme wave observations brought this phenomenon into focus as occurrence, the formation process as well as the impact on offshore structures remain widely unknown. As a consequence, offshore structures have been equipped with wave sensors resulting in numerous freak wave observations all over the world (e.g. Wolfram et al. (2000); Mori et al. (2000); Guedes Soares et al. (2004a,b)). Real-world freak wave registrations and a general overview of freak wave research is found in Kharif et al. (2009).

The classification of when a wave is a freak wave is a delicate question and various definitions are proposed based on Rayleigh statistics. In particular, for the design

---

of offshore structures, the choice of the maximum wave height to be considered in the design process influences the efficiency and reliability significantly. In this context, the maximum wave height is defined as a multiple of the significant wave height. Based on Rayleigh statistics, the most probable maximum wave height in a 1000 waves registration is  $H_{max} = 1.86 \cdot H_s$  which is commonly used for the efficiency assessment of offshore structures in the design process. However, waves higher than  $H_{max} = 2 \cdot H_s$  occur with a probability of 28% and even wave heights higher than  $H_{max} = 2.3 \cdot H_s$  have still a probability of an 2.5% exceedance. Wolfram et al. (2000) analysed storm data recorded in the North Sea at North Alwyn from 1994 to 1998 and suggested that freak waves should be defined as  $H_{max}/H_s > 2.3$ . Faulkner (2000) reviewed design rules for ships and offshore structures exposed to harsh wave environment proposing a freak wave value of  $H_{max}/H_s > 2.4$  to be considered for survival design criteria. In terms of structure response, the NORSO standards developed by the Norwegian petroleum industry define the maximum wave height within a 100 year storm as  $H_{max} = 1.9 \cdot H_s$  at which an offshore structures has to withstand undamaged. In addition,  $H_{max} = 2.375 \cdot H_s$  shall be considered for the accidental limit state ( $10^{-4}$  annual exceedance probability) at which an offshore structure should not suffer complete loss of integrity.

### Formation Process of Freak Waves

The formation process of freak waves is still not completely solved due to the fact that only single point registrations of real-world freak waves are available impeding conclusions regarding the formation process around the measuring point. Different physical mechanisms have already been identified – wave-current interaction, superposition of (non-linear) component waves and/or modulation instability. The phenomenon of freak waves occurring due to wave-current interaction as well as superposition of component waves is well understood and explainable by linear theory (e.g. Trulsen and Dysthe (1997)). More complex mechanisms are based on non-linear dynamics which can be qualitatively modelled by the Non-Linear Schrödinger-type (NLS) equation under suitable assumptions. In this context, the discovery of the modulational instability of weakly non-linear deep water waves represents a substantial progress in terms of sudden freak wave genesis due to non-linear wave-wave interaction by coupling through the non-linear boundary condition (Benjamin and Feir, 1967). Even if the NLS equation is limited to weakly non-linear water waves and narrow-banded spectra it features many of the dynamics of freak wave formation due to the self-focussing phenomenon (Onorato et al., 2001a). Onorato et al. (2001b) have shown that the NLS equation is applicable to numerical investigations of the influence of the spectral bandwidth on the occurrence of freak waves in random sea states. It has theoretically been shown that freak waves ( $H_{max} > 2.2 \cdot H_s$ ) occur more often in sea states with narrow bandwidth and higher enhancement factors, respectively, which is related to the modulation instability. Consequently, the discovered Benjamin-Feir Index (BFI) has been rearranged for (random) wave spectra by relating the spectral bandwidth to the wave steepness (Janssen, 2003; Onorato et al., 2003). This influence of the

## *1. Introduction*

---

spectral bandwidth and wave steepness of wave spectra on freak wave occurrence has been verified by experiments (Onorato et al., 2005).

Based on these findings, numerous real-world freak wave registrations have been investigated in order to draw conclusions regarding the formation process. Kurkin and Pelinovsky (2004) estimated the BFI of the NYW. They stated that the abnormal wave is strongly non-linear and showed that seven waves are sufficient to manifest the modulation instability. Also Cherneva and Guedes-Soares (2008) investigated the non-linearity and non-stationarity of the NYW using higher-order time-frequency spectra. They also stated that the seven waves leading to the NYW observed by Kurkin and Pelinovsky (2004) are enough for the evolution of the freak wave due to the modulational instability. Based on the measured responses of the Draupner platform published by Karunakaran et al. (1997), Trulsen (2001) assumed that the NYW had occurred in a long crested sea state and simulated the spatial development of the NYW using a model for weakly non-linear spatial evolution of waves. The investigation showed that the real-world freak wave “did not occur suddenly and unexpectedly” as the NYW, he simulated, evolved from a large wave group 500m in front of the measuring point. Numerical investigations on four freak waves, recorded in the North Sea at the North Alwyn in 1997 (Wolfram et al., 2000) and carried out by Slunyaev et al. (2005), demonstrated that the lifetime of real-world freak waves “vary from several seconds up to 42s”, in which “the freak waves travel up to 325m”.

However, freak wave investigations in wave tanks are an inevitable element for a complete understanding of this phenomenon. Schmittner (2005) presented a procedure for the generation of tailored extreme waves as well as real-world registrations in seakeeping basins based on experimental optimization of the wave board motion. Based on this approach, Clauss and Klein (2011) reproduced the NYW in a seakeeping basin scaled according to the actual water depth at the Draupner platform and successively measured the spatial evolution of the extreme sea state along the tank. The investigations focussed on a possible temporal and spatial evolution of the NYW as well as on the underlying wave kinematics and dynamics. The analysis revealed that freak waves occur at three different positions in the seakeeping basin, emerging from a wave group which was propagating almost constantly along the wave tank. On the basis of this extensive measurements, Petrova et al. (2011) showed that the quasi-determinism theory (Boccotti, 2000) can be applied to the prediction of such steep wave events. Buchner et al. (2007) presented the evolution of an extreme wave at different positions in a wave tank, revealing that the extreme wave develops from a relatively normal wave to an extreme crest in less than half the wavelength.

Recently, exact solutions of the NLS equation, so-called breather solutions, have been rediscovered as prototypes for freak waves (Dysthe and Trulsen 1999; Osborne et al. 2000). These “Waves that appear from nowhere and disappear without a trace” (Akhmediev et al., 2009) feature many similarities to real-world freak

---

waves (Henderson et al., 1999). They serve as suitable analytic models simulating steep wave events (Dysthe and Trulsen, 1999) and are promising candidates for extreme wave modelling in wave tanks (Huijsmans et al., 2005; Andonowati et al., 2006). Chabchoub et al. (2011) showed that the breather solutions, namely the Akhmediev solution, lead to exaggerated amplitudes compared with the initial condition. Clauss et al. (2011) presented an experimental study on the evolution of the Kusnetzov-Ma breather solution. It has been demonstrated that the mechanism of modulation instability of the Kusnetzov-Ma breather leads to extraordinarily high waves in intermediate water depth – the formation of freak waves up to the maximum physically possible wave height has been observed. Chabchoub et al. (2012) investigated so-called higher-order breather solutions, presenting a successful generation of the Akhmediev-Peregrine breather in a small wave tank.

### Consequences for Offshore Structures

The consequences of freak wave impact on offshore structures may be disastrous. There are many reports from cruise vessels encountering freak waves, some escaped with no more than a fright whereas others suffered disastrous consequences (e.g. Schulz (2001); Bertotti and Cavalieri (2008); Lemire (2005)). Of special interest are the incidents of the cruise ships *Voyager* (February 2005) and *Louis Majesty* (March 2010) in the Mediterranean Sea. Both ships encountered steep wave events but not classical freak waves in terms of extraordinarily large wave height. These incidents are characterised by the encountering of a critical wave group in terms of structure response, i.e. the wave group builds up an unfavourable ship pitch response resulting in a phase-delayed encountering of the following steep wave crests at the bow of these ships. This shows that critical situations are not necessarily related to the highest waves.

The consequences of extreme sea states and freak waves for offshore structures are still under research. Ship losses such as the sinking of the single-hull tankers *Erika* (1999) and *Prestige* (2002) as well as that of the double-hull tanker *Ievoli Sun* (2000) confirm the need for systematic investigations. In contrast to cruise ships, where the impact of steep waves at the bow will cause (dangerous) local damage at the superstructure with potentially serious consequences, cargo vessels are more affected by wave-induced global loads which may cause structural failure.

Systematic experimental and numerical investigations have been performed in order to evaluate the impact of steep wave events on offshore structures. Gorf et al. (2000) showed that the wave steepness is an important parameter for local loads by analysing the bow damage of a floating production, storage and offloading vessel (FPSO). The influence of the bow geometry on the vertical wave bending moment has been investigated by Watanabe et al. (1989). Experiments with a container vessel showed that the vertical wave bending moment becomes strongly non-linear for large bow flares. The conclusion has been verified by Fonseca and Guedes Soares (2002) comparing numerical and experimental results of wave-induced ship motions and loads. They showed that large bow flares in combination with steep

waves significantly influence the global loads. As a result, the sagging loads are significantly higher than the hogging loads, which is associated with the “non-linear geometry” of the hull (Fonseca and Guedes Soares, 2002). These non-linear effects have been approved by Clauss et al. (2010a) for different ship types confirming the significant influence of block coefficient, bow flare and freeboard height on the vertical wave bending moment.

Comprehensive studies of the freak wave impact on offshore structures have been presented by Clauss et al. (2004, 2007), comparing numerical simulations and model test results, including the generation of deterministic wave sequences with embedded rogue waves as a critical prerequisite (Clauss, 2008). It has been shown that freak wave events are outstanding situations for any offshore structure to be investigated. The application of the breather solutions for the investigation of offshore structures exposed to extreme waves has been demonstrated by Clauss et al. (2012a).

## **Outline of the Thesis**

This thesis discusses the fundamental question of tailoring short-term critical wave sequences to be experienced by offshore structures for response-based design. The aim of this work is to establish new procedures for the identification and evaluation of critical wave scenarios. Therefore, two new concepts for tailoring critical wave sequences for response-based design are introduced.

The general overview of the water wave problem is given in Sec. 2. The focus lies on the standard model of ocean waves and its applicability to engineering problems (Sec. 2.3). In addition, the NLS equation and its analytical solutions are introduced in Sec. 2.4 as a basic principle for the subsequent experimental breather solution investigations.

The first concept, the application of analytical breather solutions of the NLS equation as innovative experimental design freak waves, is presented in Sec. 3. The breather solutions offer the fast generation of freak waves of certain frequency for subsequent model tests. The general applicability of breather solutions as well as the formation process is investigated in Sec. 3.2 and reviewed against the real-world NYW reproduction (Sec. 3.1). The characteristics of breather-type freak waves in terms of particle velocity and dynamic pressure are evaluated in Sec. 3.3 and compared to measurements in the NYW. Afterwards, the applicability of breather solutions for the generation of tailored irregular sea states with an embedded freak wave is shown in Sec. 3.4. Finally, the applicability for wave-structure investigations is evaluated in Sec. 5.1. Therefore, the impact of the breather-type freak waves on the vertical bending moment of a chemical tanker is analysed.

In Sec. 4.1, the basic principle of wave-structure interaction is introduced. Numerical procedures, namely the potential code WAMIT (Sec. 4.2) and the non-linear strip theory code from Instituto Superior Técnico (IST) of Technical University of Lisbon (Sec. 4.3), relevant for this thesis are briefly described. In addition,

---

the standard model of ocean waves adopted to the wave-structure interaction problem is introduced in Sec. 4.4. At the end, established design wave concepts are presented in Sec. 4.5.

Wave-structure interaction in terms of extreme response is addressed in Sec. 5. As aforementioned, the applicability of breather-type freak waves for wave-structure investigations is evaluated in Sec. 5.1. Afterwards, the second concept, a response-based identification tool, is introduced in Sec. 5.2 as a new design wave concept. This new tool tailors the response of an offshore structure straightforward to a specific extreme value revealing the underlying critical wave sequence. This method enables the tailored identification of wave sequence which causes the most critical response for specific offshore structures. The scope of application lies on an user-defined fully automated numerical identification of specific maximum system responses and its underlying critical wave sequences as well as experimental verification. Two typical design examples are applied for the verification of the general applicability. The first application (Sec. 5.2.1) addresses extreme ship response in terms of the maximum vertical wave bending moment of a chemical tanker. Objective is to identify wave sequences which lead to the maximum vertical wave bending moment in a certain design sea state. A multi-body offshore operation in terms of an offshore LNG - transfer system is investigated as a second application (Sec. 5.2.2). The objective is the identification of critical wave sequences which lead to failure of the transfer pipes or collision of the involved vessels. The optimization results are reviewed against classical design wave concepts and validated by model tests.

Finally, general conclusions are provided in Sec. 6.



## 2. Water Wave Problem

A precise knowledge of the genesis and evolution of waves as well as the associated kinematics and dynamics is indispensable for the design and evaluation of offshore structures. The physical mechanisms of sea waves are complex and based on stochastic excluding a simple solution. In the majority of cases the water wave problem is reduced to potential theory on a somehow simplified level. A historical overview of “The Origin of Water Wave Theory” can be found in Craik (2004).

This chapter presents a brief description of the water wave problem without attempting to be comprehensive – a holistic mathematical description can be found in classical text books, e.g. Newman (1977); Chakrabarti (1987); Mei (1983); Clauss et al. (1992). This chapter presents those solutions which are relevant for this thesis, namely the derivations of the Laplace equation as it is the most common theory for the engineering community. After a brief introduction of the boundary value problem of potential flow theory (Sec. 2.1), the utilized methods are presented in the order of complexity – from regular wave approaches via weakly non-linear description of wave propagation in the narrow-band approximation to fully non-linear simulations. It starts with Stokes wave theory (Sec. 2.2) as basis for the standard model of ocean waves (Sec. 2.3). The standard model of ocean waves offers a simple handling of the complex irregular sea. The frequency domain analysis serves as a fast and holistic approach for the evaluation of wave-induced loads and responses of offshore structures. Afterwards, particular attention is paid to the NLS equation in Sec. 2.4 facilitating the quantitative description of freak wave formation as well as the mathematical description of a class of freak waves occurring at sea – the so-called breather solutions. At the end of this chapter the fully non-linear numerical wave tank WAVETUB (Sec. 2.5) is introduced.

### 2.1. Potential Flow

Figure 2.1 presents the considered coordinate system showing the profile of the x-z plane. The y-axis (direction) is neglected in the following as this thesis concentrates on uni-directional wave systems. Neglecting the y-direction results in a significant mathematical simplification, but the general scheme of the derivation of the water wave solutions will rest unaffected. The point of origin is at the still water level, the positive z-axis faces upwards opposing the gravitational force. The positive x-axis points to the direction of wave propagation.

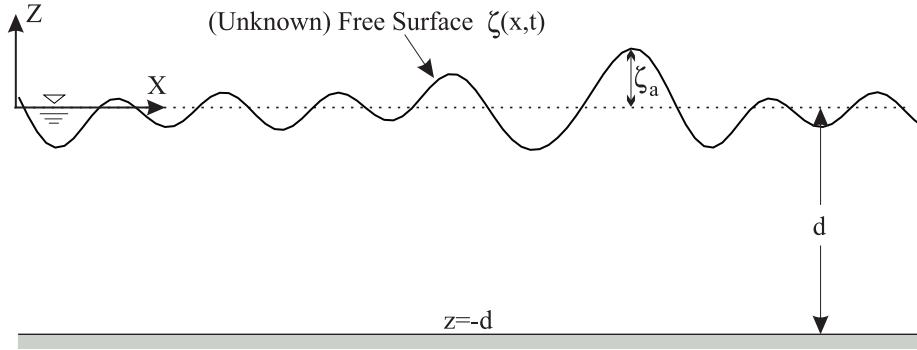


**Figure 2.1.:** Definition of the coordinate system showing the profile of the  $x$ - $z$  plane: The point of origin is at the still water level, the positive  $z$ -axis faces upwards opposing the gravitational force and the positive  $x$ -axis points to the direction of wave propagation assuming uni-directional waves.

Assuming that the Newtonian fluid is incompressible, inviscid and irrotational, the water wave problem can be mathematically described by the following (two-dimensional) governing equations:

$$\Delta\Phi = 0; \quad (2.1)$$

$$\frac{\partial\Phi}{\partial z} - \frac{\partial\Phi}{\partial x}\frac{\partial\zeta}{\partial x} - \frac{\partial\zeta}{\partial t} = 0 \quad \text{on } z = \zeta(x, t); \quad (2.2)$$

$$\rho g z + \frac{\rho}{2} \cdot \left[ \left( \frac{\partial\Phi}{\partial x} \right)^2 + \left( \frac{\partial\Phi}{\partial z} \right)^2 \right] + \rho \frac{\partial\Phi}{\partial t} = 0 \quad \text{on } z = \zeta(x, t); \quad (2.3)$$

$$\frac{\partial\Phi}{\partial z} = 0 \quad \text{on } z = -d. \quad (2.4)$$

The fluid domain is bounded by the bottom and the unknown free surface. The bottom of the fluid domain is considered to be level, rigid and impermeable (Eq. 2.4). The dynamic pressure at the free surface is defined to be constant equalling the atmospheric pressure (Eq. 2.3) and particles, which are elements of the resting free surface, must not leave the free surface of the waves (Eq. 2.2).

The solution of the boundary value problem is significantly complicated by non-linear terms in both surface boundary conditions and by the fact that these conditions have to be fulfilled at the unknown free surface  $z = \zeta(x, t)$  impeding an analytical solution for the exact boundary value problem. Therefore, approximate solutions are essential whereby different approaches lead to solutions with different scope of applications.

On the one hand, the solution can be approximated via numerical procedures up to fully non-linear simulations. Fully non-linear means that the numerical procedures solve the Laplace equation with non-linear boundary conditions at the free surface in spatial domain in combination with time-stepping schemes for wave evolution

in time domain. On the other hand, the problem can be reduced simplifying the Cauchy problem in combination with perturbation theory and Taylor series expansion to obtain analytical solutions to the problem. The solutions obtained differ due to the expansion order and perturbation parameters. Depending on the truncation order of the perturbation as well as on the utilized perturbation parameter  $\epsilon$ , different (common) wave theories are obtained:

- Stokes Wave Theory: the perturbation parameter is related to the wave steepness  $\zeta_a k$
- Non-Linear Schrödinger-type Equation: the perturbation parameter is related to the wave steepness  $\zeta_a k$  and bandwidth  $\Delta k$
- Shallow Water Wave Theory: the perturbation parameter is related to the relative water depth  $d/L$

## 2.2. Stokes Wave Theory

The genesis of the established wave theories is based on the comprehensive studies of Stokes (1849). Stokes wave theory approximates the Cauchy problem by applying the perturbation method and relating the perturbation parameter to wave steepness. The basic (first-order) solution of the Stokes expansion is the well-known linear wave theory, also known as Airy wave theory (Airy, 1845). Expansions of velocity potential and wave elevation are leading to higher-order solutions taking into account non-linearities such as the increase of the crest-trough asymmetry. The increase of the propagation speed due to wave steepness is only taken into account by Stokes Third-Order (e.g. Kinsman (1965)) or higher solutions. Skjelbreia and Hendrickson (1961) have solved the boundary value problem up to the 5. Order explicitly.

The most widely utilized wave theory is the linear one as it is a rather simple and fast method to calculate the wave field and its associated wave kinematics; thus, serves as an all-purpose tool for the engineering community. Additional simplifications are introduced for the determination of the linear solution affecting the (theoretical) area of validity of the theory. Figure 2.2 illustrates the regions of validity of various gravity water wave theories for regular waves with regard to the wave profile, giving a general outline about which theory can be used for different limiting parameters. The relative water depth is plotted on the abscissa and the relative wave height on the ordinate. Figure 2.2 shows that the linear wave theory is applicable to small amplitude waves, whereas for increasing wave heights (and hence increasing crest/trough asymmetries), the higher-order Stokes solutions apply.

However, Fig. 2.2 also shows that the linear theory can be applied to a large range of relative water depths. In addition, the linear theory provides appropriate results for wave steepness up to  $\zeta_a k < 0.05\pi$  (Hennig, 2005). The higher-order Stokes

## 2. Water Wave Problem

---

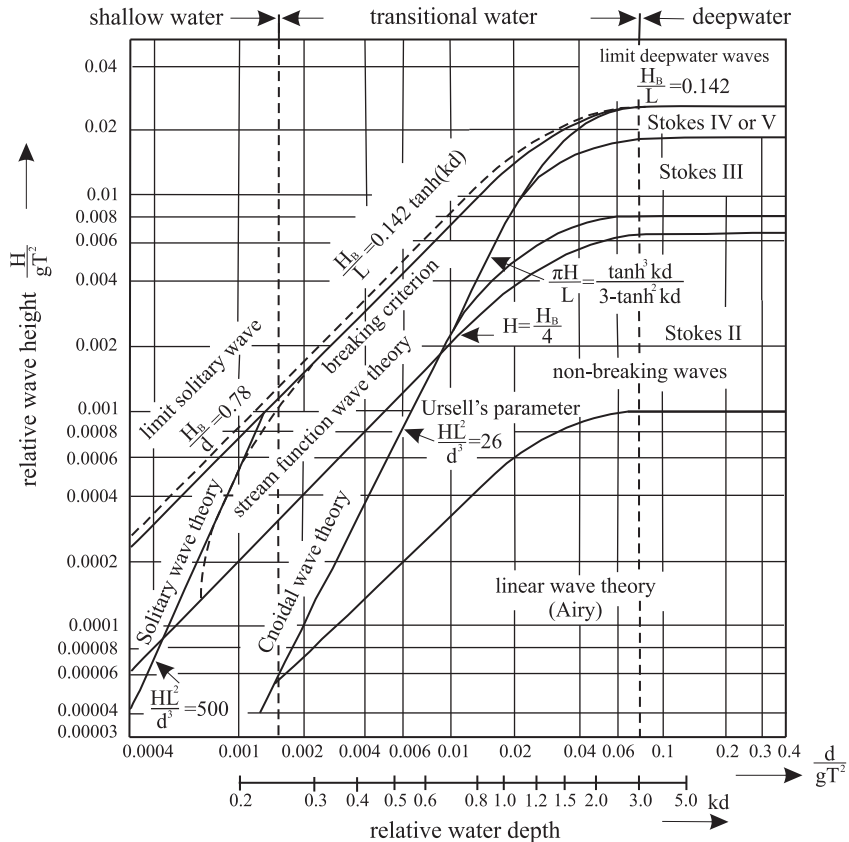


**Figure 2.2.:** Breaking wave height and regions of validity of various gravity water waves theories according to Clauss et al. (1992).

solutions are valid for relatively steep waves and are limited by the relative water depth and wave breaking limit, respectively (Hennig, 2005). The area of validity for deep or shallow water theory is defined by the Ursell parameter. Curves with constant Ursell numbers mark the boundary between different theories.

The Stokes wave theory as well as the other theories illustrated in Fig. 2.2 are appropriate for regular waves and the applicability is limited for natural seaways. For the description of natural seaways, a standard model of ocean waves is commonly used, which is introduced in the following section.

### 2.3. Standard Model of Ocean Waves

The natural seaway is complex, short crested and of stochastic nature resulting in varying wave heights, periods and directions. Hence, time series of real-world water waves are visually irregular and rarely feature regular wave behaviour. The desired sea state is regarded as superposition of independent harmonic “component” waves,

each having a particular direction, amplitude, frequency and phase based on linear theory

$$\zeta(x, y, t) = \sum_n \zeta_{an} \cos(k_n x \cos \theta_n + k_n y \sin \theta_n - \omega_n t + \phi_n), \quad (2.5)$$

with  $\zeta_{an}$ ,  $k_n$ ,  $\theta_n$ ,  $\omega_n$  and  $\phi_n$  as amplitude, directional wave number, direction, angular frequency and phase of the  $n^{th}$  component wave. Assuming long crested irregular sea states, simplifies Eq. 2.5 to

$$\zeta(x, t) = \sum_n \zeta_{an} \cos(k_n x - \omega_n t + \phi_n), \quad (2.6)$$

where the angular frequency and wave number are coupled via the dispersion relation

$$\omega_n = \sqrt{k_n g \tanh(k_n d)}. \quad (2.7)$$

The linear description of the natural seaway enables a simple handling of a complex process with widely acceptable results. Figure 2.3 shows the schematic representation of the standard model of ocean waves and its most relevant engineering applications – spectral analysis in terms of statistics (Sec. 2.3.1), wave generation (Sec. 2.3.2), analysis of wave-structure interaction (Sec. 4.4), stochastic frequency domain analysis (Sec. 4.4.1) as well as design wave concepts (Sec. 4.5).

- The spectral analysis of sea states enables a fast and simple evaluation as well as handling of complex sea states. The underlying wave kinematics can be determined fast and the surface elevation can be easily shifted in time and space (e.g. wave forecast, wave generation). In addition, the spectral parameters and wave statistics are easily determined via Fourier analysis. Empirical standard wave spectra for design purposes are also introduced and indispensable, based on energy density spectra measured in real-world natural seaways. Thus, this standard model is established in all relevant application areas – wave characteristics, wave statistics, wave generation and stochastic as well as deterministic wave-structure interaction.
- The spectral perspective of wave-structure interaction under the assumption of linear motion behaviour offers plenty of possibilities for evaluating offshore structures (Sec. 4.4): From direct calculation of the response in time domain for particular irregular sea states to short and long term statistic of the response (in terms of downtime or survivability of the offshore structure) as well as design wave concepts (Sec. 4.5)

“The analytical basis of spectral analysis of a discrete and finite record  $\zeta(t)$  is the Fourier transform” (Sobey, 1999), which can be efficiently calculated by means of the Fast Fourier transform (FFT) and inverse Fast Fourier transform (IFFT) respectively, as presented and implemented by Cooley and Tukey (1965).

## 2. Water Wave Problem

---

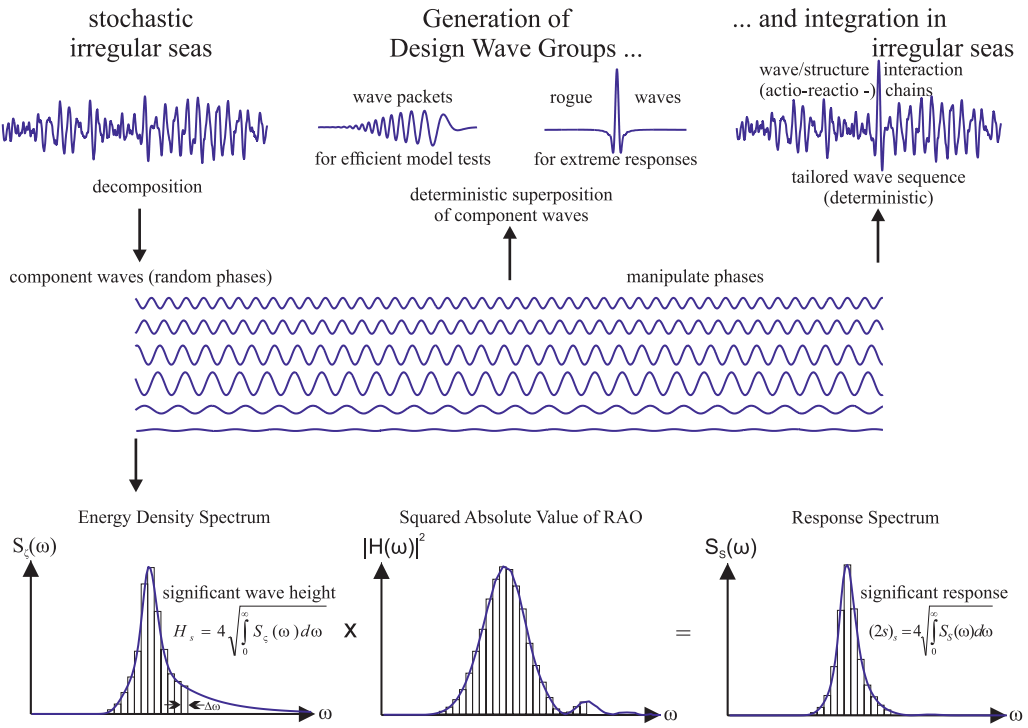


**Figure 2.3.:** Standard model of ocean waves – the irregular sea state is regarded as superposition of independent harmonic “component” waves, each having a particular direction, amplitude, frequency and phase based on linear theory.

### Spectra of Field Variables

The Fourier transform pair in combination with Parseval’s theorem provide the relation between the spectral description in frequency domain and the linear physics of surface gravity waves. Based on the spectral description of the natural seaway, the linear field variables can be determined accordingly. Table 2.1 presents the linear superposition solutions of the field variables and its Fourier transforms.  $\hat{F}(\omega)$  is the Hilbert transform of the surface elevation as the vertical velocity and the horizontal acceleration are depending on  $\sin(kx - \omega t)$ . The  $\omega^2$  multiplier for the Fourier transform of accelerations results in a  $\omega^4$  multiplier for the variance spectrum, which significantly overrate the contribution of the spectral tail and should be used with caution. The Fourier-type analysis is a very fast and efficient procedure for evaluating the kinematics under any irregular sea states. However, the linear approach tends to result in significantly higher values near the surface than observed in real sea states, in particular for high, steep waves. Using this procedure for the calculation of wave kinematics above the still water level (outside the mathematical scope) results in non-satisfying solutions up to “high frequency contamination” (Sobey, 1997). On this account, approximation methods are appropriate for improving the spectral approach on irregular sea states (e.g. Wheeler (1970); Chakrabarti (1971); Gudmestad (1986)).

$\Theta_n = k_n x - \omega_n t$	SUPERPOSITION	FOURIER TRANSFORM
$\zeta(x, t)$	$\sum_n \zeta_{an} \cos \Theta_n = \sum_n \zeta_n$	$F(\omega, x)$
$\hat{\zeta}(x, t)$	$\sum_n \zeta_{an} \sin \Theta_n = \sum_n \hat{\zeta}_n$	$\hat{F}(\omega, x)$
$u(x, z, t)$	$\sum_n \omega_n \frac{\cosh(k_n(z+d))}{\sinh(k_n d)} \zeta_n(x, t)$	$\omega \frac{\cosh(k_n(z+d))}{\sinh(k_n d)} F(\omega)$
$w(x, z, t)$	$\sum_n \omega_n \frac{\sinh(k_n(z+d))}{\sinh(k_n d)} \hat{\zeta}_n(x, t)$	$\omega_n \frac{\sinh(k_n(z+d))}{\sinh(k_n d)} \hat{F}(\omega)$
$\dot{u}(x, z, t)$	$\omega_n^2 \frac{\cosh(k_n(z+d))}{\sinh(k_n d)} \hat{\zeta}_n(x, t)$	$\omega_n^2 \frac{\cosh(k_n(z+d))}{\sinh(k_n d)} \hat{F}(\omega)$
$\dot{w}(x, z, t)$	$-\sum_n \omega_n^2 \frac{\sinh(k_n(z+d))}{\sinh(k_n d)} \zeta_n(x, t)$	$-\omega_n^2 \frac{\sinh(k_n(z+d))}{\sinh(k_n d)} F(\omega)$
$p_{dyn}(x, z, t)$	$\rho g \frac{\cosh(k_n(z+d))}{\cosh(k_n d)} \zeta_n(x, t)$	$\rho g \frac{\cosh(k_n(z+d))}{\cosh(k_n d)} F(\omega)$

**Table 2.1.:** Linear superposition method of field variables for natural seaways (Sobey, 1999).

### Spectral Parameters

The relation between the Fourier spectrum of a given wave registration and its wave energy can be deduced by Parseval's Theorem, resulting in

$$E(\omega_n) = S_\zeta(\omega_n) \Delta\omega = \frac{1}{2} \zeta_{an}^2. \quad (2.8)$$

Equation 2.8 corresponds to the total energy of a component wave (except  $\rho \cdot g$ ) which results in a direct proportionality between the area under the variance spectrum (also called energy density spectrum – see left bottom diagram in Fig. 2.3) of each component wave and the energy of the component wave per surface area. On the basis of the variance spectrum, the spectral parameters of the sea state can be determined describing its statistical characteristics. They are obtained by the spectral moments of the variance spectrum

$$m_j = \int_0^\infty \omega^j S_\zeta(\omega) d\omega. \quad (2.9)$$

The zeroth moment ( $j = 0$ ) represents the variance  $\sigma^2$  of the sea state which is equivalent to the total wave energy per surface area (normalized by  $\rho \cdot g$ ). For discrete registrations, the integrals become summations up to the Nyquist frequency

$$m_j = \sum_{n=0}^{N/2-1} \omega_n^j S_\zeta(\omega_n) \Delta\omega. \quad (2.10)$$

This can cause numerical inaccuracies for measured spectra as  $\omega^j E(\omega)$  reaches significant values for frequencies approaching  $\omega_{N/2}$ . “In practice, this is not a problem for the  $m_0$ ,  $m_1$  and  $m_2$  spectral moments which appear frequently in statistical theories” (Sobey, 1999), but for the  $m_4$  moment, the 4<sup>th</sup> power of  $\omega$  overrates the contribution of the spectral tail significantly. This can be avoided by smart truncation of the spectral tail but the result for  $m_4$  is very sensitive to this cutoff frequency.

## 2. Water Wave Problem

---

The spectral moments enable the determination of the following statistical properties

- Significant Wave Height

$$H_s = 4\sqrt{m_0} = 4\sigma \quad (2.11)$$

- Modal Period

$$T_1 = 2\pi \frac{m_0}{m_1} \quad (2.12)$$

- Zero-upcrossing Period

$$T_0 = 2\pi \sqrt{\frac{m_0}{m_2}} \quad (2.13)$$

- Peak Period

$$T_P = 2\pi \frac{\int_0^\infty S_\zeta^P(\omega) d\omega}{\int_0^\infty \omega S_\zeta^P(\omega) d\omega}. \quad (2.14)$$

- Spectral Width

$$\tilde{\epsilon} = \sqrt{1 - \frac{m_2^2}{m_0 m_4}} \quad [0 \leq \tilde{\epsilon} \leq 1] \quad (2.15)$$

$$\nu = \sqrt{\frac{m_0 m_2}{m_1^2} - 1} \quad (2.16)$$

Equations 2.15 (Cartwright and Longuet-Higgins, 1956) and 2.16 (Longuet-Higgins, 1975) present the most common formulas for spectral width. Equation 2.16 is introduced to avoid high frequency inaccuracies regarding the  $m_4$  moment for measured spectra. The spectral width  $\tilde{\epsilon}$  describes the distribution of the peak values of the sea state, e.g.  $\tilde{\epsilon} = 0$  results in the Rayleigh distribution and  $\tilde{\epsilon} = 1$  in the Gauß distribution. The number of peak values below the process average increases with expanding bandwidth  $\tilde{\epsilon}$ , i.e. the spectrum is distributed over a larger frequency band. For determining the peak period,  $P$  is usually set to be between 5 and 8 for common wave spectra ( $\omega_P < \omega_1 < \omega_0$ ) to weight the result strongly toward the visual peak of the spectrum (Sobey and Young, 1986; Mansard and Funke, 1988).

### 2.3.1. Statistical Analysis

As aforementioned, the natural seaway is of stochastic nature resulting in varying wave heights and periods. The assumed underlying Gaussian random wave model denotes that the superimposed harmonic wave components feature a Gaussian distributed irregular surface elevation with zero mean and standard deviation  $\sigma$ . Supposing that the seaway is a narrow banded random process (stationary and ergodic) and the waves are independent of each other, allows the application of

Rayleigh statistics which yields the probability of occurrence as well as exceedance of extreme values.

The Rayleigh distribution describes the probability density function of the wave heights,

$$\phi_R(H) = \frac{H}{4\sigma^2} e^{-\frac{H^2}{8\sigma^2}}. \quad (2.17)$$

Including Eq. 2.11 gives

$$\phi_R(H) = \frac{4H}{H_s^2} e^{-\frac{2H^2}{H_s^2}}. \quad (2.18)$$

The probability of the wave height being less than or equal to  $H_1$  (cumulative distribution function) is

$$\Phi_R(H_1) = \int_0^{H_1} \phi_R(H) dH = 1 - e^{-\frac{2H_1^2}{H_s^2}}. \quad (2.19)$$

The associated probability of exceedance  $P(H > H_1) = 1 - \Phi_R(H_1)$  for the highest wave in a registration of  $N$  waves yields

$$P(H \geq H_{max}) = e^{-\frac{2H_{max}^2}{H_s^2}} = \frac{1}{N}, \quad (2.20)$$

resulting in the well known relation

$$\frac{H_{max}}{H_s} = \sqrt{\frac{\ln N}{2}}. \quad (2.21)$$

As the cumulative distribution function for one selected wave height is  $\Phi_R(H_1)$ , we obtain  $\Phi_R^2(H_1)$  for the height of two succeeding (independent) waves, and  $\Phi_R^N(H_1)$  for  $N$  succeeding waves, i.e.

$$\Phi_{H_{max}}(H_1) = \Phi_R^N(H_1) = \left[ 1 - e^{-\frac{2H_1^2}{H_s^2}} \right]^N. \quad (2.22)$$

Differentiation of Eq. 2.22 with respect to the wave height leads to the probability density function (PDF) of the maximum wave height:

$$\phi_{H_{max}}(H) = \frac{\partial \Phi_{H_{max}}}{\partial H} = N \left[ 1 - e^{-\frac{2H^2}{H_s^2}} \right]^{N-1} \frac{4H}{H_s^2} e^{-\frac{2H^2}{H_s^2}}. \quad (2.23)$$

This PDF is plotted in Fig. 2.4 for different numbers of waves  $N = 1 \dots 10 \dots 10^3 \dots 10^5$  (continuous lines). In addition, the associated cumulative distribution of the maximum wave height  $\Phi_{H_{max}}$  is shown (Eq. 2.22; dashed lines). Note that for  $N = 1$  the PDF is reduced to the underlying Rayleigh distribution.

The PDF reveals the statistical character of the maximum wave height. As a result of these distributions it can be concluded, that in a 1000-waves registration a wave higher than  $H_{max}/H_s = 2$  occurs with a probability of 28% (see Fig. 2.4). Even a wave with  $H_{max}/H_s = 2.3$  has still a probability of an 2.5% exceedance.

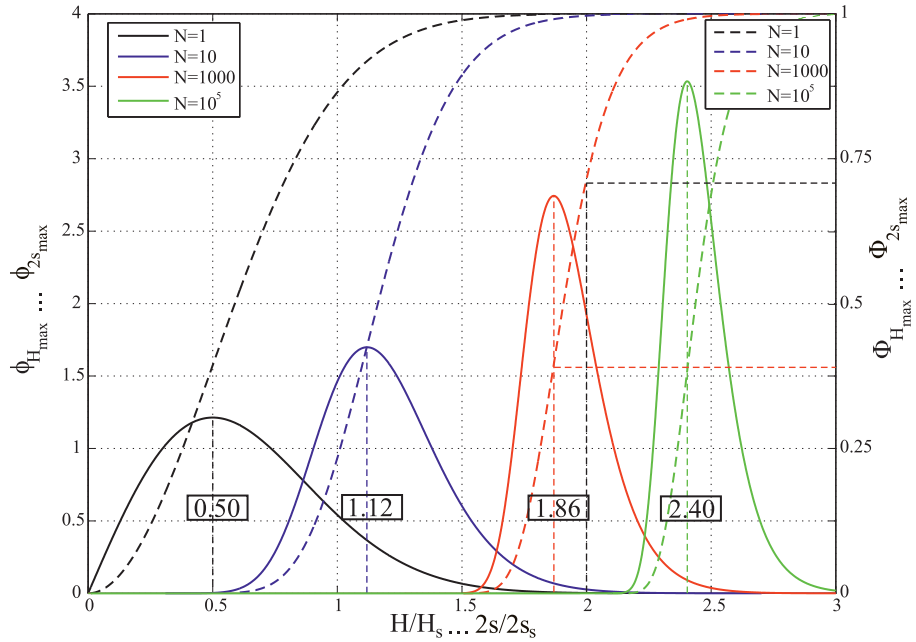


**Figure 2.4.:** Normalised probability density distribution of the maximum wave height  $\phi_{H_{max}}$  (maximum response  $\phi_{(2s)_{max}}$ ) as well as its cumulative probability distribution  $\Phi_{H_{max}}$  ( $\Phi_{(2s)_{max}}$ ).

### 2.3.2. Wave Generation

For the generation of irregular sea states and tailored wave sequences, the standard model of ocean waves is used. For this thesis only long crested waves have been generated enabling the application of the simplified Eq. 2.6 – each component wave is described by amplitude, frequency and phase.

Figure 2.3 displays the procedure used for wave generation. The component waves (centre) are used to create the desired wave sequence. For that matter, two fundamental principles can be utilized – random or manipulated phases – resulting in a set of different kind of deterministic wave sequences applied for model tests.

*Regular waves* are the basic application as only one component wave has to be utilized (amplitude and frequency exclusively, the phase is non-relevant). Regular waves are basically applied for determining hydrodynamic characteristics in terms of linear response behaviour. Assuming linear response behaviour, the response itself can be interpreted as superimposed linear components. Thus, the Response Amplitude Operator (RAO) of a system can be determined by a multitude of model tests with different wave frequencies.

*Stochastic irregular sea states* (Fig. 2.3 top left) represent the day-to-day business of test facilities. The harmonic components are determined from variance (standard) spectra and are combined with a random phase distribution. Stochastic irregular sea states allow the lifelike representation of the chaotic natural sea.

Objective is the evaluation of the system response in terms of short-term and long-term statistics. Typically, a set of sea states with different phase distributions is investigated to reduce statistical uncertainties.

*Transient wave packets* (Fig. 2.3 top centre) are synthesized wave groups with manipulated phases. The phases are manipulated in such way that all component waves are in-phase superimposed at a so-called concentration point resulting in a single high wave peak. This technique is based on the dispersion relation of water waves. The associated width of the amplitude spectrum can be adjusted to the relevant frequency range of the investigated offshore structure. Transient wave groups can be applied as design wave groups as well as very high “freak” waves (Clauss and Kühnlein, 1997), representing an efficient procedure for seakeeping tests. Compared to regular waves, transient wave groups with small steepness (Fig. 2.3 top centre left) offer the determination of the RAOs of a system by only one single test run, significantly reducing the cost-intensive tank time (Clauss and Kühnlein, 1995). Steep (breaking) wave packets (Fig. 2.3 top centre right) can be used for the evaluation of design wave loads on offshore structures.

*Tailored wave sequences* are complex structures of wave sequences. They comprise a multitude of different kind of wave sequences – from short critical wave groups obtained by previous numerical simulations via irregular sea states with embedded critical wave sequences (single high waves or dangerous steep wave groups) to exact reproductions of real-world registrations. A basic method of generating extreme waves within irregular sea states is illustrated in Fig. 2.3 top right. The very high “freak” wave obtained by the transient wave package technique is superimposed with an irregular sea state (with random phases). More complex and tailored sea states require more sophisticated reproduction procedures.

Basically, all presented methods (except regular waves) provide wave sequences for a specific location in the tank (so-called target location), which is usually not the position of the wave maker. Thus, wave trains which are not related to the position of the wave maker, have to be transformed upstream back to this position. The state of the art method is to transform the wave train by means of linear theory in frequency domain. The wave spectrum at the wave board will then be multiplied with the wave maker RAO and subsequently transformed back into time domain in order to determine the wave maker control signal. Typically, the wave maker RAO consists of two independent transfer functions – one represents the hydrodynamic relation between the wave board motion and the corresponding wave at the wave board (hydrodynamic RAO); the other represents the mechanical or hydraulic relation between the electrical control signal and corresponding wave board motion (electrical RAO). Both RAOs can be determined by experiments. The hydrodynamic RAO can also be modelled using an analytical function proposed by Biésel and Suquet (1951). Details regarding the water wave problem at the moving wave board can be found in Biésel and Suquet (1951); Svendsen (1985) and Schäffer (1996).

The generation of higher and steeper deterministic wave sequences, in particular the reproduction of real-world extreme wave events and critical sea states, require a more sophisticated approach. This is due to the fact that steep wave trains do not obey linear dispersion, i.e. the wave celerity is not only a function of frequency and water depth but also of wave height. Consequently, it is not possible to calculate the wave train linearly upstream back to the wave maker to determine the control signal of the wave board as the associated wave sequence will show substantial deviations at the target position due to non-linear propagation.

In the following, a brief description of two established experimental procedures is presented which have been applied in this thesis for tailoring extreme wave sequences in physical wave tanks.

### **Tailoring Extreme Wave Sequences**

In contrast to the standard procedure of generating irregular sea states, where the phase shift of the variance spectrum is supposed to be random, the phase spectrum of tailored wave sequences is an important deterministic quantity. The phase spectrum is responsible for all local wave characteristics at the target location. Consequently, the aim is to determine a control signal for the wave maker by manipulating amplitudes and phases which results in the desired wave sequence at target location. As aforementioned, this is a delicate problem as linear theory fails. As a consequence, experimental optimization schemes for the generation of tailored steep wave sequences have been developed which are briefly described below. The following two methods differ mainly regarding the grade of accuracy of the reproduction. The phase-amplitude iteration scheme (Chaplin, 1996; Schmittner et al., 2009; Schmittner and Hennig, 2012) offers a fast generation of tailored wave sequences with sufficient accuracy. The experimental optimization procedure (Schmittner, 2005) allows the exact reproduction of the wave sequence including several specific wave characteristics of the target wave at the expense of time as the procedure is time consuming.

#### **• Phase-Amplitude Iteration Procedure**

For the fast reproduction of critical wave sequences with sufficient accuracy, a phase-amplitude iteration procedure can be applied (Chaplin, 1996; Schmittner, 2005; Schmittner and Hennig, 2012). At first, the predefined wave sequence is transformed back from the target location to the position of the wave maker by means of linear wave theory. By multiplication with the electrical and hydrodynamic RAO in the frequency domain and subsequent IFFT, a first control signal is obtained. The wave sequence is then generated in a physical wave tank and recorded at the target position. Since non-linear effects like wave-wave interaction may occur during the experiment, the measured wave train differs from the target parameters. To improve the accuracy of the reproduced wave sequence at the target location, the control signal is

iteratively improved. The basic idea is to set up the rule of proportion between target and measured wave sequence in relation to target and utilized control signal. The ratio between the target and the measured wave sequence is determined in the frequency domain (amplitudes and phases separately) and multiplied with the used control signal to obtain the new (optimized) control signal. The procedure iteratively improves the control signal and reaches the optimum usually fast after 3 to 5 iteration steps. Afterwards no further improvement can be achieved. Strong non-linear wave-wave interactions such as modulation instability define the limitation of the procedure due to the fact that the rule of proportion provides only a simple linear relation between target and measured wave sequence. In addition, the procedure is limited to non-breaking short wave sequences. However, it has been shown that the procedure is capable of the fast generation of tailored wave sequences (Schmittner et al., 2009; Clauss et al., 2010b; Schmittner and Hennig, 2012; Clauss et al., 2013; Clauss and Klein, 2013).

### • Experimental Optimization Procedure

It has been generally observed that wave tank registrations at target location show substantial differences if a linearly utilized control signal is applied to the generation of tailored extreme wave sequences. Clauss (2001) showed that the main deviation is only localized within a small range proving that optimizing only a short segment of the control signal is adequate for tailoring extreme wave sequences. In other words, only the part of the control signal related to the wave environment close to the embedded target waves at the target location needs to be modified. Schmittner (2005) developed an experimental optimization procedure for the generation of tailored wave sequences with predefined characteristics taking this concept into account.

The fully automated optimization procedure is conducted in a physical wave tank taking all non-linear wave effects inherently into account. The procedure comprises the control and operation of the wave maker, measuring and analysing the wave sequence as well as modifying the control signal resulting in a self-validating process. The optimization process starts with the determination of the preliminary control signal. This signal is based upon the predefined wave sequence transformed linearly back to the position of the wave maker, neglecting wave-wave interaction and wave breaking. Thus, the first wave sequence will deviate from the target wave sequence. Objective of the optimization scheme is to improve the control signal with special emphasis on exact reproduction of the target wave in terms of wave height and period as well as vertical and horizontal asymmetry. As only a short temporally limited section of the control signal has to be modified, the discrete wavelet transform is applied (Gonzales Sanches et al., 1996) which enables local changes of the signal in time domain. The wavelet transformation converts the signal into several decomposition levels and each level comprises

a set of coefficients which describe the wave in specific time ranges. The Subplex optimization method (Rowan, 1990) is applied to adapt the control signal. The wavelet coefficients, which correspond to the wave environment close to the embedded target waves at the target location, are used as free variables to be modified by the Subplex optimization. The fully automated optimization scheme operates until convergence is achieved or the maximum number of iterations is reached.

Since the fully automated optimization process is time consuming, the optimization may be carried out in a small wave tank. Afterwards, the optimized control signal can be transferred to the seakeeping basin for investigations of wave-structure interaction. Sample applications of the experimental optimization procedure have been published by Clauss and Schmittner (2005); Schmittner (2005); Clauss et al. (2006) and Clauss and Klein (2009).

Both procedures are efficient in terms of generating tailored critical wave sequences, in particular, if the desired wave train is defined far away from the wave maker. In addition to this class of tailored wave sequences where the solution at the wave board is not known, a new class of tailored critical wave sequences, breather solutions of the NLS equation, has also been investigated for this thesis. The applied breather solutions provide the surface elevations at the wave maker (see Sec. 2.4 and 3.2) and the control signal is obtained immediately. Deviations between measured and target waves may occur and are related to the simplifications of the underlying wave theory.

## 2.4. Non-Linear Schrödinger-Type Equation

Weakly non-linear wave models have been introduced to take some important aspects of non-linearity into account. A substantial progress in the sense of the non-linear wave-wave interaction is the discovery of the modulational instability of weakly non-linear deep water waves, which has been independently discovered by Benjamin and Feir (1967) as well as Zakharov (1968). A historical review on this subject can be found in Zakharov and Ostrovsky (2009). It has been shown that weakly non-linear deep water wave trains are unstable to modulational perturbations due to migration of energy to adjacent side band frequencies. As a result, the self-focusing effect of the monochromatic wave causes a local exponential growth of the wave amplitude. The monochromatic wave train is unstable if the wave steepness  $k\zeta_a$  exceeds the perturbation wave frequency  $\delta$ ,  $0 < \delta \leq \sqrt{2}k\zeta_a$ . The instability condition, also known as BFI, has been rearranged by Janssen (2003) and Onorato et al. (2003) for (random) wave spectra by relating the spectral bandwidth with the wave steepness,

$$BFI = \frac{\sqrt{2}\epsilon}{\Delta\omega/\omega_c} \nu \sqrt{\frac{\beta}{\alpha}} = \frac{2\sqrt{2}\epsilon}{\Delta k/k_c} \sqrt{\frac{\beta}{\alpha}}. \quad (2.24)$$

The term  $\sqrt{\beta/\alpha}$ , introduced by Onorato et al. (2003), takes the influence of the water depth on the modulational instability into account.

Further investigations showed that the space and time evolution of weakly non-linear deep water waves obeys the NLS equations (Zakharov, 1968; Hasimoto and Ono, 1972). Yuen and Lake (1980) pointed out that all weakly non-linear methods lead to the same NLS equation by implementation of the same assumptions.

The NLS equation can be deduced from the potential equations. Assuming small amplitude waves and a narrow bandwidth spectrum, the boundary value problem is approximated by perturbation expansions. The perturbation parameters are the wave steepness  $\epsilon = k_c \zeta_a$  and the relative bandwidth  $\mu = \Delta k/k_c \ll 1$  (assuming  $\mu^2 \propto \epsilon$ ). In addition, the surface boundary conditions are simplified by introducing Taylor series expansions about still water level. Afterwards, the boundary value problem is separated into the different orders  $\mathcal{O}(\epsilon^{(n)})$  and each order is solved sequentially, starting from the lowest to the highest order. Truncation of the perturbation expansion at order  $\mathcal{O}(\epsilon^2)$  leads to the NLS equation (Serio et al., 2005),

$$\frac{\partial A}{\partial t} + \frac{1}{2} \frac{\omega_c}{k_c} \nu \frac{\partial A}{\partial x} + i \frac{1}{8} \frac{\omega_c}{k_c^2} \alpha \frac{\partial^2 A}{\partial x^2} + i \frac{1}{2} \omega_c k_c^2 \beta |A|^2 A = 0. \quad (2.25)$$

The second and third terms take the dispersive behaviour of the waves into account, whereas the last term is related to non-linear wave-wave interaction. The coefficients  $\alpha$  and  $\beta$  are depending on the carrier wave number  $k_c$ , the corresponding angular frequency  $\omega_c$  and the water depth  $d$  and read for arbitrary depth according to Serio et al. (2005) (the derivation of the coefficients can be found in Mei (1989))

$$\alpha = -\nu^2 + 2 + 8(k_c d)^2 \frac{\cosh(2k_c d)}{\sinh^2(2k_c d)}, \quad (2.26)$$

$$\beta = \frac{\cosh(4k_c d) + 8 - 2 \tanh^2(k_c d)}{8 \sinh^4(k_c d)} - \frac{(2 \cosh^2(k_c d) + 0.5\nu)^2}{\sinh^2(2k_c d) \left[ \frac{k_c d}{\tanh(k_c d)} - (\frac{\nu}{2})^2 \right]}. \quad (2.27)$$

The coefficient  $\nu$  represents the correction term for the group velocity in finite water depth,

$$\nu = 1 + 2 \frac{k_c d}{\sinh(2k_c d)}. \quad (2.28)$$

A remarkable feature of the coefficients  $\alpha$  and  $\beta$  is that their ratio  $\beta/\alpha$  converges to one as  $k_c d$  goes to infinity, decreases for decreasing water depth and becomes negative for  $k_c d < 1.36$ . The ratio  $k_c d = 1.36$  marks a physically important property – for  $k_c d > 1.36$  Eq. 2.25 has focusing properties, i.e. energy can be focused through modulational instability, which is impossible for  $k_c d < 1.36$ . Consequently, in water shallower than  $k_c d = 1.36$ , the modulation instability disappears. A detailed derivation of the NLS equation is presented in Annex B.

Equation 2.25 describes the evolution of wave groups in time of a space series. For wave tank applications, it is necessary to transform the leading order approximation (Eq. 2.25) to handle time series in space, as time series at specific locations in space are required and available, respectively, e.g. at the wave board as well as at every measuring point in the wave tank. The TNLS, where T stands for time, can be derived by an iterative procedure exchanging the derivatives in space with derivatives in time and vice versa (see e.g. Mei (1989)), resulting in

$$\frac{\partial A}{\partial x} + \frac{1}{C_g} \frac{\partial A}{\partial t} + i \left( \alpha' \frac{\partial^2 A}{\partial t^2} + \beta' |A|^2 A \right) = 0, \quad (2.29)$$

with

$$\alpha' = \frac{1}{8} \frac{\omega_c}{k_c^2} \frac{\alpha}{C_g^3}, \quad \beta' = \frac{1}{2} \omega_c k_c^2 \frac{\beta}{C_g}, \quad (2.30)$$

and with  $C_g$  as the group velocity. In the following, TNLS will be named NLS only for brevity reasons. The NLS can be solved exactly for initial conditions that decay sufficiently rapid by using the inverse scattering transform (Gardner et al., 1967). Otherwise, the wave propagation can be simulated by means of numerical procedures.

The simplest solution of the NLS is the plane wave solution. A small amplitude perturbation of this plane wave solution will lead to exponential growth of the amplitude during propagation which is specified as modulational instability. In addition, envelope soliton solutions as well as breather solutions have been identified as exact solutions of the NLS.

#### 2.4.1. Envelope Soliton Solution

Zakharov and Shabat (1971) solved the NLS exactly via inverse scattering transform predicting the existence of envelope solitons, which has been verified by experiments (Yuen and Lake, 1975). Envelope solitons constitute a stable wave group by balancing the wave dispersion and non-linearity of the system. Hence, the envelope propagates with permanent form as the “soliton is constituted by interacting coherent wave harmonics that prevents dispersion of the group” (Slunyaev et al., 2013). An interesting feature of envelope solitons is that the form will survive interactions with other solitons or wave packets. The envelope soliton solution of Eq. 2.29 describing the evolution of the envelope in space, of a time series, reads

$$A_S(x, t) = a_c \frac{e^{(-i\frac{1}{2}a_c^2\beta'x)}}{\cosh \left( a_c \sqrt{\frac{\beta'}{2\alpha'}} t \right)}, \quad (2.31)$$

where  $a_c$  is the soliton amplitude. Equation 2.31 is suitable for wave tank experiments as the wave can be defined at fixed locations (wave board, measuring point, etc.).

### 2.4.2. Breather Solutions

Breather solutions are characterized by slightly perturbed quasi-monochromatic waves in time or space. The perturbation of the breather envelope increases during evolution due to modulational instability resulting in large amplifications of the initial amplitude. In principle, each breather solution of the NLS can be built with arbitrary steepness, but it has to be considered that NLS theory does not predict the breaking or overturning of the waves. In nature, steepness hardly reaches values larger than 0.4 (Toffoli et al., 2010) because of wave breaking. Modulational instability theory described only the growth of a small amplitude perturbation of a plane wave solution; however, it has become common practice to discuss modulational instability also for large amplitude perturbations as the ocean waves are characterized by wave packets (Onorato et al., 2003; Onorato et al., 2005, 2006).

The following breather solutions are derived from the NLS equation (Eq. 2.29) and feature the following general form

$$A_B(x, t) = A_c(x)[G(x, t)e^{(i\phi(x))} - 1], \quad (2.32)$$

where  $G$ ,  $\phi$  are real functions to be determined and

$$A_c = a_c e^{(-i\beta' a_c^2 x)}. \quad (2.33)$$

A detailed discussion on the derivation of the three different solutions can be found in van Groesen et al. (2006) as well as in Karjanto and van Groesen (2007). At the end, the three known exact solutions of the NLS are obtained, namely the Kusnetzov-Ma breather, the Akhmediev breather and the Peregrine breather.

#### i) The Akhmediev Breather

The Akhmediev breather (Akhmediev et al., 1985; Akhmediev and Korneev, 1986; Akhmediev et al., 1987), also known as Soliton on Finite Background (SFB), describes the modulational instability process in space and is periodic in time. The breather shows an exponential behaviour in its non-linear regime resulting in large envelope waves due to modulational instability. For large negative and positive space variables, the solution corresponds to a perturbed Stokes wave. The corresponding analytical solution is

$$A_B(x, t) = A_c(x) \left( \frac{\tilde{v}^2 \cosh(\sigma x) - i\tilde{\sigma} \sinh(\sigma x)}{\cosh(\sigma x) - \sqrt{1 - \frac{1}{2}\tilde{v}^2} \cos(vt)} - 1 \right), \quad (2.34)$$

with  $\tilde{v} = v/a_c \sqrt{\alpha'/\beta'}$ ,  $\tilde{\sigma} = \tilde{v} \sqrt{2 + \tilde{v}^2}$  and  $\sigma = \beta' a_c^2 \tilde{\sigma}$  (Karjanto and van Groesen, 2007). Note that there exist several different ways of presenting the analytical expression of the solution (for details see Karjanto (2006)).

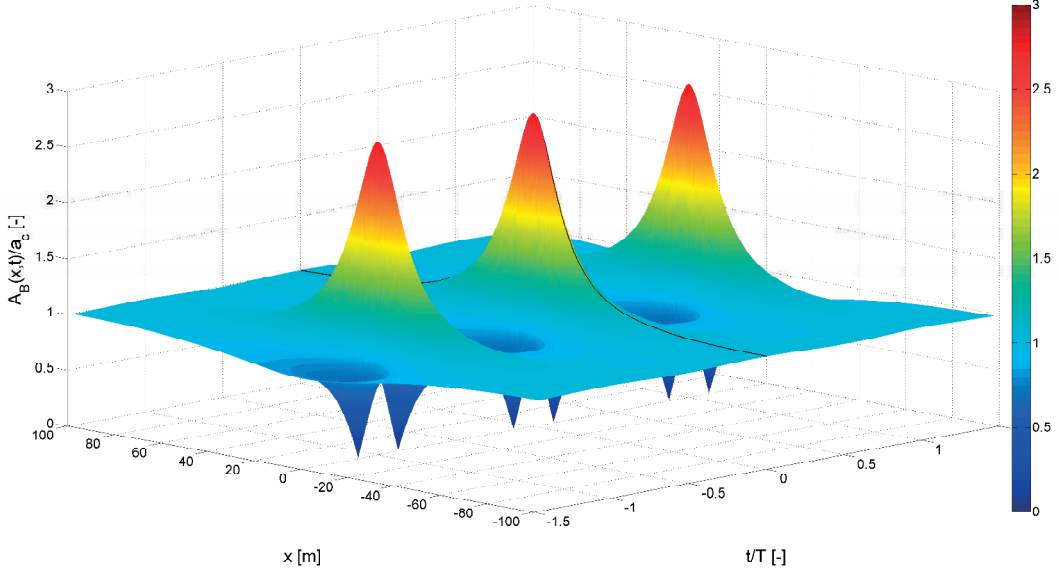


**Figure 2.5.:** Envelope of the Akhmediev breather in time and space. The amplitude amplification factor is defined as  $AAF = 2.8$  of the surrounding plane wave, resulting in a normalized modulation frequency of  $\tilde{v}^2 = 0.38$

Figure 2.5 presents the envelope solution of the Akhmediev breather in time and space. In order to determine the breather envelope, three parameters have to be predefined – the plane-wave amplitude  $a_c$ , the normalized modulation frequency  $\tilde{v}$  as well as the carrier frequency  $\omega_c$ . The periodicity in time of the solution is  $T = 2\pi/\nu$ . The maximum amplification of the breather – the ratio of maximum amplitude and the plane-wave amplitude – can be illustrated by the amplitude amplification factor (AAF), which depends only on the normalized modulation frequency  $\tilde{v}$ . The  $AAF(\tilde{v})$  reads

$$AAF(\tilde{v}) = 1 + \sqrt{4 - 2\tilde{v}^2}, \quad (2.35)$$

with  $0 < \tilde{v} < \sqrt{2}$  (Onorato et al., 2000; Karjanto, 2006). The AAF of the Akhmediev breather ranges between 1 and 3. For  $\tilde{v} > \sqrt{2}$ , the Akhmediev breather does not exist ( $AAF = 1 \rightarrow$  plane wave solution) and for  $\tilde{v} = 0$ , the Akhmediev breather turns into the Peregrine solution ( $AAF = 3$ ). For practical reasons, the AAF can be directly used as input parameter for wave tank experiments, as the AAF is exclusively related to the modulation frequency  $\nu$ . This denotes that the AAF, steepness  $\epsilon = a_c k_c$  and carrier frequency  $\omega_c$  define the breather characteristics by plain physical parameters.

### ii) Kusnetzov-Ma Breather

The Kusnetzov-Ma breather (Kuznetsov, 1977; Ma, 1979) is periodic in space and decreases exponentially in time. In contrast to the Akhmediev breather, where

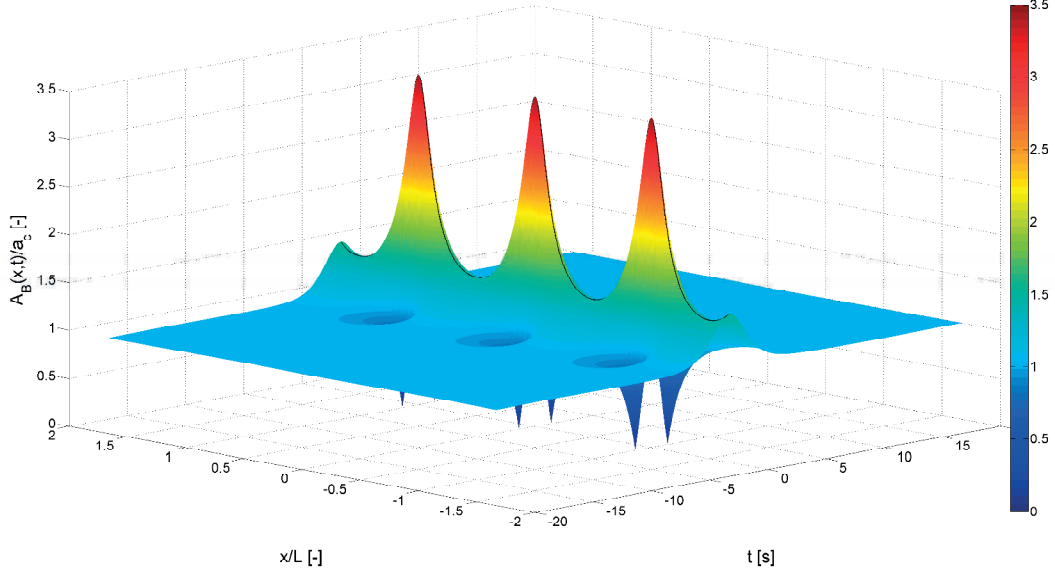


**Figure 2.6.:** Envelope of the Kusnetzov-Ma breather in time and space. The modulation length is  $L = 60$  m ( $x_t = 30$  m  $\rightarrow \eta = 0.1047$ ) and the amplitude amplification factor is  $AAF = 3.44$ .

the solution corresponds to a perturbed Stokes wave (plane wave plus a small perturbation) for the large positive or negative space limit, the modulation for the Kusnetzov-Ma breather is never small as the solution oscillates while propagating. Therefore, this solution does not correspond to the classical Benjamin-Feir instability. The corresponding analytical solution of the NLS is

$$A_B(x, t) = A_c(x) \left( \frac{-\sqrt{2}\tilde{\vartheta}^2 \cos(\eta x) + i\sqrt{2}\tilde{\eta} \sin(\eta x)}{\sqrt{2} \cos(\eta x) - \sqrt{2 + \tilde{\vartheta}^2} \cosh(\vartheta t)} - 1 \right), \quad (2.36)$$

with  $\tilde{\vartheta} = \vartheta/a_c \sqrt{\alpha'/\beta'}$ ,  $\tilde{\eta} = \tilde{\vartheta} \sqrt{2 + \tilde{\vartheta}^2}$  and  $\eta = \beta' a_c^2 \tilde{\eta}$  (Karjanto and van Groesen, 2007).

Figure 2.6 presents the envelope solution of the Kusnetzov-Ma breather in time and space. Again, three parameters have to be predefined in order to determine the breather envelope – the plane-wave amplitude  $a_c$ , the normalized modulation wave number  $\tilde{\eta}$  as well as the carrier frequency  $\omega_c$ . The periodicity in space is  $L = 2\pi/\eta$ . The  $AAF(\tilde{\vartheta})$  of this solution depends only on the normalized modulation wave number  $\tilde{\vartheta}$  (Karjanto, 2006),

$$AAF(\tilde{\vartheta}) = 1 + \sqrt{4 + 2\tilde{\vartheta}^2}, \quad (2.37)$$

with  $\tilde{\vartheta} \geq 0$ . For  $\tilde{\vartheta} = 0$ , the Kusnetzov-Ma breather transforms into the Peregrine solution ( $AAF = 3$ ) and for  $\tilde{\vartheta} \rightarrow \infty$ , the Kusnetzov-Ma solution results in the

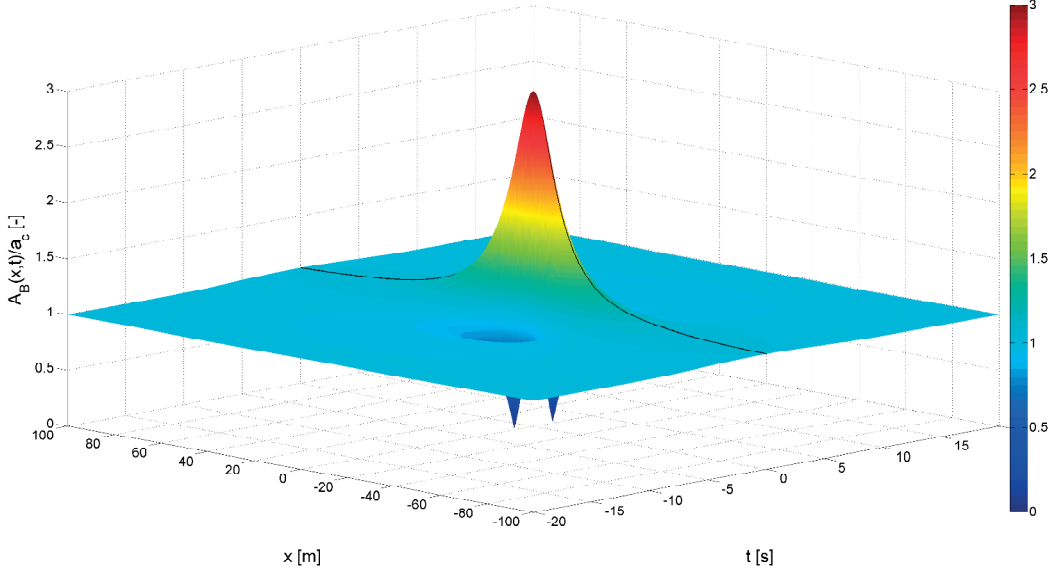


**Figure 2.7.:** Envelope of the Peregrine breather in time and space.

single soliton solution. By substituting  $v = i \cdot \vartheta$  into Eq. 2.36, the Kusnetzov-Ma breather turns into the Akhmediev solution. In contrast to the Akhmediev solution, where the AAF can be directly utilized for wave tank experiments, it is more convenient to apply the modulation length  $\eta$  of the Kusnetzov-Ma breather, by what the AAF is determined indirectly. Thus, the modulation length can be adjusted to the conditions of the wave tank. As a result, the three plain physical parameters essential for the determination of the Kusnetzov-Ma breather are the target location ( $x_t = \pi/\eta$ ), the steepness  $\epsilon = a_c k_c$  and the carrier frequency  $\omega_c$ .

### iii) Peregrine Breather

The Peregrine solution, also known as rational solution, has been originally derived by Peregrine (1983). The Peregrine breather represents the limiting case of the time-periodic Kusnetzov-Ma breather and the space-periodic Akhmediev breather. It has the peculiarity of being not periodic in time and in space: it is a wave that “appears from nowhere and disappears without trace” (Akhmediev et al., 2009) and has been considered as special prototype of freak wave (Shrira and Geogjaev, 2010). Its analytical form is (Karjanto and van Groesen, 2007)

$$A_B(x, t) = A_c(x) \left( \frac{4\alpha'(1 - i2\beta' a_c^2 x)}{\alpha' + \alpha'(2\beta' a_c^2 x)^2 + 2\beta' a_c^2 t^2} - 1 \right). \quad (2.38)$$

Figure 2.7 presents the envelope solution of the Peregrine breather in time and space. In contrast to the other two solutions, only the plane-wave amplitude  $a_c$  as

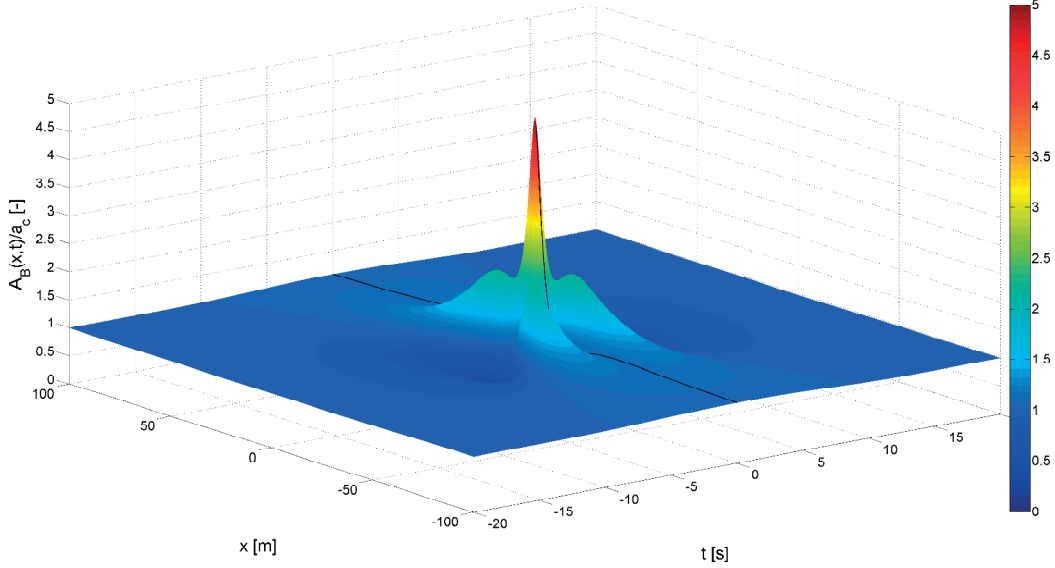


**Figure 2.8.:** Envelope of the higher-order Akhmediev-Peregrine breather in time and space.

well as the carrier frequency  $\omega_c$  (i.e. the initial steepness) have to be predefined to fully determine the Peregrine solution. The AAF is always equal to three and only the shape of the largest wave group changes depending on the initial steepness.

#### iv) Higher-order Akhmediev-Peregrine Breather

The Peregrine solution is the (simplest) “first-order” form of a hierarchy of rational solutions (Akhmediev et al., 2009). The basic structure of these rational solutions is

$$A_B(x, t) = A_c(x) \left[ \frac{G - iH}{D} - 1 \right], \quad (2.39)$$

which results for  $G = 4$ ,  $H = 8\tilde{\chi}$  and  $D = 1 + 4\tilde{\tau}^2 + 4\tilde{\chi}^2$  in the “first-order” Peregrine solution for  $\tilde{\chi} = a_c^2 \beta' x$  and  $\tilde{\tau} = \sqrt{\beta'/2\alpha'} a_c t$  (Akhmediev et al., 2009). In addition, there is also a lesser known higher-order solution available which has the same form of Eq. 2.39 with (Akhmediev et al., 2009)

$$G = (\tilde{\tau}^2 + \tilde{\chi}^2 + \frac{3}{4})(\tilde{\tau}^2 + 5\tilde{\chi}^2 + \frac{3}{4}) - \frac{3}{4}, \quad (2.40)$$

$$H = \tilde{\chi}(\tilde{\chi}^2 - 3\tilde{\tau}^2 + 2(\tilde{\tau}^2 + \tilde{\chi}^2)^2 - \frac{15}{8}), \quad (2.41)$$

and

$$D = \frac{1}{3}(\tilde{\tau}^2 + \tilde{\chi}^2)^3 + \frac{1}{4}(\tilde{\tau}^2 - 3\tilde{\chi}^2)^2 + \frac{3}{64}(12\tilde{\tau}^2 + 44\tilde{\chi}^2 + 1). \quad (2.42)$$

This higher-order solution is called Akhmediev-Peregrine breather (Chabchoub et al., 2012). Figure 2.8 presents the envelope solution of the Akhmediev-Peregrine breather in time and space. The AAF of the higher-order solution is also constant independently on the input but the maximum amplification is significantly increased to five times the background. Again, only the shape of the largest wave group changes depending on the initial steepness. For wave tank experiments, only the plane-wave amplitude  $a_c$  as well as the carrier frequency  $\omega_c$  (i.e. the initial steepness) have to be predefined to fully determine the Akhmediev-Peregrine breather solution.

## 2.5. WAVETUB

Several numerical methods have been developed for simulating freely propagating, non-linear water waves. Numerical methods denote discretization methods for the approximated solutions of the differential equations including the boundary conditions in space and time. Therefore, the numerical solution is usually related to a discretized finite spatial domain and provides results at discrete time steps. The methods to solve the free surface flow can be categorized by the discretization scheme used – fixed grid methods, grid-free methods or moving-grid methods (Scardovelli and Zaleski, 1999). Classical non-linear numerical wave tanks are in the majority of cases based on potential flow theory as its assumptions result in significant simplifications of the equations and computing time reduction with high accuracy at the same time. However, most of the codes are not able to handle wave breaking or similar effects. A review on non-linear free surface flow simulation techniques can be found in Westhuis (2001) as well as in the references therein. A more general overview of numerical methods to solve the class of problems in fluid dynamics can be found in Ferziger and Peric (2002).

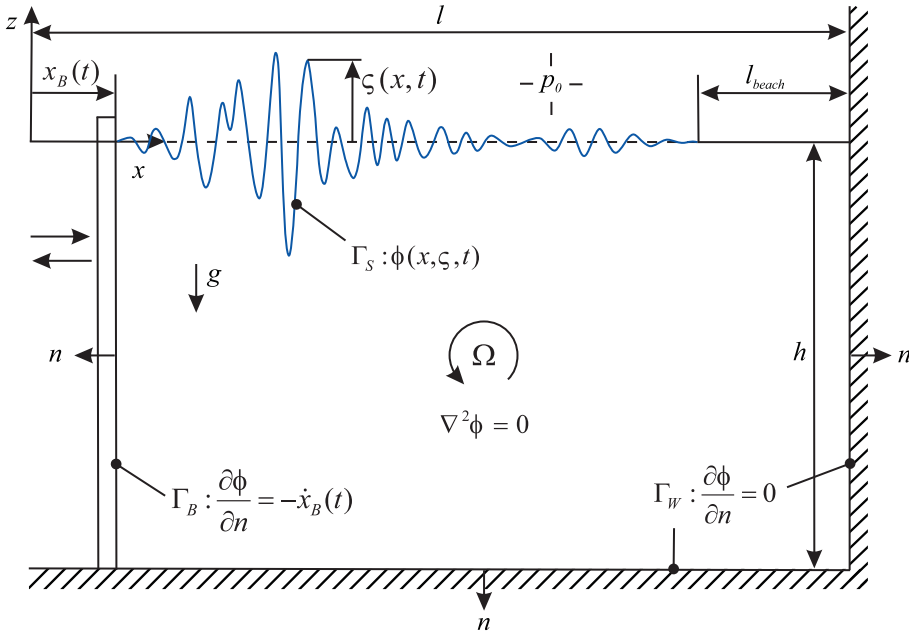
For this thesis, the well-established and validated fully non-linear wave tank WAVETUB (**WAVE** simulation tool developed at Technische Universität Berlin; Steinhagen (2001)) has been utilized for evaluation purposes of experimental results as well as thereby emerging questions related to the water wave problem. The following section briefly describes the basic principle of WAVETUB.

Figure 2.9 presents the mathematical model of the numerical wave tank developed by Steinhagen (2001). The two-dimensional, non-linear surface flow problem is solved with potential flow theory (cf. Sec. 2.1) in time domain which results in the following boundary value problem:

$$\Delta\Phi = 0 \quad \text{in } \Omega(t); \quad (2.43)$$

$$\Phi_x \zeta_x + \zeta_t - \Phi_z = 0 \quad \text{on } z = \zeta(x, t); \quad (2.44)$$

$$g\zeta + \frac{1}{2} \cdot (\Phi_x^2 + \Phi_z^2) + \Phi_t = 0 \quad \text{on } z = \zeta(x, t); \quad (2.45)$$



**Figure 2.9.:** Illustration of the mathematical model of WAVETUB (Steinhagen, 2001).

$$\Phi_z = 0 \quad \text{on } z = -d; \quad (2.46)$$

$$\Phi_x = 0 \quad \text{on } x = l; \quad (2.47)$$

$$\Phi_n + \dot{x}_B(t) = 0 \quad \text{on } x = x_B(t). \quad (2.48)$$

On top and bottom of the numerical wave tank, the already introduced (non-linear) boundary conditions are taken into account – kinematic, dynamic as well as bottom boundary conditions (cf. Eqs. (2.2 – 2.4)). In addition, two further boundaries are introduced to define the complete two-dimensional fluid domain  $\Omega$  – a wall on each side. The wall on the left side is defined to be movable to be able to generate waves within the numerical wave tank. Consequently as a boundary condition, the normal velocity of the fluid at the moving wall needs to equal the moving wall velocity,

$$\frac{\partial \Phi}{\partial n} = -\dot{x}_B(t), \quad (2.49)$$

whereby  $x_B(t)$  presents the wave board motion. The moving wall is implemented in such a way to simulate different types of wave makers – piston-type, flap-type and double flap-type wave boards. Hence, the wave board motion obtained in a physical wave tank can be directly used as input for the numerical calculations. On the right side, the wall is defined to be fixed and impermeable. To suppress wall reflections at long term simulations, a numerical beach is implemented at the end of the wave tank by adding artificial damping terms to the kinematic and dynamic free surface boundary condition.

## *2. Water Wave Problem*

---

For the calculation of the velocity potential in the entire fluid domain, the finite element method (FEM) is implemented, and at each time step, the potential for the current boundary conditions is calculated. On the basis of this solution, the velocities at the free surface are determined by second-order differences updating the potential, surface elevation as well as the position of the wave board. The classical fourth-order Runge-Kutta formula is used to develop the solution in time domain. At each time step a new boundary fitted mesh is created. The procedure is repeated until the desired time step is reached or the waves become unstable and break.

A detailed discussion on the theoretical background, on numerical verifications of spatial and temporal resolutions as well as on validation with experimental results can be found in Steinhagen (2001).

### 3. Extreme Waves

The following chapter focuses on the propagation, kinematics and dynamics of high steep waves exclusively. The formation process of steep wave groups and extraordinarily high waves in space and time is investigated at first:

- **New Year Wave** – this real-world freak wave is reproduced in the seakeeping basin and the spatial evolution has been measured at 520 positions.
- **Breather-Type Freak Waves** – the three known breather solutions of the NLS equation, i.e. Kusnetzov-Ma breather, Akhmediev breather and Peregrine breather, have been generated in the seakeeping basin for the first time. The spatial evolution of the Kusnetzov-Ma breather is measured at several positions and the measurements are compared with numerical results obtained with WAVETUB.

The objective of these investigations is to draw conclusions regarding the formation process of high, steep waves. On the one hand, a real-world freak wave is investigated, exploring the wave-wave interaction of a freak wave embedded in an irregular wave sequence (Sec. 3.1). On the other hand, breather-type freak waves are studied, investigating non-linear and dispersive waves in the narrow band approximation to validate the theoretical background as well as to evaluate their relevance for wave-structure investigations (Sec. 3.2).

Afterwards, the kinematics and dynamics of high, steep wave events are compared in Sec. 3.3. Namely, the NYW and a Peregrine breather with similar extreme wave characteristics are investigated. The dynamic pressure field as well as the particle velocities have been measured at different vertical positions up to the wave crest at the target position, i.e. at the position of maximum wave height and wave breaking, respectively.

The last part of this chapter (Sec. 3.4) presents the potential of breather solutions for the generation of tailored extreme wave sequences. It is shown that breather solutions can be used for the generation of irregular sea states with embedded freak waves. Moreover, the breather solution is tailored in such a way that the obtained freak wave embedded within the irregular sea state will finally be similar to the NYW.

### 3. Extreme Waves

---

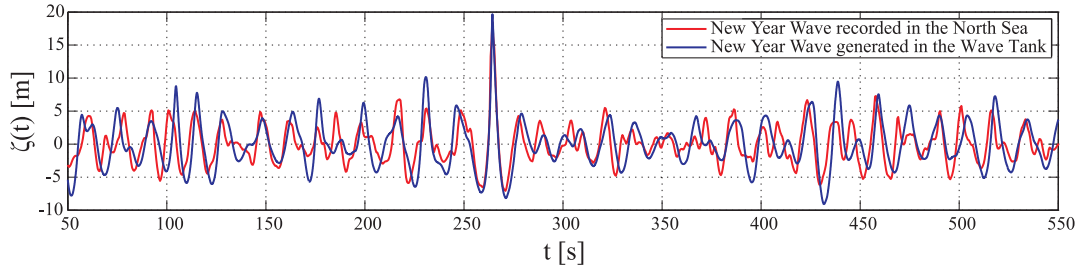


**Figure 3.1.:** Comparison of tailored model wave train measured in the seakeeping basin at target location ( $x_t = 3213m$  full scale) and the NYW sequence recorded at the Draupner platform (all data full scale; Clauss and Klein (2011)).

#### 3.1. New Year Wave

The scaled NYW has been reproduced in the seakeeping basin at Technische Universität Berlin (see Annex A for test facility details) at scale 1 : 70. For the reproduction of this real-world freak wave, the experimental optimization procedure is applied (see p. 21). Figure 3.1 presents a comparison between the real-world registration (red curve) and the reproduction in the seakeeping basin (blue curve) in full scale.

The surface elevation is successively measured along the basin, in a range from 2163m (full scale) ahead to 1470m behind the target position – altogether at 520 locations. The focus lies on the detailed description of a possible evolution of the NYW over a large area and time interval. Following results incorporate revised excerpts from the pre-release of Clauss and Klein (2011).

#### Experimental Setup

The experiments have been performed in the seakeeping basin at Technische Universität Berlin. The model scale is 1:70 depicting the exact representation of the actual water depth at the Draupner jacket platform. The towing carriage is equipped with thirteen surface piercing resistance-type wave gauges, installed at an interval of 0.2m. The seakeeping basin is subdivided into 20 measurement sections. To achieve a resolution of  $\Delta x = 0.1m$ , two measurements per section are carried out – at position  $x$  and  $x + \Delta x$ , respectively. The positioning of the probe array in the basin has been adjusted using a laser distance measuring device. The wave board serves as a reference point ( $x = 0m$ ) for the positioning of the array. Figure 3.2 schematically shows the experimental setup, with a side view of the setup (top) describing the order of measurements as well as a top view of the arrangement of the wave gauges installed on the towing carriage (bottom).

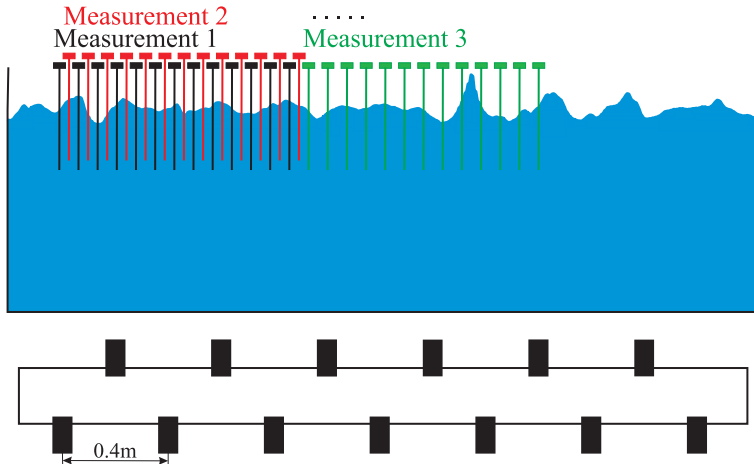


**Figure 3.2.:** Schematic sketch of the experimental setup (Clauss and Klein, 2011).

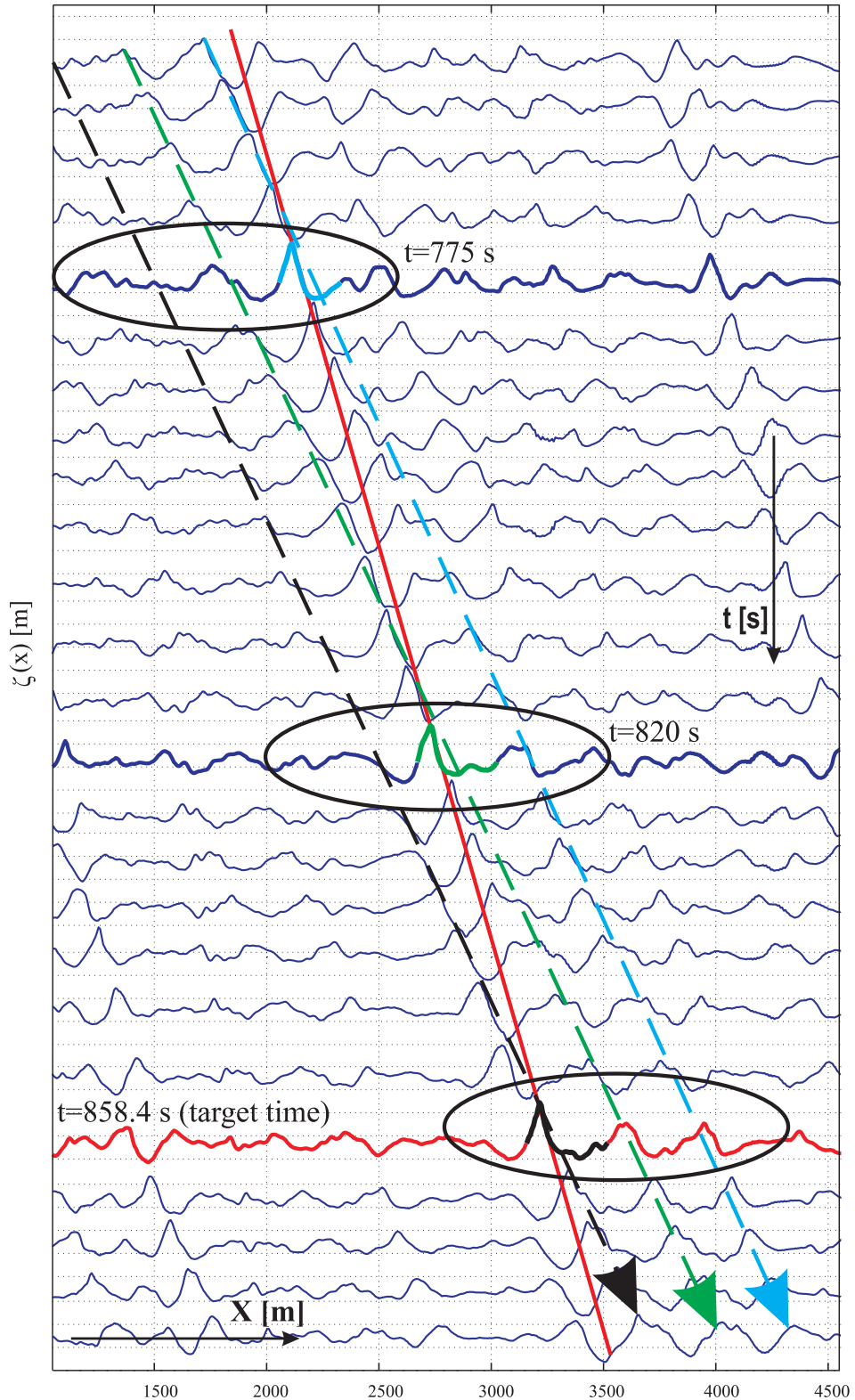
### Wave Propagation

Figure 3.3 presents the general overview of the experimental results in time and space. The horizontal axis indicates the spatial domain and the vertical axis the time domain. Each curve represents surface elevation snapshots for selected time steps – top to bottom from the beginning to the end of the evolution of the extreme wave sequence within the measuring range. The wave propagates from left to right.

The red curve in Fig. 3.3 shows the snapshot of the NYW at target time – the black highlighted segment marks the zero-downcrossing freak wave. Surprisingly, two further freak waves have been discovered during the analysis of the registrations indicated by the bold blue curves. The zero-downcrossing freak waves are additionally marked in light blue and green. The observed freak waves are developing from a wave group of three waves (black encircled in Fig. 3.3). The first conclusion is that a large wave group evolves along the seakeeping basin up to the target location to form the NYW. This is in accordance with the numerical results presented by Trulsen (2001) and Slunyaev et al. (2005).

Tracking the three individual waves of that wave group in space and time – the dashed straight lines in Fig. 3.3 – reveals that the waves propagate in parallel with nearly constant celerity (blue dashed line for the first, green dashed line for the second and black dashed line for the target wave). In addition, each wave grows up to the size of a freak wave and subsequently shrinking to a moderate wave height during propagation along the seakeeping basin.

Analysing the progress of the wave heights of the individual waves at each time step along the basin confirms that the three waves feature almost the same genesis, which is illustrated in the top diagram in Fig. 3.4. The wave height increases



**Figure 3.3.:** Spatial development of the NYW for selected time steps (full scale).

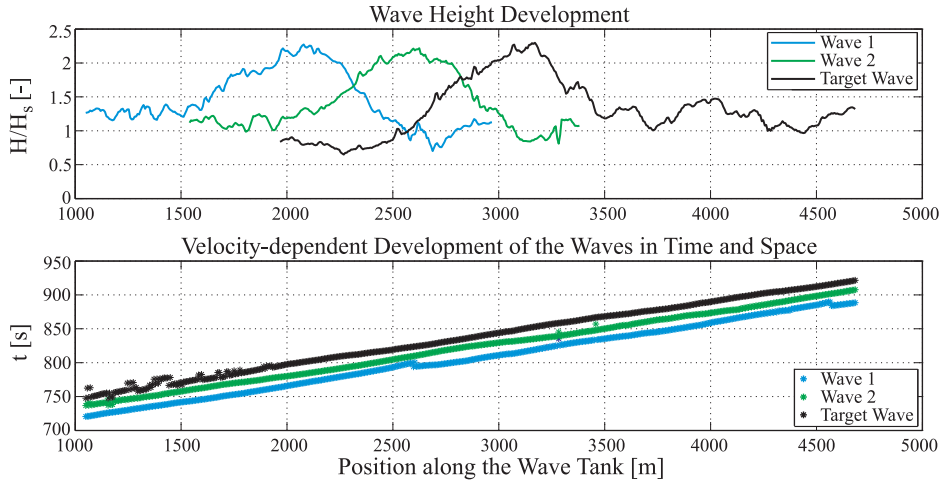


**Figure 3.4.:** Progress of the wave heights along the seakeeping basin and velocity-dependent development of the wave crests in time and space (Clauss and Klein, 2011).

continuously over a range of  $550m \sim 630m$ . In addition, the first two extreme waves ( $H/H_s > 2$ ) are propagating over a wide range ( $280m \sim 360m$ ) whereas the target wave ( $H/H_s > 2$ ) propagates the shortest distance. This is due to the fact that the NYW (in contrast to the first two freak waves) is breaking as a plunging breaker behind the target location.

The distance between the locations of the maximum wave height is almost constant ( $\approx 550m$ ), the first wave reaches its maximum height at  $2110m$ , the second at  $2624m$  and the target wave at  $3213m$ . A similar constant distance ( $\approx 500m$ ) between the locations of the maximum wave height is featured by two waves preceding the wave group, which are temporarily high waves on their own ( $H = 19.6m$  and  $23.1m$ ).

Following the dashed straight lines in Fig. 3.3 results in time and space coherence of the three wave crests along the basin. The lower diagram in Fig. 3.4 presents the corresponding velocity-dependent development of the wave crests in time and space. This diagram shows – similar to the dashed straight lines in Fig. 3.3 – that the wave crests propagate almost parallel and at constant speed when traveling through the seakeeping basin. Linear regression results in the following crest velocities:  $C_{crest_1} = 21.34m/s$ ,  $C_{crest_2} = 21.42m/s$  and  $C_{crest_{target}} = 21.31m/s$ .

The red straight line in Figure 3.3 illustrates the propagation of the highest wave elevation which is attributed to the three (subsequent) individual waves. Evaluating the propagation speed of the highest elevation results in  $C_{crest_{freak}} \approx 13m/s$ .

Summarizing the findings, it is revealed that the wave group features identical characteristics (see Tab. 3.1) and each wave emerges alternately to a freak wave. The first freak wave seems to accrue from energy contributions of the two waves

	wave 1	wave 2	target wave
$H_{max}$	26.82m	26.46m	27.41m
$H_{max}/H_s$	2.25	2.22	2.29
$\zeta_{c_{max}}$	17.28m	17.22m	18.15m
$\zeta_{c_{max}}/H_s$	1.45	1.44	1.52
$C_{crest}$	21.34m/s	21.42m/s	21.31m/s

**Table 3.1.:** Summary of the main characteristics of the three freak waves.

in front of the wave group. The following freak waves, again, develop from these energy contributions as well as due to the parallel propagation of the three individual waves within the wave group. Finally, the energy contributions focus to a plunging breaker at the target location.

### Energy Flux

This section looks at the energy flux in detail to prove the supposed freak wave mechanism mentioned before. At first, the group velocity is determined describing the energy propagation of the sea state. The upper three diagrams in Fig. 3.5 illustrate the procedure for three registrations exemplarily. The centroid  $c_{med}(t, x)$  (red dots in Fig. 3.5) of the mean energy distribution  $\bar{E}(t, x) \propto \zeta^2$ ,

$$c_{med}(t, x) = \frac{\sum_i \bar{E}(t_i, x) \cdot c_{med}(t_i, x)}{\sum_i \bar{E}(t_i, x)}, \quad (3.1)$$

with

$$\bar{E}(t_i, x) = \frac{1}{2} \rho g \zeta_i^2, \quad (3.2)$$

is determined by means of numerical integration ( $\bar{E}(t_i)$  energy and  $c_{med}(t_i)$  centroid of segment  $i$ ) for each registration along the basin. Subsequently, plotting all calculated centroids  $c_{med}(t, x)$  as a scatter plot (bottom diagram in Fig. 3.5) yields the space and time dependent progress of the centroid  $c_{med}(t, x)$  of the mean energy distribution  $\bar{E}(t, x)$ . Linear regression of the scatter plot results in the mean velocity of energy propagation  $C_{\bar{E}} = 11.73m/s$ .

Based on this result, the energy of the wave group is investigated in detail. Using the time-varying energy envelope concept (Stansberg, 1997) – the energy envelope  $E_H(t)$  of the wave group  $\zeta_{WG}$  can be described using the Hilbert transformation technique,

$$E_H(x, t) = \frac{1}{2} |\hat{\zeta}(x, t)|^2 = \frac{1}{2} [\zeta_{WG}^2(x, t) + \zeta_H^2(x, t)], \quad (3.3)$$

where  $\zeta_H$  is the real part of the Hilbert transformation of  $\zeta_{WG}$  and  $\hat{\zeta}(x, t)$  is the complex analytical signal of the real elevation  $\zeta_{WG}$ . Figure 3.6 illustrates the

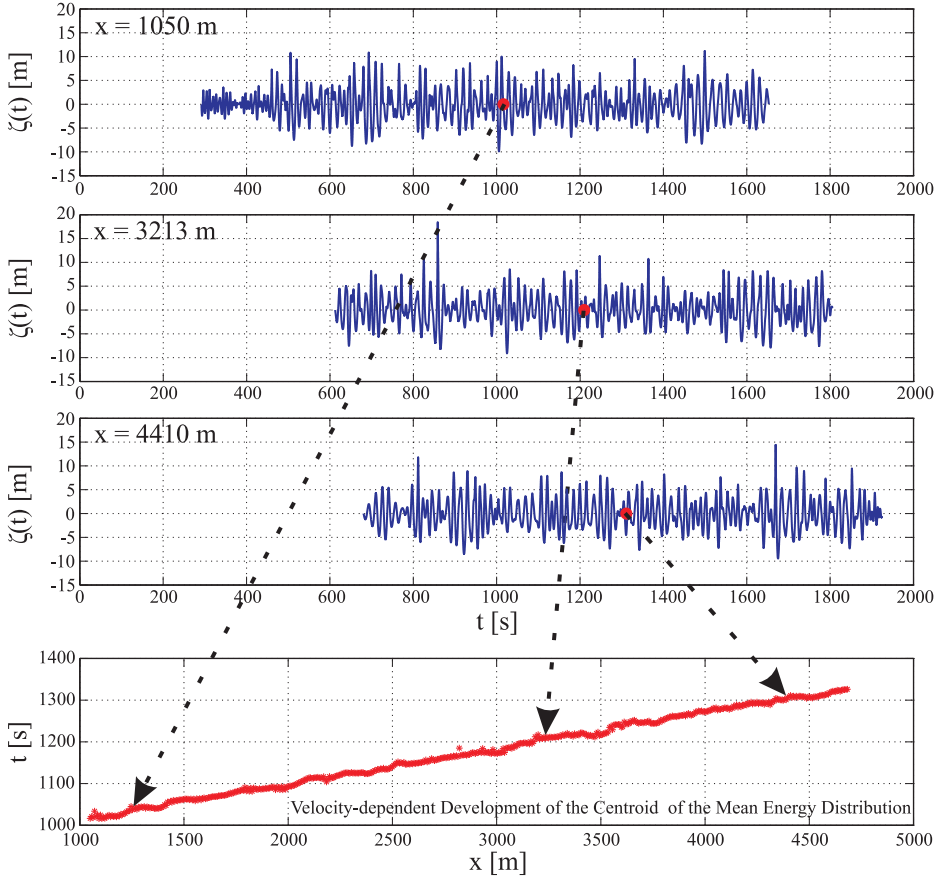


**Figure 3.5.:** Progress of the centroid of the mean energy distribution  $\bar{E}(t, x)$  for all registrations (Clauss and Klein, 2011).

energy envelopes at the three locations of freak wave occurrence. Similar to the mean velocity of energy propagation and the velocity of the highest elevation, the energy of the wave group propagates with  $C_{gr} \approx C_{crest}/2$ , i.e. with half of the celerity.

Finally, the supposed freak wave mechanism is verified – Fig. 3.6 shows that

- the energy of the (first) freak wave benefits from the two waves in front of the wave group,
- the following freak waves develop from these energy contributions due to the group velocity,
- the energy beneath the wave group focuses at the target location to the tailored NYW.

### 3. Extreme Waves

---

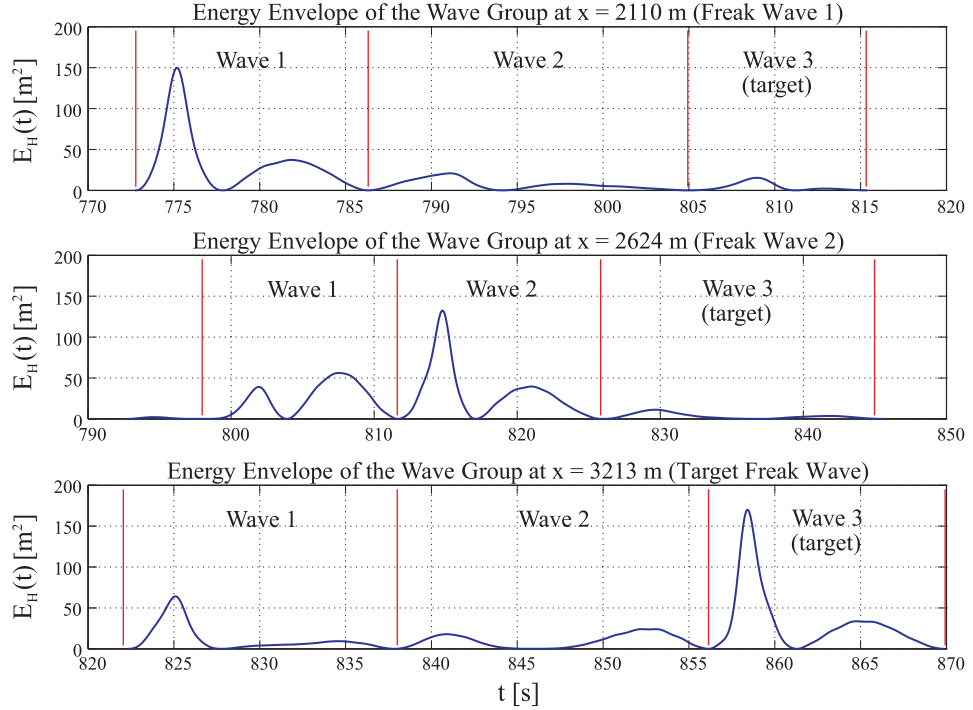


**Figure 3.6.:** Energy envelope of the wave group (time domain) at the locations of freak wave occurrence (Clauss and Klein, 2011).

## 3.2. Breather Solutions

The breather solutions are introduced as a new approach for the deterministic generation of freak wave events. This section presents systematic investigations of the evolution of the Kusnetzov-Ma breather solution exclusively. Figure 3.7 illustrates the theoretical Kusnetzov-Ma breather development based on Eq. 2.36 (cf. Fig. 2.6). The top diagram presents envelope (black curves) as well as associated surface elevation (blue curves) profiles of the Kusnetzov-Ma breather in time domain for different positions in space according to Fig. 2.6. The breather solution evolves from bottom to top (maximum amplification). Theoretically, as can be seen in Fig. 3.7, the perturbed wave sequence changes its shape due to modulational instability and results in an exaggerated high single wave at half of the modulation length ( $x/L = 0$  in Fig. 3.7), i.e. the wave sequence is unstable in terms of modulational instability. The dashed black curve in the top diagram of Fig. 3.7 indicates the course of the maximum breather amplitude in space and time. The associated Maximum Temporal Amplitude (MTA), which represents the maximum surface elevation of the propagating wave field in space over time, is shown in the bottom diagram. In this example, the maximum amplitude of the highest wave is  $AAF = 3.44$  higher than the surrounding carrier amplitude.

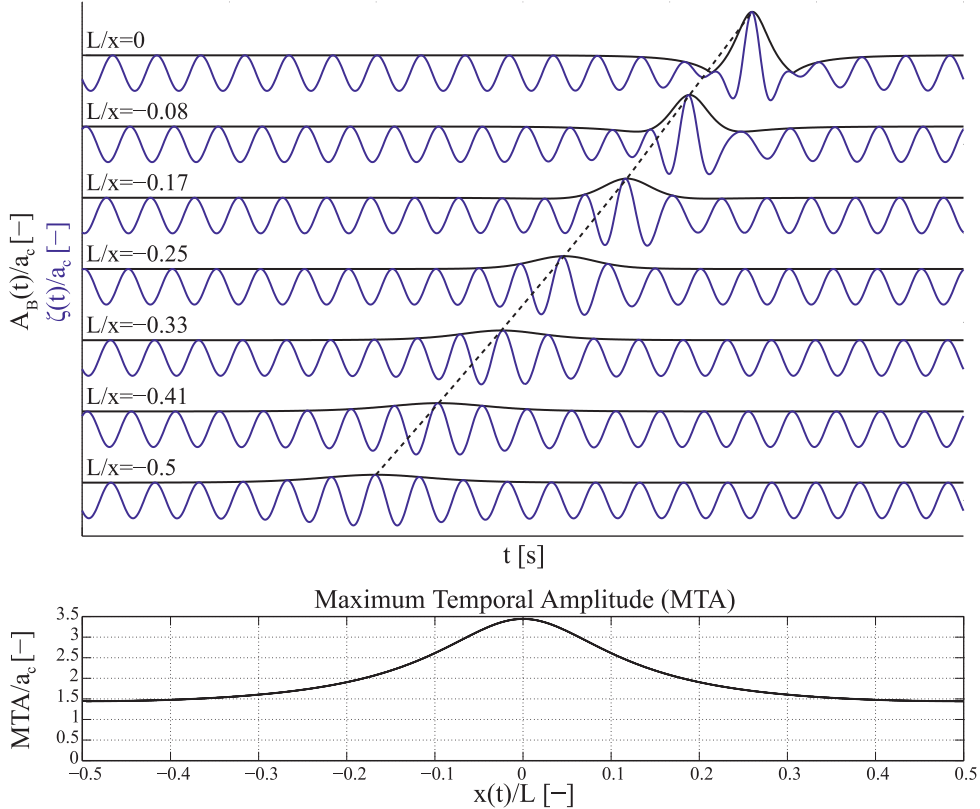


**Figure 3.7.:** Theoretical Kusnetzov-Ma breather development in time and space. The top diagram present envelope (black curves) as well as associated surface elevation (blue curves) profiles of the Kusnetzov-Ma breather in time domain for different positions in space. The breather evolves from bottom to top (maximum amplification). The dashed black curve indicates the course of the maximum breather amplitude in space and time resulting in the MTA. The bottom diagram presents the associated MTA in space.

The objective of the following study is to verify if the breather solutions are also unstable in terms of modulational instability in a physical wave tank, i.e. are the breather solutions applicable for the generation of extreme waves for test facilities. The focus lies on the deterministic generation of freak waves up to the maximum physically possible wave height. The second objective is to gain a deeper understanding on the formation process of freak waves in intermediate water depth such as at the location of the Draupner jacket platform, where the NYW occurred. Physics changes significantly for  $k_c d < 1.36$  whereby the waves become stable in terms of modulational instability (cf. Sec. 2.4). Hence, different carrier wave lengths and steepness are systematically investigated in the seakeeping basin to obtain conclusions regarding the influence of the water depth on the modulational instability. In addition, numerical simulations are conducted using WAVETUB. This allows a systematic adjustment of the wave tank geometry as the physical wave tank has limited scope regarding length and water depth. Following results incorporate revised excerpts from the pre-release of Clauss et al. (2011).

**Table 3.2.:** Overview of the investigated parameters of the Kusnetzov-Ma breather solution.

$T_c$ [s]	1.25	1.4	1.5
$k_c a_c$	0.1135/0.136/0.1475	0.1135/0.1475/0.17	0.1135/0.1475/0.17/0.1816
$d/L_c$	0.41	0.33	0.28
$k_c d$	2.58	2.05	1.79

### Experimental Setup

The experiments have been performed in the seakeeping basin at Technische Universität Berlin (see Annex A for details). The test setup consists of 10 surface piercing resistance-type wave probes installed in an interval of  $5m$  starting at  $15m$  and ending at  $60m$  in front of the wave maker. Table 3.2 presents the main parameters of the investigated waves. The first row shows the investigated carrier periods  $T_c$  and the second row the associated initial wave steepness  $k_c a_c$ . The wave steepness has been varied for each wave period to analyse its influence on the formation of the modulational instability. The carrier wave length  $L_c$  has been chosen in such a way that the ratio of water depth to carrier wave length fulfils the intermediate water depth condition ( $d/L_c < 0.5$ ; third row). The last row presents the product between carrier wave number and water depth describing the influence of the water depth on the modulational instability.

### Experimental Procedure

Equation 2.36 has been utilized for transferring the theoretical Kusnetzov-Ma breather solution with the smallest initial steepness for each carrier frequency into the seakeeping basin. Therefore, the surface elevation at the beginning of the modulation length (e.g.  $x/L = -0.5$  in Fig. 3.7) is used as initial condition at the wave board in order to determine the control signal. The subsequently investigated breathers with higher initial steepness are obtained by scaling the original wave sequence (with the smallest initial steepness). Consequently, the carrier amplitude as well as the amplitudes of the sidebands are increased equally; thus, not representing the exact Kusnetzov-Ma breather solution any more. This procedure is mainly applied due to the fact, that changing the initial steepness in Eq. 2.36 would result in significant differences regarding the AAF and the modulation length as the shape of the initial envelope at the wave board will change significantly. However, the objective of this study is to keep the shape of the breather at the wave board constant (except amplification) to ensure that the steepness is modified exclusively. This allows to associate the observed characteristics with the initial steepness.

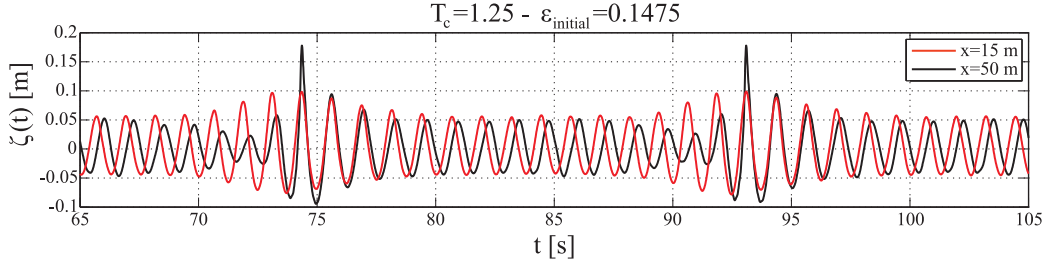


**Figure 3.8.:** Formation of the highest wave – comparison between time series measured at the beginning of the evolution (15m in front of the wave board) and the location of highest waves' occurrence (50m in front of the wave board) (Clauss et al., 2011). The time series measured at 15m is shifted in time domain for better comparability.

### Wave Propagation

Figure 3.8 presents the evolution of a Kusnetzov-Ma breather measured in the seakeeping basin comparing time series registered at the beginning of the measuring section (15m) and the location of occurrence of the highest waves (50m) for run  $T_c = 1.25s$  with  $\epsilon_{initial} = 0.1475$  (see also Fig. 3.10). Figure 3.8 proves that the Kusnetzov-Ma breather solution can be transferred into the seakeeping basin resulting also in an exaggerated high single wave due to modulational instability. The energy transfer of the surrounding waves to the freak wave can be basically observed in front of the freak wave.

Following, all Kusnetzov-Ma breathers presented in Tab. 3.2 are investigated in detail. For the evaluation of the breather propagation along the basin, the two main parameters – maximum wave height and maximum crest height – of each breather are investigated at each registration. The course of maximum wave height and maximum crest height represents the MTA of the breather indicating the existence of modulational instability. Increasing wave heights and, in particular, an increase in horizontal asymmetry illustrate the unstable behaviour of the wave sequence due to energy transfer between the carrier and the sideband frequencies, resulting in a single high wave within the wave train. Since the investigated wave trains comprise several breathers in a row, the mean value of both parameters has been evaluated at each registration.

Figure 3.9 presents the wave and crest height development along the basin for the investigated waves. The diagram is arranged as follows: the three carrier wave periods are illustrated separately, the top diagram of each block presents the maximum wave height and the bottom diagram the maximum crest height of the breathers. Each diagram compares the results for different initial steepnesses.

**Table 3.3.:** Properties of the measured breather-type freak waves.

Period $T_c$	Initial Steepness $k_c a_c$	Location	Horizontal Asymmetry $H_{crest}/H$	Max. Steepness $\pi \cdot H/L$
1.25 s	0.1475	50 m	0.64	0.438
1.4 s	0.17	45 m	0.6	0.37
1.5 s	0.1816	60 m	0.65	0.436

The following findings can be directly deduced from the diagrams:

- The shape of the breathers with the smallest initial steepness does not change significantly during the development along the measuring section.
- The breathers begin to show an unstable behaviour within the measuring section with increasing initial steepness.
- The highest initial steepness leads to maximum wave heights as well as maximum wave crest heights within the measuring section.
- The smaller the relative water depth  $k_c d$ , the higher the initial steepness to obtain the maximum wave and crest height within the measuring section.

Table 3.3 illustrates the properties of these highest waves. The modulational instability leads to high steep waves with a large horizontal asymmetry. The maximum steepness values show that the highest wave reaches almost the physically possible maximum wave steepness (wave breaking criterion:  $(\pi H/L)_{max} \approx 0.45 \tanh(kd)$ ) at the measuring point. This corresponds to observations during the experiments, where plunging breakers have been observed for the highest waves. Please note that the observed wave breaking locations are not exactly identical to the positions of the wave probes, particularly for run  $T_c = 1.4s$  with  $\epsilon_{initial} = 0.17$ , where the wave breaking was located at approximately 42m.

So far, the experiments show that modulational instability can be detected in limited water depth ( $k_c d > 1.36$ ). In addition, it has been observed that only higher initial steepness causes an unstable behaviour of the wave group within the measuring section. The instability condition of the Kusnetzov-Ma breather, which is exclusively affected by the water depth limit, is also fulfilled for the smaller initial steepness (cf. Tab. 3.2). The theoretical limiting case  $\tilde{\vartheta} \rightarrow \infty$ , resulting in the stable soliton solution, can be neglected and is excluded in this discussion. Hence, the smaller initial steepness breathers are to be unstable too (cf. Eq. 2.37). As a consequence, the distance the breathers (with the smaller initial steepness) have to pass before the perturbation grows is much longer than the measuring section. Thus, the main dimensions of the seakeeping basin in terms of measuring section as well as water depth limit the systematic investigations of the breather solutions

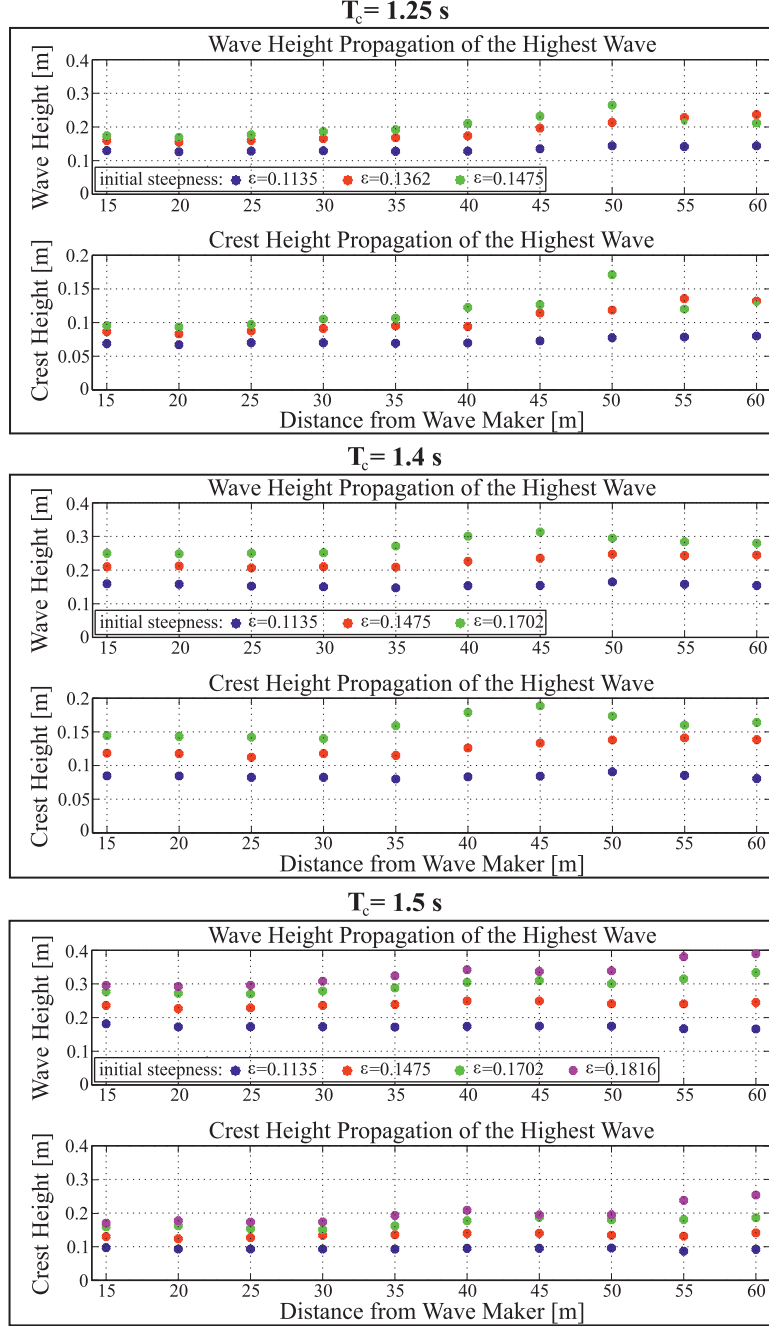


**Figure 3.9.:** Wave and crest height development of different Kusnetzov-Ma breathers along the seakeeping basin (Clauss et al., 2011). The three carrier wave periods are illustrated separately (black rectangle - top for  $T_c = 1.25\text{s}$ , centre for  $T_c = 1.4\text{s}$  and bottom for  $T_c = 1.5\text{s}$ ), the top diagram of each block presents the maximum wave height and the bottom diagram the maximum crest height of the envelope. Each diagram compares the result for different initial steepness.

with smaller initial steepness. These limitations are conquered by using the non-linear numerical wave tank WAVETUB in the following as its main dimensions can be easily adapted to meet particular issues.

## **WAVETUB**

The non-linear numerical wave tank WAVETUB (see Sec. 2.5) is utilized for systematic numerical investigations of the water depth influence on the modulational instability. WAVETUB is initially validated against experimental results to prove its general applicability. Afterwards, two fundamental questions have to be answered:

- What is the distance the breathers with the smallest initial steepness have to pass to reach the maximum wave height?
- What is the influence of the water depth on this distance?

Firstly, the propagation of the above presented breather solutions with the smallest initial steepness is simulated in order to determine the distance each breather has to pass to reach the maximum wave height. Secondly, the relative water depth  $k_c d$  is systematically varied to evaluate the influence of the water depth on this distance.

### Validation

For validation purposes, a worst case wave sequence regarding non-linear wave propagation is chosen. Run  $T_c = 1.25s$  is preset with  $\epsilon = 0.1475$  due to the high initial steepness and the registered freak waves at  $x = 50m$ . Figure 3.10 compares experimental results (black dashed curves) against numerical calculations (red curves) at different positions up to the location where wave breaking occurs. The overall agreement is good, only the maximum wave heights at the bottom diagram ( $x = 50m$ ) differ slightly due to the fact that WAVETUB does not take wave breaking into account. The results obtained with WAVETUB have been shifted in time domain with a constant  $\Delta t = +0.2s$  due to an identified delay between the experimental results and the numerical calculations. The delay arises from a phase delay caused by a low-pass filter inserted between the control unit and the wave maker. However, it is clearly identifiable that WAVETUB reproduces the formation process of non-linear waves accurately.

### Numerical Results for the Smallest Initial Steepness

For the simulation of the breather solutions with the smallest initial steepness, the numerical wave tank geometry is elongated in such a way that the highest wave height of the propagating breather is detected before the first wave of the breather reaches the numerical beach. Figure 3.11 presents the results of the numerical simulations. The three different carrier wave periods are illustrated separately – top for  $T_c = 1.25s$ , centre for  $T_c = 1.4s$  and bottom for  $T_c = 1.5s$ .

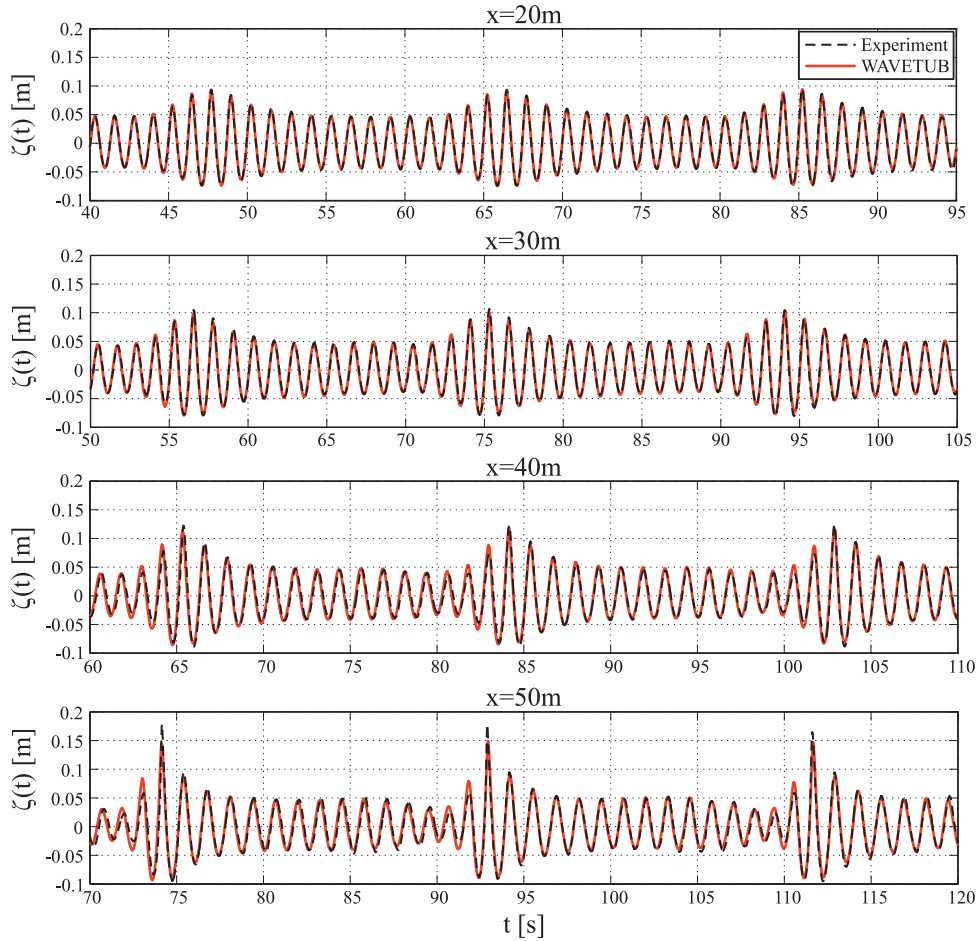


**Figure 3.10.:** WAVETUB vs. Experiment: Comparison between experimental results and numerical calculations at different positions in the basin up to the location where the wave breaks ( $x = 50m$ ) for  $T_c = 1.25s$  and  $\epsilon_{initial} = 0.1475$  (cf. Tab. 3.3).

The top diagram in each block presents the surface elevation at  $x = 60m$  and the bottom diagram the surface elevation at the location of the maximum wave height occurrence. The calculated surface elevations at  $x = 60m$  are additionally compared to the experimental results to evaluate the quality of the numerical calculations. The numerical simulations prove that the breathers with the smallest initial steepness are also unstable. However, it is also obvious that the three breathers need a comparatively large distance to reach the maximum amplification. Thereby, the results indicate a dependency between the relative water depth and the maximum amplification distance – the smaller the relative water depth  $k_c d$ , the longer the maximum amplification distance. The experimental results support this finding: for the longer carrier wave lengths the initial steepness needed to be further increased in order to obtain the maximum amplification within the measuring section (cf. Fig. 3.9).

### 3. Extreme Waves

---

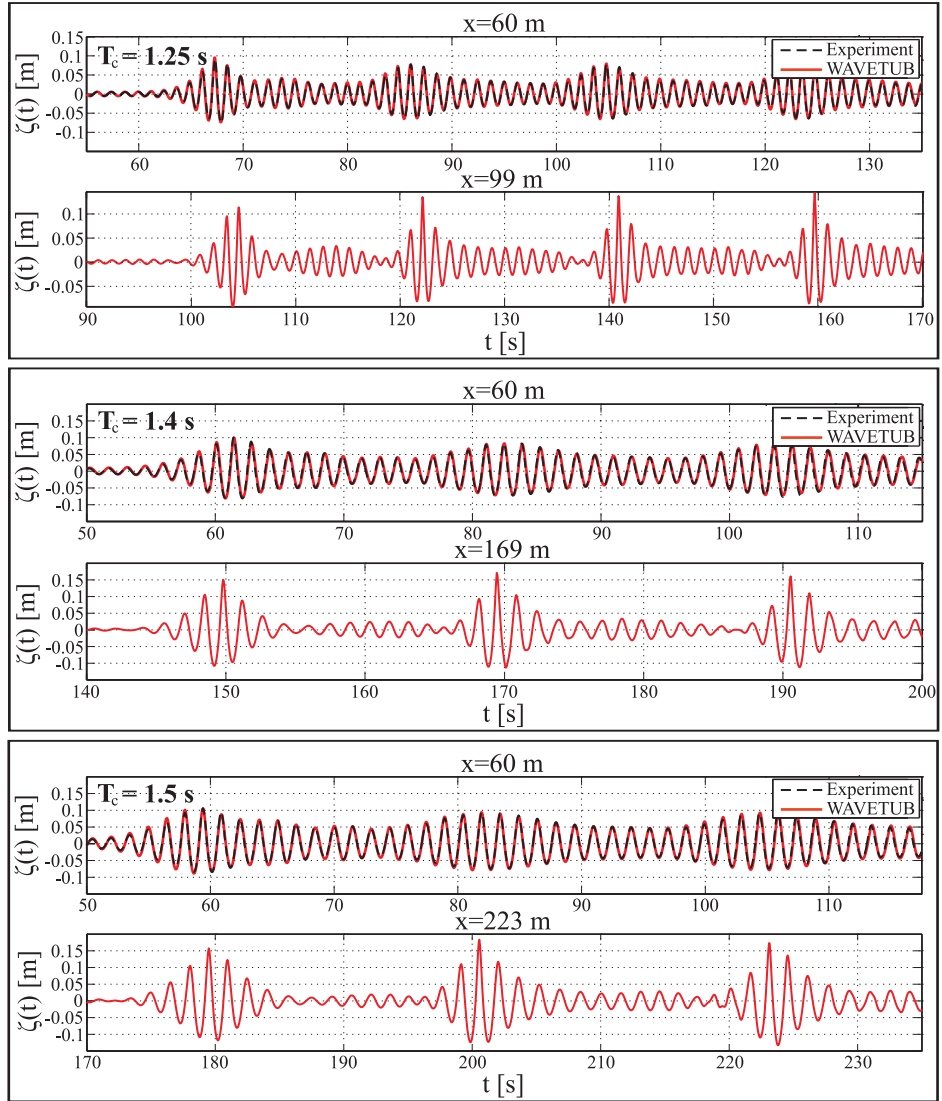


**Figure 3.11.:** WAVETUB results for the three carrier frequencies with the smallest initial steepness  $\epsilon = 0.1135$  (cf. Tab. 3.3).

#### Variation of Water Depth

Next, WAVETUB is used for a systematic variation of the water depth to verify the dependency between the relative water depth and the maximum amplification distance. Therefore, numerical calculations are performed in different water depths for a given Kusnetzov-Ma breather. The above investigated breather solution with the carrier frequency  $T_c = 1.4\text{s}$  and the smallest initial steepness ( $\epsilon = 0.1135$ ) is chosen. The numerical wave board motion for the different water depths has been adjusted using the Bi  sel function (Bi  sel and Suquet, 1951), to ensure that the wave sequences at the wave board are identical for the different water depths.

Figure 3.12 presents surface elevation snapshots at the time of occurrence of the first maximum wave height for the investigated water depths – the water depth increases from top to bottom. The initial and the termination ramp of the wave sequence are excluded in the evaluations, i.e. the three breathers inside the wave sequence are considered. For the determination of the location of the maximum wave height occurrence, the maximum temporary crest amplitude has been tracked during the spatial development along the numerical wave tank up to the position where the wave crest reaches its maximum and breaks. In this context, it should be noted again that the wave breaking phenomenon cannot be simulated using WAVETUB and that the simulation of the steepest waves prior to the breaking point is delicate – a smoothing function for the FEM grid is implemented to avoid a program termination due to wave breaking which influences the wave profile and propagation after the wave breaking event. However, the quantitative detection of the location of the maximum wave height is unaffected.

Figure 3.12 clearly demonstrates that the distance the envelope has to pass before reaching its maximum wave height is strongly depending on the water depth. In intermediate water depth ( $d \leq 1.5m$ ) the distance increases significantly with decreasing water depth and approaches infinity probably at  $k_c d < 1.36$  where the waves become stable as the non-linear term in the NLS equation changes its sign.

Finally, the following results are discovered:

- The mechanism of modulational instability leads to extraordinarily high waves in intermediate water depths ( $k_c d > 1.36$ ) – the formation of freak waves up to the physically possible maximum wave height has been observed (cf. Tab. 3.3).
- The higher the initial steepness, the shorter the distances the wave train has to pass to reach the maximum amplification.
- The limited water depth influences the formation process significantly – the smaller the relative water depth  $k_c d$ , the longer the maximum amplification distance.
- The NLS equation provides the basis for the generation of breather-type freak waves (i.e. boundary condition at the wave board), but deviations from its predictions will be observed (especially for large steepness) in the course of wave propagation.
- The non-linear numerical wave tank WAVETUB is applicable to the simulation of non-linear wave propagation, in particular to the simulation of long distances and varying water depths which cannot be covered by test facilities.

The obtained results are exclusively related to the steepness since the shape of the wave group envelopes is kept constant (except amplification). Therefore, the investigated exaggerated breathers are not representing exact solutions. However,

### 3. Extreme Waves

---

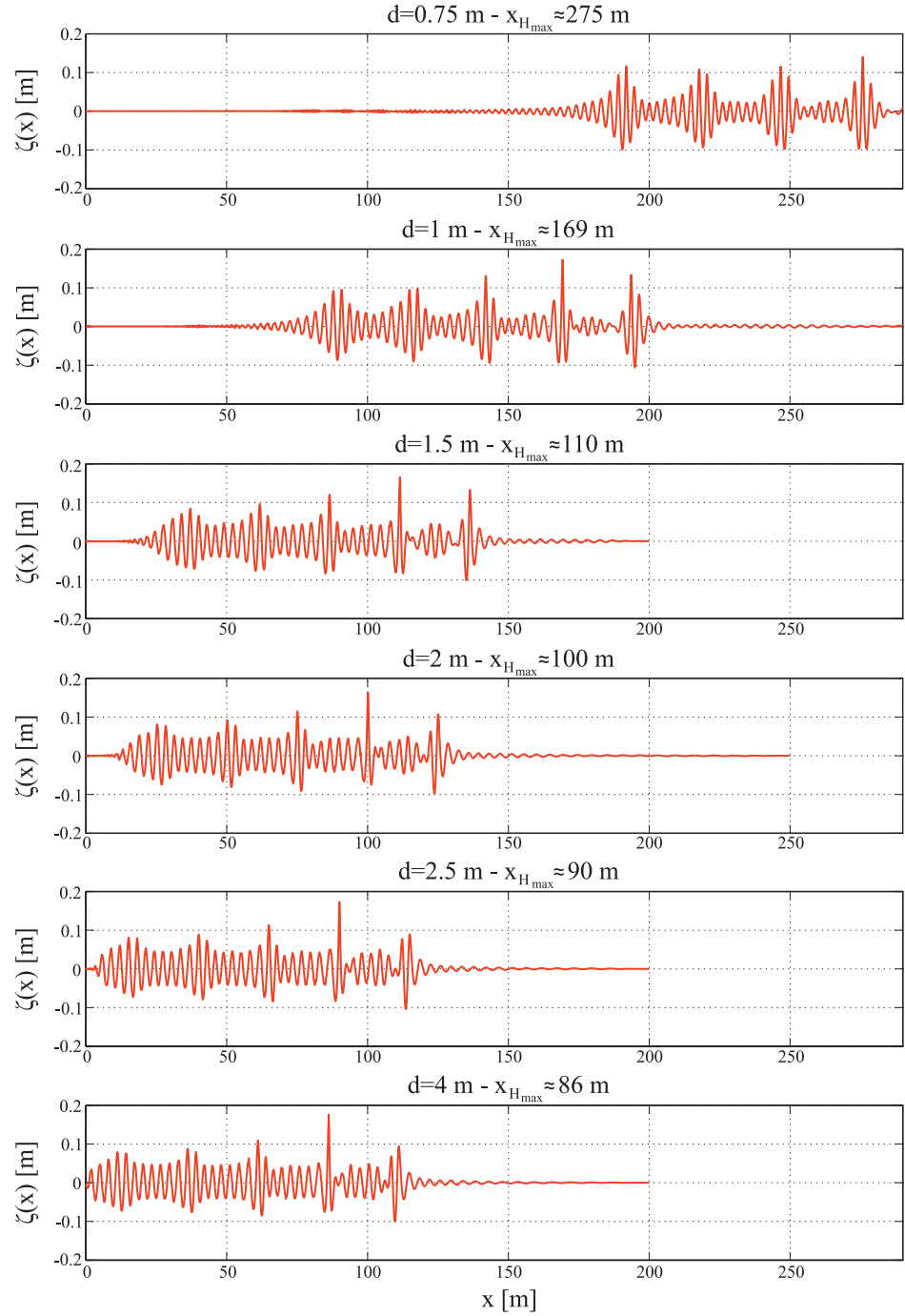


**Figure 3.12.:** WAVETUB results for the  $T_c = 1.4\text{s}$  breather with the smallest initial steepness: surface elevation snapshots at the time of occurrence of the first maximum wave height for the different investigated water depths – the water depth increases from top to bottom (Clauss et al., 2011).

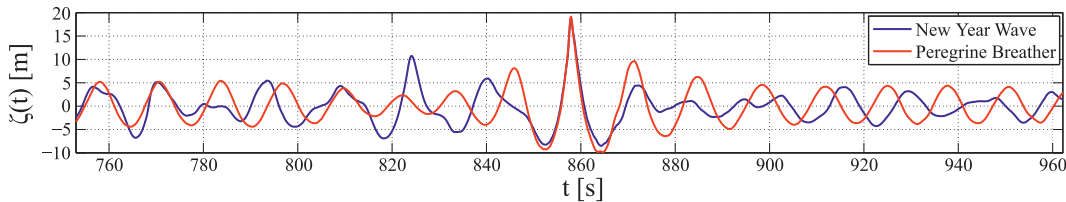


**Figure 3.13.:** New Year Wave vs. Peregrine breather – measured registrations at target location.

general conclusions can be derived regarding the formation process of unstable wave groups in limited water depth as well as regarding the influence of the steepness on it. The breather solution equations themselves take the water depth influence into account and will provide different solutions at the wave board if the water depth and target location varies.

### 3.3. New Year Wave vs. Breather Solution

So far, the spatial evolution of extreme waves has been evaluated. In the next step, the characteristics of such freak waves in terms of kinematics and dynamics are subject to investigation. The objective is to draw conclusions on the differences or similarities between the real-world NYW and the somehow artificial breather-type freak waves. The following investigations are inspired by the fact that one Peregrine breather generated for the wave-structure interaction investigations (see Sec. 5.1) features similar characteristics at target location in terms of wave and crest height as well as crest front steepness compared to the NYW (cf. Fig. 5.1, top diagram in the bottom black rectangle). In addition, the Peregrine breather has been considered as special prototype of freak wave (Shrira and Geogjaev, 2010) which “appears from nowhere and disappears without trace” (Akhmediev et al., 2009).

Figure 3.13 compares the measured registrations of the NYW and the Peregrine breather at target location. The blue curve shows the NYW and the red curve the Peregrine breather. The Peregrine breather is shifted in time domain for a better comparability. As shown in the diagram, this Peregrine breather has been chosen due to the fact that the freak wave at target location features almost the same extraordinarily high wave crest height. However, the Peregrine breather is also characterized by deeper preceding and succeeding troughs as well as shorter up- and downcrossing wave periods, i.e. the Peregrine breather is higher and steeper compared to the NYW. The resulting consequence on wave-structure interaction is presented in Sec. 5.1.

The test campaign addresses the investigation of the pressure and velocity field. The combined pressure and velocity measurements have been conducted in the seakeeping basin at Technische Universität Berlin (see Annex A for details). The

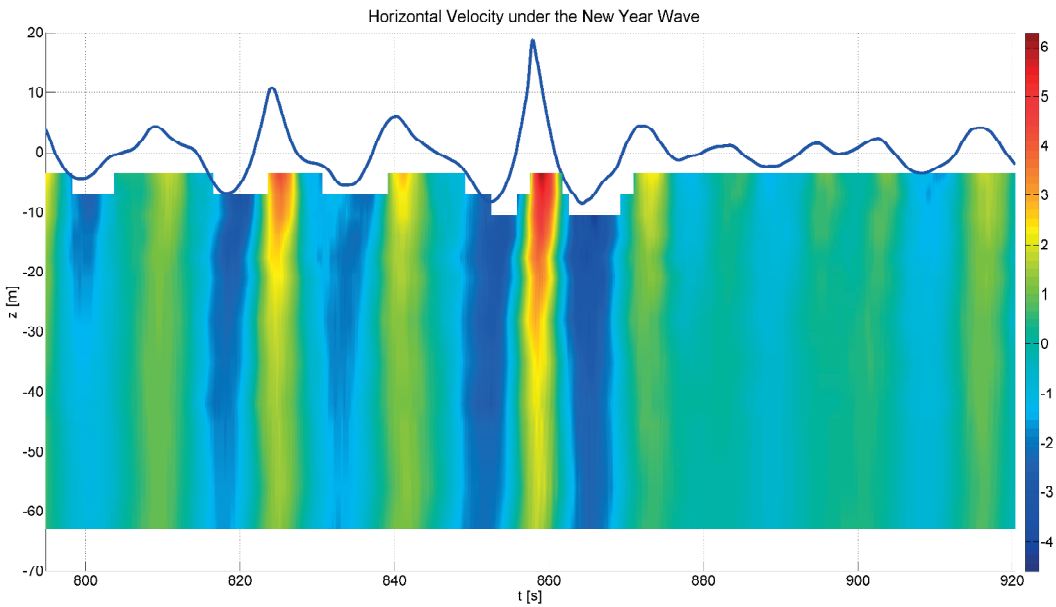
dynamic pressure as well as the particle velocities (horizontal and vertical) of the NYW and the Peregrine breather are systematically measured at different vertical positions up to the still water level and for some cases also above, up to the wave crest. The choice of the target location is obvious as both wave sequences feature breaking extreme waves at the same position.

The pressure measurements are conducted with a pressure transducer (Bell & Howell, type BHL 4104-00-05110). Simultaneously, the particle velocities are measured by an ultrasonic flow meter featuring the measurement of the particles' velocity in three orthogonal planes (Denshi Kogyo Co. LTD, type DS-102S). Both sensors are mounted on a vertical semi-beam which is adjustable in height for the investigation of different water depths. The sensors are mounted, therefore, in such a way that the vertical measuring plane is identical and the measuring points are far enough from each other for unaffected operation. However, the geometry and measurement principle of the utilized sensors limit the operational range of the investigations. The ultrasonic flow meter cannot be used above still water level due to the measurement principle. In addition, only a short emerging in wave troughs can be compensated. The pressure sensor on the other side can be utilized above the still water level, but needs a minimum impact time interval of the wave crest to produce reasonable and trustworthy data. Both sensors can not be utilized near the bottom of the seakeeping basin due to the geometry of the sensors, with the pressure sensor being far less applicable in this respect.

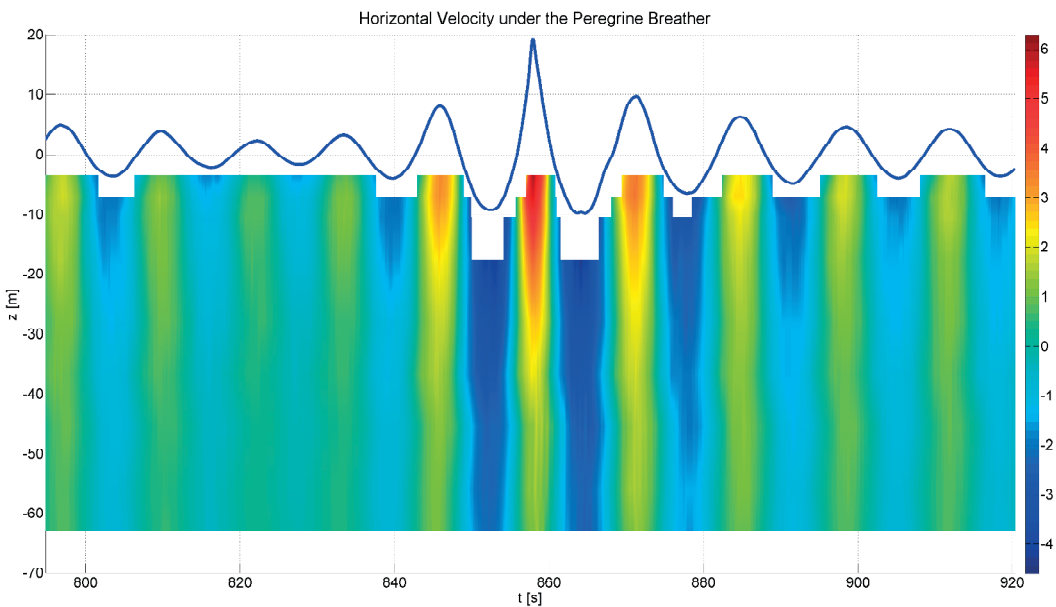
Figure 3.14 presents coloured parametric surface plots of the measured horizontal velocities under the NYW (Fig. 3.14(a)) and the Peregrine breather (Fig. 3.14(b)). The axis of abscissae illustrates the time domain – only a short interval around the target wave is presented. The axis of ordinate illustrates the vertical position, where zero indicates the still water level. The velocities are illustrated in different colours according to their values as assigned in the colour bar on the right side. Additionally, the corresponding surface elevation is plotted for clarity reasons. Both diagrams show the same trend – the highest horizontal particle velocities are observed under the deepest wave troughs and highest wave crests, respectively. The velocity under the target wave crest reaches the highest values for both wave sequences.

Figure 3.15 displays the associated coloured parametric surface plots of the measured dynamic pressure under the NYW (Fig. 3.15(a)) and the Peregrine breather (Fig. 3.15(b)). The diagram is arranged just like the previous one and the dynamic pressure is illustrated in different colours according to their values as assigned in the colour bar on the right side. Comparing the dynamic pressure reveals the same trend – the highest/lowest dynamic pressures are observed under the highest wave crests and deepest wave troughs, respectively. Again, the dynamic pressure under the target wave crest reaches the highest values for both wave sequences.

In the next step, the characteristics under the wave crests are evaluated in detail. Therefore, the horizontal velocity as well as dynamic pressure under the extreme



(a) Horizontal particle velocity [m/s] under the NYW in full scale.

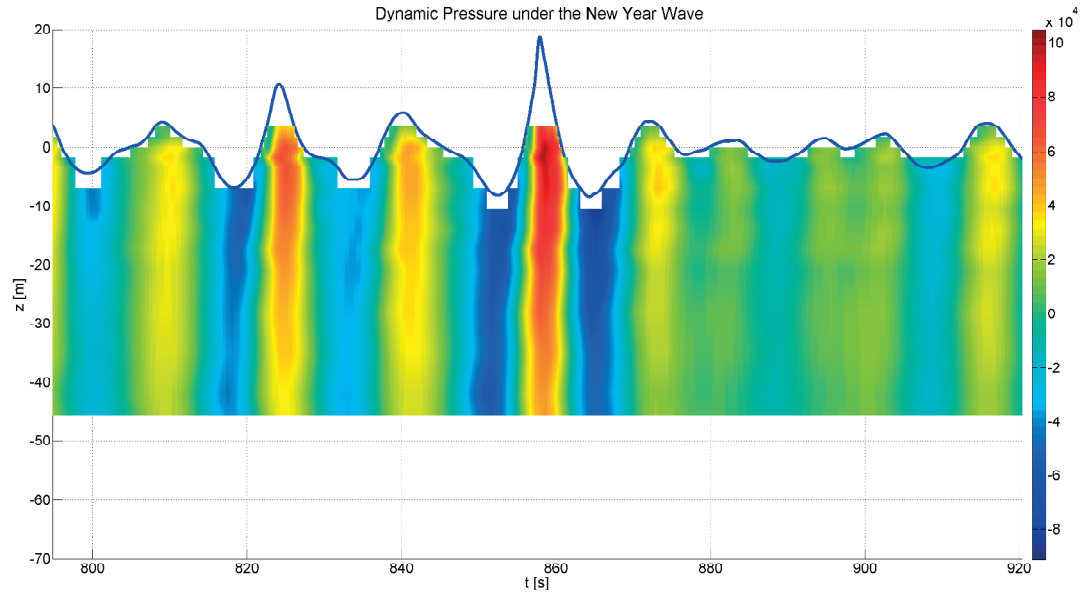


(b) Horizontal particle velocity [m/s] under the Peregrine breather in full scale.

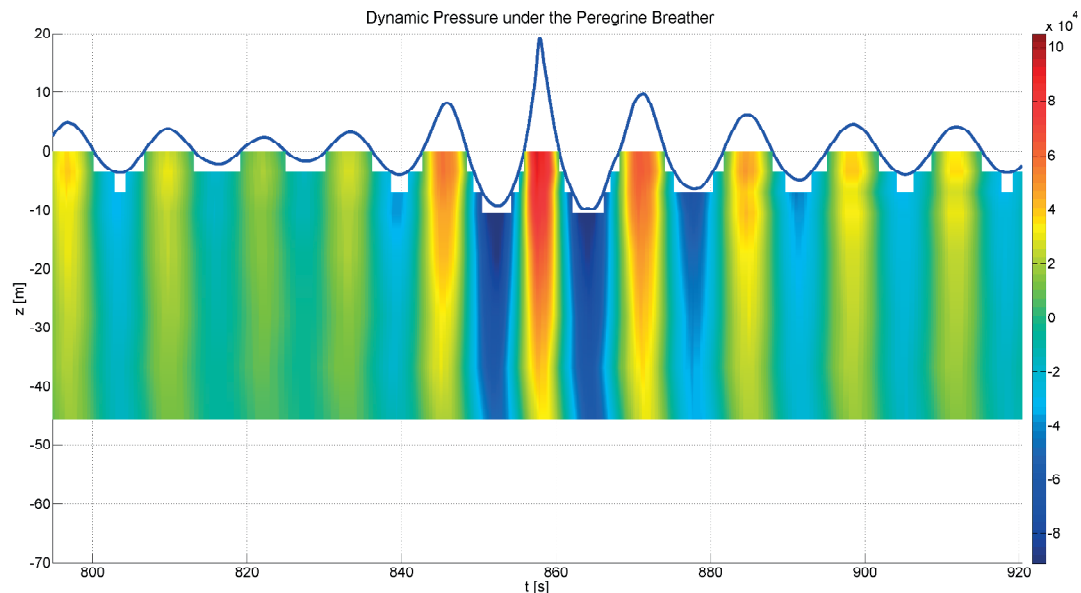
**Figure 3.14.:** Comparison of the horizontal particle velocity between NYW and Peregrine breather.

### 3. Extreme Waves

---



(a) Dynamic pressure [ $\text{Pa}$ ] under the NYW in full scale.



(b) Dynamic pressure [ $\text{Pa}$ ] under the Peregrine breather in full scale.

**Figure 3.15.:** Comparison of the dynamic pressure between NYW and Peregrine breather.

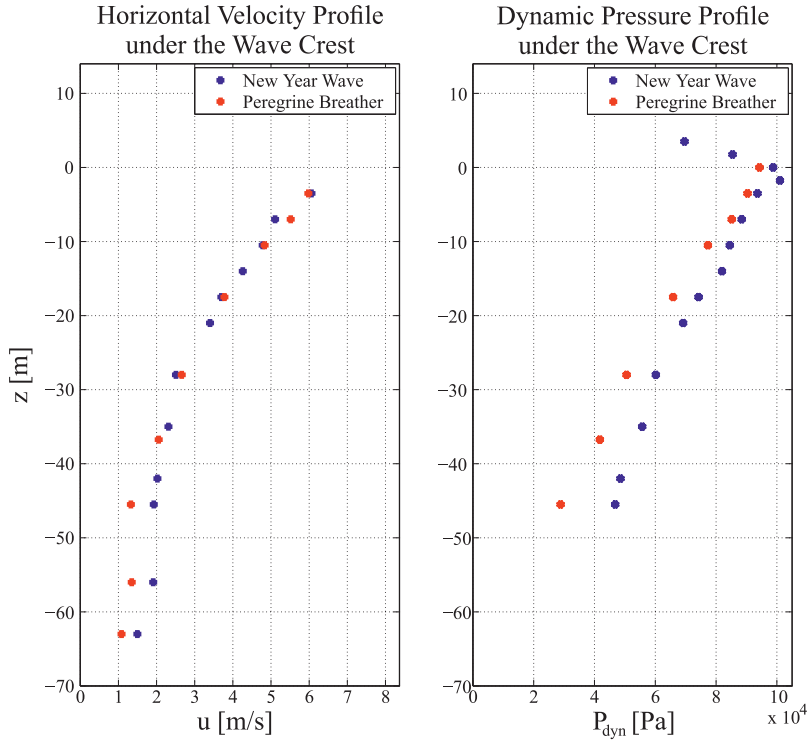


**Figure 3.16.:** Horizontal velocity and dynamic pressure profile under NYW crest and Peregrine breather wave crest (full scale).

wave crest is determined at every measured vertical position to obtain the corresponding vertical profiles. The temporal position of the vertical profile under the wave crest is chosen according to the highest measured quantity. The left diagram in Fig. 3.16 presents the horizontal velocity profiles under the NYW crest (blue dots) and the Peregrine breather wave crest (red dots). The right diagram presents the corresponding dynamic pressure profiles. The axes of abscissa indicates the measured particle velocity (left) and dynamic pressure (right), respectively. The axis of ordinate indicates the vertical position. Again, zero defines the still water level. The water depth of the basin is illustrated completely.

A comparison against the course of the velocity profiles on the left diagram reveals that the first conclusions based on the previous diagrams are confirmed. The velocity profiles are almost identical in the upper half. Afterwards, the profiles diverge steadily up to the deepest measured position, i.e. the Peregrine breather reaches lower horizontal velocities near the bottom compared to the NYW. This trend becomes even more distinctive for the dynamic pressure. Here, the discrepancy at the deepest position is more significant, and both profiles do not overlap in the course of the upper half. The reason for this difference lies in the wave characteristics discussed before (cf. Fig. 3.13) – the effect of the kinematics and dynamics decreasing faster for the Peregrine breather with increasing water depth is due to

the shorter up- and down crossing wave periods. Both diagrams show clearly that the wave crests feature almost the same characteristics near the surface area (up to  $z \approx -30m$ ).

So far, the characteristics of breather solutions are evaluated and compared to the real-world NYW in terms of kinematics and dynamics of the largest wave. Their impact on offshore structures in terms of forces and motions relevant for the design is addressed in Sec. 5.1. Again, deterministic model tests in the Peregrine breather presented above are compared to results in the NYW allowing conclusions regarding the applicability as well as relevance of breather solutions for wave-structure investigations.

### 3.4. Tailored Breather Solution

The previous sections showed that the breather solutions are applicable for the deterministic generation of tailored extreme waves. In addition, it becomes apparent that the breather solutions feature similar characteristics compared to real-world reproductions. This denotes that the breather solutions represent a promising alternative to real-world freak wave investigations in terms of model tests. In particular, due to the fact that real-world reproductions are very time-consuming regarding the generation process in contrast to the availability of an analytical breather solution at the wave board.

Naturally, the next step is to exploit the chances of the breather solutions in terms of tailoring irregular sea states, i.e. integration of the breather solution into an irregular sea state to obtain a single high wave embedded into a random wave field. For this purpose, experiments have been performed in the seakeeping basin at CEHIPAR (see Annex A for details). There, an extract of a Peregrine breather solution (at the wave board) is integrated into an irregular sea state with random phases in such a way that the irregular waves surround the breather. Afterwards, the tailored surface elevation at the wave board is multiplied with the wave maker RAO in frequency domain and subsequently transformed back into time domain for the determination of the wave maker control signal. Figure 3.17 top shows the determined wave maker motion. The extract of the Peregrine breather between  $t = 300s$  and  $t = 500s$  is obviously. This extract has been selected by preceding experimental investigations in order to ensure that the highest wave of the Peregrine breather occurs at the target location ( $x = 50m$ ). The centre and bottom diagram in Fig. 3.17 presents the experimental results. The centre diagram shows the registration at  $x = 10m$  and the bottom diagram at  $x = 50m$ . The Peregrine solution provides already a high single wave within the breather sequence at the wave board due to the short distance between wave maker and target location. At target location, the high single wave reaches its maximum wave height and the surrounding waves merge to an irregular wave shape.

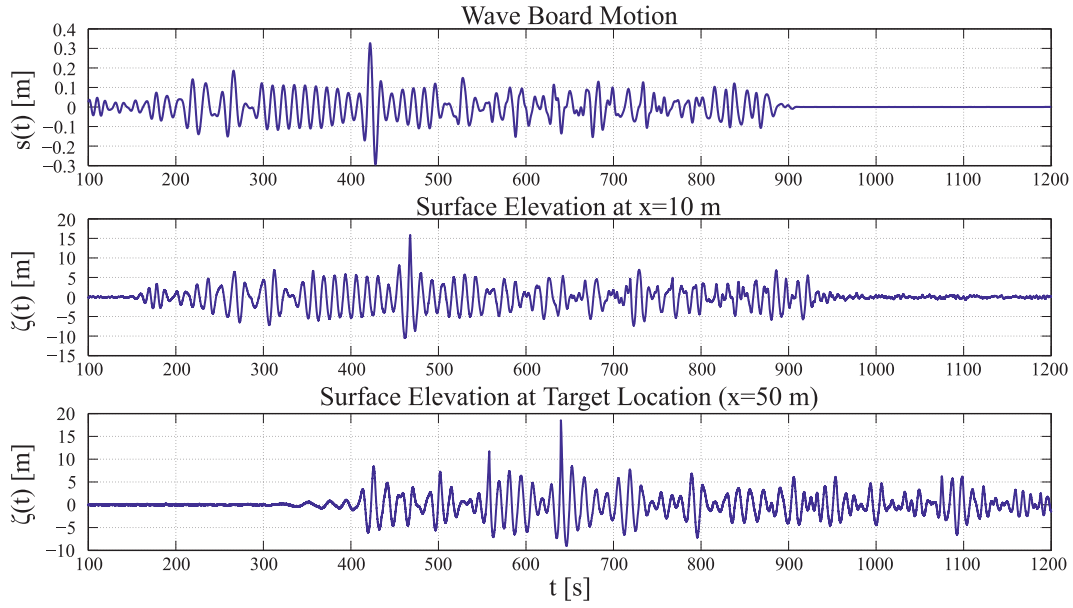


**Figure 3.17.:** Generation of a tailored Peregrine Breather – integration of a Peregrine Breather into an irregular sea state. The top diagram presents the wave board motion, the centre diagram the surface elevation at  $x = 10\text{m}$  in front of the wave maker and the bottom diagram the surface elevation at target location ( $x = 50\text{m}$ ).

Again, similar to the investigations presented in Sec. 3.2, the integrated Peregrine breather is preselected in such a way as to obtain a single high wave at the target location which features an almost identical characteristic compared to the NYW. Figure 3.18 presents comparison between the registrations of the tailored Peregrine breather and the NYW at target location showing a good agreement regarding the target freak wave. Again, the Peregrine breather related freak wave is characterized by deeper preceding and following troughs as well as shorter up- and downcrossing wave periods, i.e. the tailored Peregrine breather is higher and steeper compared to the NYW (cf. Sec. 3.3).

Figure 3.18 proves that the breather solutions are capable to tailor irregular sea states including a high single wave as well as that the solutions can be applied for the deterministic reproduction of real-world scenarios.

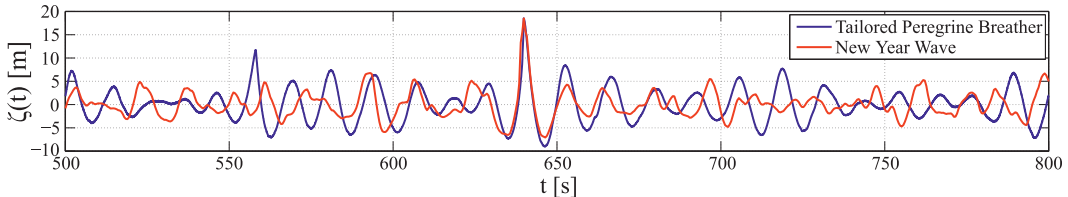


**Figure 3.18.:** Comparison between the real-world New Year Wave and the tailored Peregrine breather at target location.



## 4. Wave-Structure-Interaction

The determination of the behaviour of offshore structures in waves is in a similar vein complex as the description of the waves itself. The oscillating loads of the waves acting on the submerged part have to be determined in order to obtain the associated response. Thus, an analytical solution is, analogue to the water wave problem, not available. Different approaches are applied for the evaluation of offshore structures – from simple and fast linear methods to fully non-linear calculations. Thereby, the selection of appropriate wave-structure interaction analysis tools depends on the level of non-linearity to be reached as well as on the computational time available. Highly non-linear CFD methods allow sophisticated simulations at advanced level but due to the high computational effort, only selected cases can be analysed limiting a holistic application in the design process. Similar to the water wave problem, the approaches used for the determination of the exciting wave forces are in the majority of cases based on potential flow theory. Thereby, the most commonly used linear solution results in RAOs applying the standard model of ocean waves (cf. Sec. 2.3) which offers an efficient procedure for the fast holistic evaluation of a design. In particular, the evaluation of the applicability of a design for certain sea areas can be done very fast by linear stochastic analysis.

This chapter starts with a brief introduction of the theoretical background of the wave-structure interaction analysis relevant for this thesis (Sec. 4.1) – a holistic mathematical description of the wave-structure interaction problem can be found in classical text books, e.g. Newman (1977). Afterwards, the numerical methods used in this thesis are presented. The numerical investigations are conducted in frequency and time domain. For frequency domain calculations the radiation-diffraction code WAMIT (Wave Analysis at Massachusetts Institute of Technology, WAMIT (1994)) is applied (Sec. 4.2), which is a well established linear potential theory approach (see Newman (1977)). The second application is the non-linear time-domain strip theory code from IST (Instituto Superior Tecnico Lisbon, Fonseca and Guedes Soares (1998a,b), Sec. 4.3). The standard model of ocean waves adapted to offshore structure dynamics is introduced in Sec. 4.4 enabling stochastic frequency domain investigations (Sec. 4.4.1) as well as deterministic time domain investigations (Sec. 4.4.2). This chapter ends with a brief review of the state of the art design wave concepts (Sec. 4.5).

## 4.1. Hydrodynamic Analysis

The basic principle for calculating the response of a structure is Newtonian mechanics – the sum of all forces (internal and external) is directly proportional to, and in the same direction as, the acceleration of the body – resulting in six differential equations of motion for stable, linear systems (Lewis, 1989),

$$(M + A) \cdot \ddot{\underline{s}} + B \cdot \dot{\underline{s}} + C \cdot \underline{s} = \underline{F}_e. \quad (4.1)$$

The underline marks a vector with six components according to the six degrees of freedom,  $M$  is the mass matrix,  $A$  the hydrodynamic mass matrix,  $B$  the damping matrix,  $C$  the restoring forces matrix and  $F$  the excitation forces and moments matrix. The system matrices are of dimension  $[6 \times 6]$  according to the number of modes of motion. The total force acting on an offshore structure in waves results from the integration of the dynamic pressure on the wetted surface of a submerged body  $S_b$ ,

$$F_{dyn} = \iint_{S_b} p_{dyn} \underline{n}^* dS_b. \quad (4.2)$$

The main force components are

**Froude-Krylov force** – due to the pressure field within the undisturbed wave field

**hydrodynamic mass force** – arousing from the pressure field due to relative acceleration between water particles and structural components

**potential damping force** – arousing from the pressure field due to relative velocity between water particles and structural components

**viscous drag force** – arousing from the pressure field due to wake on the downstream side caused by relative velocity between water particle and structural components

Once the exciting forces and hydrodynamic coefficients of the floating structure are known, the response can be determined. Thereby, offshore structures can be classified in hydrodynamic transparent ( $D/L < 0.2$ ) or hydrodynamic compact structures ( $D/L > 0.2$ ), i.e. if the characteristic dimension D of the structure is greater than 20% of the wave length L the structure is hydrodynamic compact. In this thesis hydrodynamic compact structures are exclusively considered, but for the sake of completeness also the theoretical background for hydrodynamic transparent structures is briefly described below.

### 4.1.1. Hydrodynamic Transparent Structures

Transparent structures are not affecting the encountering wave field, i.e. the structure response to the waves generate no or only small waves. In that case, the forces acting on the submerged body can be calculated using the Morison equation (Morrison et al., 1950). This empirical formula has been introduced originally for fixed, vertical cylinders,

$$dF_x = (f_m + f_d)dz = C_m \frac{\pi D^2}{4} dz \frac{\partial u}{\partial t} + C_d \frac{\rho}{2} D dz |u| u, \quad (4.3)$$

and has been generalized by Clauss et al. (1992) for arbitrary orientated structural components

$$dF_N = \underbrace{\rho \frac{\pi D^2}{4} ds \frac{\partial \nu_N}{\partial t}}_{\text{Froude-Krylov force}} + \underbrace{C_a \rho \frac{\pi D^2}{4} ds \frac{\partial u_{RN}}{\partial t}}_{\text{Hydrodynamic mass force}} + \underbrace{C_d \frac{\rho}{2} ds |u_{RN}| u_{RN}}_{\text{Viscous drag force}}. \quad (4.4)$$

The Morison equation consist of an inertia term (Froude-Krylov-force and hydrodynamic mass force) and a non-linear drag force term. The forces depend on inertia and drag coefficients, which can be determined experimentally (cf. Clauss et al. (1992)). Drag effects are only relevant for larger values of  $KC = \pi H/D$  (deep water), and dominate at values greater than 40 (Clauss et al., 1992). The Keulegan-Carpenter-Coefficient  $KC$  gives the ratio of the circumference of the orbital path of a water particle to cylinder diameter at still water level. This shows that the inertia forces are dominant for many offshore structure, particularly, for relatively large structures.

### 4.1.2. Hydrodynamic Compact Structures

Compact structures are significantly affecting the encountering wave field. Two effects can be observed, scattering and radiation of the waves, which are both generally called diffraction. Scattering means that due to presence of a compact structure the incident wave field will be deflected and reflected. The second effect, radiation, comes from the fact that a moving compact structure will generate waves which propagate away circularly from the structure. The energy, required for the generation of the radiation wave field, is extracted from the kinetic energy of the moving structure. Thus, the body motion is damped, which is called potential damping. Drag forces on compact structures have only marginal impact and can be neglected (except for the damping of roll motions).

Analogue to the water wave problem, the flow around the structure (cf. Eq. 4.2) can be described by superposition of independent potentials (linearisation of the problem) assuming an ideal fluid,

$$\Phi = \Phi_0 + \sum_{j=1}^6 \Phi_j + \Phi_7, \quad (4.5)$$

with  $\Phi_0$  the incident wave field potential,  $\Phi_j$  the radiation wave field potential due to motion  $j$  and  $\Phi_7$  the scattering wave field potential.

The boundary value problem of the unknown potentials (Eq. 4.5) has to be determined by numerical procedures. Different potential flow procedures have been introduced mainly based on boundary element methods. They offer the exclusive discretization of the boundary of the domain (surface and hull of offshore structure), which significantly reduces the computational time. The different methods can be distinguished as two-dimensional and three-dimensional methods. The two-dimensional methods, also called 2-D strip theory methods, subdivide the submerged three-dimensional body into a finite number of rigidly connected transverse slices at which the hydrodynamic coefficients are determined. The three-dimensional methods, also called 3-D panel methods, discretize the submerged three-dimensional body into a finite number of N panels at which the unknown potentials are assumed to be constant.

A detailed overview on the different methods as well as its mathematical background is beyond the scope of this thesis, details can be found for instance in Newman (1977) as well as Journée and Massie (2000). For this thesis two different numerical methods have been applied – the 3-D panel code WAMIT (Sec. 4.2) and the 2-D strip theory code from IST (Sec. 4.3). The target of all methods is to solve the equation of motion (Eq. 4.1) by determining the hydrodynamic forces, damping and added mass numerically resulting in the motion of the structure.

## 4.2. WAMIT

WAMIT is a radiation/diffraction program for the evaluation of wave-structure interaction at zero speed in frequency domain (Newman, 1977; WAMIT, 1994; Lee, 1995). It is assumed for the 3-D panel method that the wave heights as well as the ship response are small; thus, the boundary value problem can be linearised. In addition, this assumption allows the discretization of the submerged body exclusively, reducing the computational effort.

WAMIT can simulate single or multi-body problems for arbitrary water depths, where the structures can be arbitrarily located within the entire fluid domain – from free surface to submerged and bottom mounted bodies. Dynamic analysis can be conducted with freely floating, restrained or for fixed bodies.

The radiation and diffraction potentials on the submerged hull are computed by applying Green's second identity, with the free surface source-potential represented by Green's function (Newman, 1985, 1986). The submerged hull is discretized into a finite number of low-order panels (flat quadrilateral elements) and the boundary value problem has to be solved at each panel. The centre of each panel is the collocation point and the potentials are assumed to be constant over the whole panel.

WAMIT offers to determine several quantities for the 6 degrees of freedom rigid body motion such as hydrostatic, damping and added mass coefficients, motion amplitudes and phases, hydrodynamic pressure and fluid velocity on the body surface and the fluid domain as well as drift forces. In addition, WAMIT allows the analysis of generalized modes. One application is the definition of flexural ship bending modes, by what the associated structural deformations due to the wave-structure interaction can be calculated.

Generally, WAMIT is a widely accepted, validated numerical tool for hydrodynamic analysis and proven to be suitable for a multitude of applications.

### 4.3. IST Code

The IST Code is a non-linear time domain strip theory solver developed for the evaluation of the wave-structure interaction of ships advancing in waves with constant speed (Fonseca and Guedes Soares, 1998a,b). The cruising vessels can be investigated in regular and irregular sea states. In addition, Fonseca et al. (2006, 2008) applied a method to investigate the ship response in predefined, deterministic wave sequences. This enables the investigation of tailored critical wave sequences as well as real-world registrations of extreme waves.

The strip theory hypothesis is applied for the determination of the rigid body motions and associated global structural loads, i.e. the longitudinal hydrodynamic unsteady forces are negligible. Additionally, only heave and pitch motions are considered. It is assumed that heave and pitch are relatively small, but the relative motions between the ship and the wave elevation can lead to large variations of the submerged volume with associated non-linear effects. For this purpose the ship hull is discretized into rigidly connected transverse slices up to the weather deck taking non-linear hydrodynamic effects on the hull structure above mean water level into account.

Assuming a slender hull at slow forward speed and sufficiently small amplitudes of the unsteady motions and incident waves, the potential results in

$$\Phi = -Ux + \Phi_S + \Phi_0 + \sum_{j=1}^6 \Phi_j + \Phi_7. \quad (4.6)$$

In comparison to Eq. 4.5, two new terms are introduced due to the advancing ship. The first two terms in Eq. 4.6 represent the steady flow due to the presence of the ship advancing through the free surface, with  $U$  being the forward speed of the ship and  $\Phi_S$  the steady perturbation potential. The non-linear effects on the vertical motions and global structural loads are assumed to be dominated by buoyancy effects, therefore Froude-Krylov (exciting forces) and hydrostatic forces (restoring forces) are non-linear, while the radiation and diffraction forces are kept linear. The radiation forces are derived with impulse response functions (Cummins, 1962)

which take memory effects into account. The memory functions and radiation restoring coefficients are determined via Fourier analysis. The frequency dependent added mass and damping coefficients are calculated with a strip theory method (Salvesen et al., 1970). The wave potential is decomposed into harmonic wave components and the associated exciting forces are divided into diffraction and Froude-Krylov forces. The diffraction forces are handled linearly in frequency domain. The Froude-Krylov forces and the hydrostatic forces (restoring forces) are calculated over the “exact” wetted surface at each time step accounting for the non-linear effects of the waves acting on the ship.

The difference between the inertia forces and the sum of the hydrodynamic forces acting on the hull ahead of a cross section results in the dynamic global structural loads at this cross section in terms of vertical wave shear forces and vertical wave bending moment. Forces due to green water on deck, contributing to motions and structural loads (Buchner, 1995), are taken into account. Further details can be found in Fonseca and Guedes Soares (1998a,b).

The IST code is well established and validated; proven to be suitable for investigations on extreme waves and responses (Fonseca and Guedes Soares, 2002; Clauss et al., 2004; Rajendran et al., 2011).

#### 4.4. Standard Model of Offshore Structure Response

The application of spectral analysis in ship dynamics started with the fundamental publication of St. Denis and Pierson (1953). Assuming a steady state system, the sea state as well as the response is interpreted as a superposition of an infinite number of harmonic elementary components. As a consequence, the system behaviour of offshore structures is describable by a set of RAOs. RAOs describe the ratio between response and excitation,

$$RAO(\omega_j) = \frac{s_{aj}(\omega_j)}{\zeta_{aj}(\omega_j)} \cdot e^{i\hat{\phi}_j(\omega_j)}, \quad (4.7)$$

assuming a linear response behaviour of the system – the harmonic excitation of a structure due to a wave of frequency  $\omega_j$  yields a phase shifted harmonic response of the same frequency.  $RAO(\omega_j)$  is the response amplitude operator,  $s_{ja}(\omega_j)$  the amplitude of the response,  $\zeta_{ja}(\omega_j)$  the amplitude of the excitation and  $\hat{\phi}_j$  is the phase shift between excitation and response.

Fig. 4.1 illustrates the application spectrum of the standard model of offshore structure response (cf. Fig. 2.3) – left represents frequency domain and right represents time domain. The analytical basis, as aforementioned, is the Fourier transform which provides the link between frequency domain and time domain. The application of RAOs enables a fast, efficient and complete description of the hydrodynamic characteristics of offshore structures. Frequency domain investigations

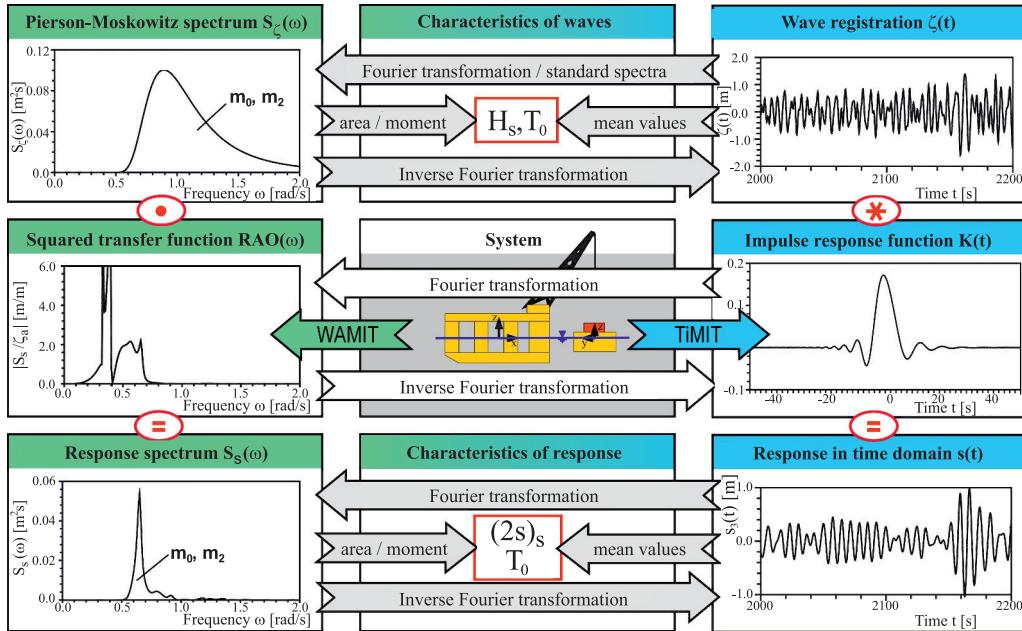


**Figure 4.1.:** Standard model of offshore structure response: sea state as well as response are interpreted as superposition of harmonic component waves enabling investigations in frequency as well as time domain. Source: Jacobsen (2005), modified.

offer a holistic evaluation of offshore structures including short-term and long-term statistics as well as annual downtime. Time domain investigations are essential for task-related evaluations of cause-reaction effects in deterministic tailored wave sequences. Both approaches are briefly described in the following paragraphs.

#### 4.4.1. Stochastic Frequency Domain Investigations

The spectral density  $S_\zeta(\omega)$  (Fig. 4.1, top left) represents the energy distribution of a sea state as a function of wave frequency  $\omega$ . In analogy to the wave spectrum  $S_\zeta(\omega)$ , the response spectrum  $S_S(\omega)$  (Fig. 4.1, bottom left) represents the energy distribution of the output signal. Accordingly, the spectral approach introduced for the sea state description can also be directly applied for the response spectrum (cf. Sec. 2.3). Wave and response spectra are related by

$$S_S(\omega) = |RAO(\omega)|^2 \cdot S_\zeta(\omega). \quad (4.8)$$

Similar to the significant wave height  $H_s$ , a significant force or motion double amplitude  $(2s)_s$  follows from the response spectrum related to certain values of  $H_s$  and  $T_0$ :

$$(2s)_s(H_s, T_0) = 4 \sqrt{\int_0^\infty S_S(\omega) d\omega}. \quad (4.9)$$

Relating the significant double amplitude with  $H_s$  yields the significant RAO,

$$RAO_s(T_0) = \frac{(2s)_s(H_s, T_0)}{H_s}, \quad (4.10)$$

which is a function of zero-upcrossing period only.

Supposing that the response is a narrow banded random process (stationary and ergodic) allows the application of Rayleigh statistics – analogue to the sea state statistics. The statistical properties introduced for the seaway (p. 16–17) are directly transferable to the response by replacing  $H$  with  $(2s)$ ,  $H_s$  with  $(2s)_s$  and  $H_{max}$  with  $(2s)_{max}$ .

Thus, the operability of an offshore structure can be determined by utilizing the extreme value statistics to the spectral approach of the response. Firstly, the most probable maximum double amplitude can be determined,

$$(2s)_{max}(H_s, T_0) = 1.86 \cdot (2s)_s(H_s, T_0), \quad (4.11)$$

choosing a statistical parameter of  $H_{max}/H_s = 1.86$  exemplary. The suitable selection of this parameter is a delicate problem as it should be balance safety and efficiency (cf. Fig. 2.4). The significant double amplitudes are appropriate hydrodynamic measures of merit criteria for the design process, whereby  $(2s)_{max}(H_s, T_0)$  is only a statistical magnitude and expresses the most probable value.

Equation 4.11 is used to take long term statistics into account for the determination of the operational range of the offshore structure. Based on known limiting values  $(2s)_{max}$  of the design, the tolerable significant double amplitude  $(2s)_{s,tol}$  can be determined from the following statistical relation (adapted from Eq. 4.11)

$$\frac{(2s)_{max}}{(2s)_{s,tol}} = 1.86. \quad (4.12)$$

Again, the statistical probability of 1.86 between maximum and significant value is chosen exemplary, other values may be more appropriate depending on the investigated problem. However, the tolerable significant wave heights  $H_{s,tol}(T_0)$  are obtained on the basis of the tolerable significant double amplitude,

$$H_{s,tol}(T_0) = \frac{(2s)_{s,tol}}{RAO_s}. \quad (4.13)$$

The tolerable significant wave heights can be directly included into a wave scatter diagram for a defined sea area in order to highlight feasible and unfeasible sea states for operation. From this, the downtime of the structure is calculated by summation of all relevant probabilities over the infeasible region.

#### 4.4.2. Deterministic Time Domain Investigations

Deterministic time domain investigations are essential for the evaluation of tailored extreme sea states, critical wave groups and extreme response in terms of design wave concepts. Following Fig. 4.1, the deterministic wave sequence in time domain (top right) can be transformed by means of FFT to arrive at the spectral density  $S_\zeta(\omega)$  of the wave sequence (top left) in frequency domain. Applying Eq. 4.8, the spectral density of the response  $S_S(\omega)$  (bottom left) can be re-transformed into time domain by means of IFFT obtaining the corresponding response (bottom right).

A more sophisticated approach is the direct calculation of the corresponding response in time domain (Fig. 4.1 right) by applying impulse response functions (Cummins, 1962). The impulse response function  $K(t)$  takes memory effects of the moving vessel into account and represents the inverse Fourier transform of the RAO (Fig. 4.1 centre right),

$$K(t) = \frac{1}{2\pi} \int_{-\infty}^{\infty} RAO(\omega) \cdot e^{i\omega t} d\omega. \quad (4.14)$$

The time dependent response (Fig. 4.1 bottom right) is calculated by convolution of the impulse response function with arbitrary, tailored wave trains,

$$s(t) = \int_{\hat{\tau}=-\infty}^{\infty} K(t - \hat{\tau}) \cdot \zeta(\hat{\tau}) d\hat{\tau}, \quad (4.15)$$

yielding the so-called F2T+ approach (Jacobsen, 2005). Jacobsen (2005) presented this advanced F2T+ approach showing by means of a hydrodynamically coupled multi-body offshore crane operation that the method allows fast and effective time domain simulations including memory effects.

### 4.5. Design Wave Concepts

In critical wave conditions, the linear model implies uncertainties due to non-linear response behaviour. In this case, non-linear simulations become crucial to obtain reliable limiting values. Non-linear simulations at advanced level are (up to now) not practical for holistic design approaches due to the computational time needed per simulation. Hence, it is difficult to obtain accurate extreme value estimates by long-term extreme value statistics as sufficiently long simulations are necessary (but impractical) to reduce statistical uncertainties. Contrary, reducing the level of accuracy of the non-linear simulations enables very long simulation durations in an adequate time span resulting in very small statistical uncertainties, but increases the numerical model and extreme value uncertainties, respectively.

Tailored wave sequences of short duration can be applied to avoid statistical uncertainties and impractical simulation time spans. These critical wave sequences, also called critical wave episodes, correspond to a specific extreme wave event the structure will experience during its lifetime. The deterministic identification of such critical (design) wave sequences leading to a certain maximum response is still a key issue.

The application of *Regular Design Waves* is the simplest design wave concept. Long-term extreme values based on linear theory are used as input. By selecting a certain wave period (e.g. peak of the linear transfer function), the amplitude of the regular wave can be determined by division of the long-term extreme value with the linear transfer function (e.g. Adegeest et al. (2000)). This kind of design wave is quite questionable as the real-world wave leading to an extreme response will significantly differ from such a regular design wave.

*Critical Wave Episodes* (CWE) (Torhaug et al., 1998) are determined by very long realizations of the ship response combining linear transfer functions and irregular sea states. Wave sequences within the realization which lead to extraordinarily large responses are defined as critical wave episodes. By randomly varying the phase distribution of the input sea state, a multitude of different CWE's can be identified. Afterwards, a number of identified CWE's, the average of all CWE's or the CWE leading to the maximum response can be used for non-linear simulations to obtain conclusions on extreme values.

Advanced methods are based on probabilistic conditioning of critical wave sequences and responses, respectively. The idea is to tailor a short encountering wave sequence in such a way that the obtained wave group represents a most probable critical surface elevation or predefined maximum response. The target of such conditioning is to estimate the extremes of the non-linear response statistics by performing only short non-linear simulations with the identified wave sequences. The main assumption is that the linear theory gives a good indication for extreme events: a wave train that creates a large (non-linear) response in reality is similar to a calculated wave train that creates a large linear response.

The *New Wave* model has been introduced as “A new model for the kinematics of large oceans waves” by Tromans et al. (1991). The New Wave model is based on the standard model of ocean waves and determines the most probable maximum wave crest elevation by conditioning of amplitudes using probabilistic analysis. At the end, the method provides the most probable maximum surface elevation and its associated kinematics for a given sea state. The method assumes a constant mean frequency of the input spectrum independently of the real frequencies of the amplitudes. This simplification can only be seen as a first approximation model (Friis-Hansen and Nielsen, 1995) as the assumption is only adequate for narrow-banded wave processes. Friis-Hansen and Nielsen (1995) extended the New Wave model by also introducing random frequencies in the conditioning process.

This *Most Likely storm Wave* (MLW profile), obtained by conditioning amplitude and frequencies, is subsequently used as a design wave for wave-structure analysis. The basis of such a MLW profile is the definition of a design wave spectrum including the calculation of a set of random wave components representing the spectral properties. The design wave spectrum represents the sea state which gives the most probable linear extreme value. To arrive at the MLW profile, a specific crest amplitude of the critical wave has to be defined and the mean of a set of infinite number of possible realizations is calculated (Friis-Hansen and Nielsen, 1995). Adegeest et al. (2000) pointed out that the “mean response to a set of random realizations will in general not be equal to the response to the mean, or Most Likely, realization”. In addition, memory effects on the response are not taken into account. This denotes that for each selected design study one should evaluate whether the CWE’s, one particular conditioned wave or the MLW profile is applicable.

The *Most Likely Extreme Response* (MLER) can be derived by applying the MLW theory on the response. This denotes that the response spectrum of the structure is used as input instead of the wave spectrum (Adegeest et al., 2000), resulting in the MLER profile. The basic idea is to search for an unfavourable response condition instead for a wave condition, as the MLW must not be the worst case wave regarding extreme responses. Based on the derived response profile the underlying wave sequence can be calculated resulting in the *Most Likely Response Wave* (MLRW) (Adegeest et al., 2000; Dietz, 2004). Combining the MLRW profile with an irregular random background wave yields the *Conditional Random Response Wave* (CRRW), which is particularly suitable for investigations of responses with contributions of transient effects like whipping (Dietz, 2004; Drummen et al., 2009).

A different approach has been presented by Alford (2008) for extreme response estimation. This approach manipulates the phase of the response spectrum by means of an optimization algorithm to obtain a certain maximum response. This tool has been developed for the fast evaluation of a new design in the early design stage.

All these approaches have in common, that using RAOs results in a major advantage, as a critical wave sequence can be determined quickly for subsequent non-linear simulations or model tests. At the same time, the linearity of these procedures is also a drawback since it implies uncertainties due to non-linear response behaviour. The fundamental assumption, that the non-linear response is a correction of the linear response, should be validated under different severe conditions, when non-linear effects are significant (Drummen et al., 2009). In addition, all methods require the definition of response levels to be reached (commonly taken from linear short or long-term statistics) and the resulting wave sequence is directly proportional to this level. This can lead to physically impossible wave sequences regarding wave height and steepness (as Rayleigh statistics are not considering any physical limitation regarding response or excitation).

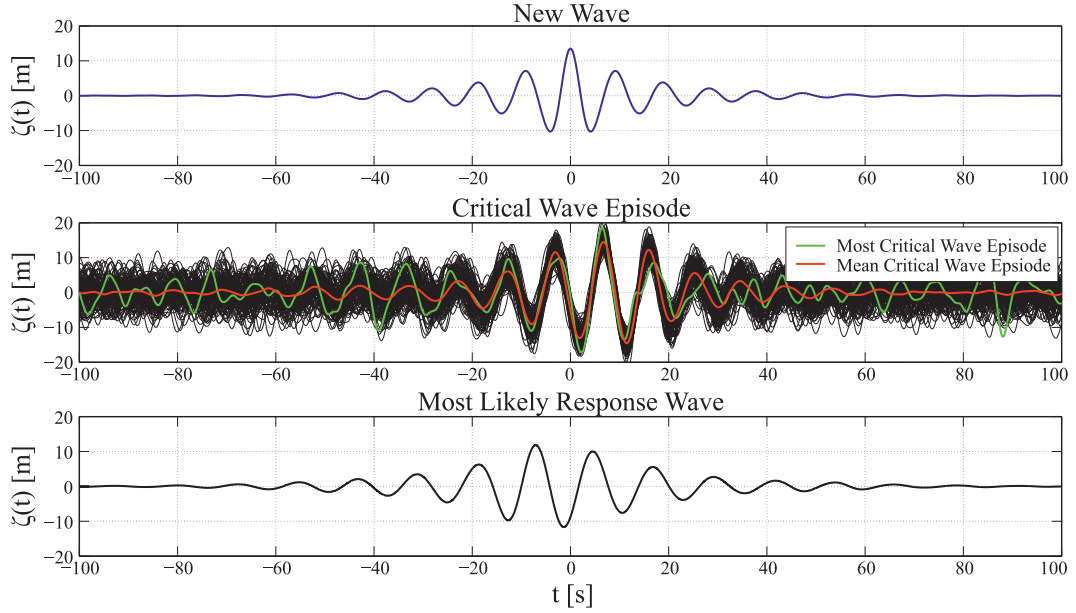


**Figure 4.2.:** Examples of design wave concepts. The top diagram presents the New Wave profile. The centre diagram shows one thousand realizations of Critical Wave Episodes (black curves), the mean of all Critical Wave Episodes (red curve) and the most Critical Wave Episode (green curve). The bottom diagram presents the Most Likely Response Wave profile.

Figure 4.2 presents examples of design wave concepts. The underlying sea state is a JONSWAP spectrum with a significant wave height of  $H_s = 14.5\text{m}$ , a peak period of  $T_p = 12.2\text{s}$  and an enhancement factor of  $\gamma = 3.3$ . The supposed critical response is the vertical bending moment of a LNG carrier. The top diagram shows the New Wave profile. The centre diagram shows one thousand realizations of Critical Wave Episodes (black curves), the mean of all Critical Wave Episodes (red curve) and the most Critical Wave Episode (green curve). The bottom diagram presents the Most Likely Response Wave profile. The obtained wave profiles feature a very similar characteristic – a steep wave group of short duration.

## 5. Extreme Responses

The following chapter addresses the complex problem of tailoring critical wave sequences for response-based design. At the beginning, tailored wave events in terms of freak waves, which are generally critical for all kind of offshore structures, are experimentally investigated. Therefore, the breather solutions introduced in Sec. 3.2 are applied to model tests in Sec. 5.1. For this purpose, a chemical tanker is investigated in breather solutions addressing the vertical wave bending moment amidships. The impact of this new class of freak waves is reviewed against results obtained in the classical real-world NYW to evaluate their relevance for test facilities in terms of experimental design waves.

Tailoring the structure response to arrive at extreme values, which are critical for a specific offshore structure, is a more straightforward approach in terms of identifying critical wave events. In this context, a new design wave concept is introduced in Sec. 5.2. The broad scope of the new response-based identification tool is demonstrated on two typical design examples – one addresses the survivability in terms of maximum vertical bending moment a chemical tanker can experience at amidships (Sec. 5.2.1) and the other the question on the utilisability of a multi-body offshore operation (Sec. 5.2.2). The identified underlying critical wave sequences are experimentally validated and evaluated against design wave concepts as well as breather-type freak waves.

### 5.1. Breather-Type Freak Waves as Experimental Design Waves

Model tests are indispensable for the evaluation of offshore structures due to the fact that the numerical methods available comprise simplifications on different levels (which have to be validated). The scope of application ranges from the determination of the RAOs in frequency domain via time domain investigations in stochastic irregular sea states to tailored wave sequences.

Tailored wave sequences are an important component in the evaluation of a design as they generally represent specific events in terms of structure response. On one hand, these events can be identified by numerical investigation such as design wave concepts, which addresses particular questions. On the other hand, these critical wave events can be of a more general nature such as freak waves embedded in irregular sea states or real-world reproductions. Freak wave events are of particular interest as they are outstanding situations relevant for all offshore structures.

Consequential, the new classes of extreme waves – breather-type freak waves – presented in Sec. 3.2 are promising candidates for new experimental design waves as they feature important characteristics in terms of wave-structure interaction investigations:

- The existence of an analytical solution offers a fast and simple generation of the wave maker control signal.
- The small frequency bandwidth offers the tailored investigation of critical wave lengths in terms of structure response.
- The wave group steepness is variable up to very steep wave groups.

The special feature of the breather-type freak waves is the fact that these solutions offer the possibility to generate extreme wave events at arbitrary wave lengths up to wave breaking at deterministic positions in the basin. This denotes that the wave length of the extreme wave can be adjusted in order to meet a critical length in terms of structure response. Moreover, the breaking breather solution represents the maximum possible wave height at a certain wave length to be suffered by an offshore structure.

Consequently, the breather solutions are applied to wave-structure investigations in the seakeeping basin at Technische Universität Berlin. The investigations are conducted for a chemical tanker at zero speed in head waves and the vertical wave bending moment amidships is addressed. In addition, the chemical tanker is investigated in the real-world NYW for direct comparison between the different classes of freak waves. Table A.2 presents the main dimensions of the chemical tanker and Fig. A.3 the model test setup. Details on the equipped model, the test setup and the suspension system can be found in Annex A.

The following study comprises the generation of the three breather solutions introduced in Sec. 2.4.2 – the Kusnetzov-Ma breather, Akhmediev breather and Peregrine breather. Each solution is used to generate a set of high, steep single waves of different discrete carrier wave lengths. The carrier wave lengths are chosen in order to cover the range of interest in frequency domain in terms of wave-structure interaction – from  $T_0 = 10.5\text{s}$  to  $T_0 = 12.5\text{s}$  full scale. The breather solutions are generated in such a way that the high single wave at target location is as high as physically possible for the defined wave lengths. Target location denotes the location of the subsequent wave-structure investigations, which is approximately  $x = 45\text{m}$  in front of the wave maker. The model is placed in such a way that the target wave reaches its maximum wave height at the forward perpendicular.

Figure 5.1 presents the results of these investigations. Altogether, three different carrier periods are investigated. The individual results of each carrier wave period are labelled with a black rectangle – from top, the shortest, to bottom the longest wave length. The measured surface elevations are shown in the top diagram of each block. The three breather solutions for the same carrier period are compared in

### 5.1. Breather-Type Freak Waves as Experimental Design Waves

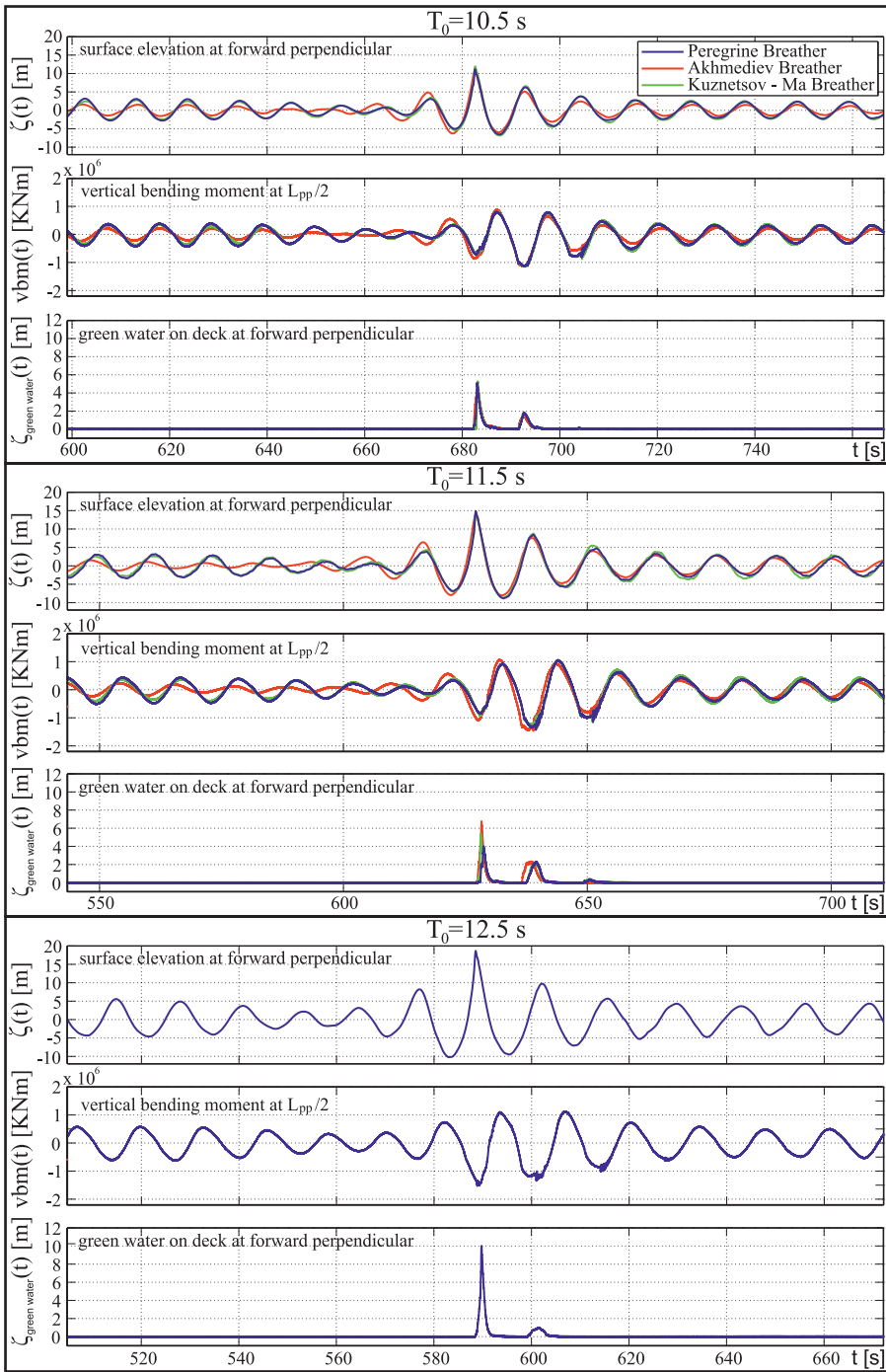


**Figure 5.1.:** Model test results of the breather-type freak wave investigations. The three solutions are investigated with three carrier periods – each block presents one carrier period. The surface elevation is shown in the top diagram of each block, followed by the corresponding vertical wave bending moment. The bottom diagram of each block presents the green water column height at the forward perpendicular.

the same diagram – the blue curves denote the results for the Peregrine breather, the red curves for the Akhmediev breather and the green curves the Kuznetsov-Ma breather. The Peregrine solution is exclusively applied for the longest wave period. The ordinates are equally scaled for all diagrams to simplify the overall picture of the results. The corresponding vertical wave bending moment is presented in the centre diagram of each block. In addition, the green water column height on deck is shown in the bottom diagram of each block.

The overall picture of the presented results shows that all breathers evolved to high, steep single waves at the measuring point. In addition, the surface elevations of the different breather solutions with the same carrier wave length feature an almost identical shape, only the Akhmediev breather shows a slightly different wave propagation in front of the target wave. The height of the presented freak waves increases with increasing carrier wave period, independently of the used breather solution as all waves represent the highest physically possible wave height, i.e. close to the target location all freak waves are plunging breakers. In this context, it is interesting to note that the upcrossing wave periods of the individual freak waves are  $\approx 1\text{s}$  shorter than the (input) carrier periods of the surrounding waves.

The corresponding vertical bending moment reaches maximum values at the moment of the freak wave impact. Even if the shortest carrier wave length ( $T_0 = 10.5\text{s}$ ) represents the worst case in terms of structure response per metre wave height (maximum of the RAO), the highest sagging moment is measured for the longest carrier wave length, as period as well as wave height contribute to the vertical bending moment. The freak wave with the longest carrier wave length reaches a significantly higher maximum wave height before breaking – this freak wave is  $\approx 10\text{m}$  higher than the shortest one. However, the two longer carrier periods reaches almost the same level of maximum sagging values.

Altogether, the experiments show that the breather-type freak waves are outstanding critical events resulting in severe impact on offshore structures. This conclusion is confirmed by the measured green water column heights at the forward perpendicular, which reach impressive values – up to  $10\text{m}$  high wave fronts have been detected, which is as high as a three story building.

#### New Year Wave vs. Breather-Type Freak Wave

So far, the impact of the breather solutions are evaluated by means of model tests. Next, the results are compared to experiments performed in the NYW (cf. Sec. 3.1). The model test setup is identical with the experiments performed for the breather-type freak waves and the target location of the NYW is also at forward perpendicular.

The Peregrine breather shown in the top diagram of the bottom black rectangle in Fig. 5.1 is chosen for this comparison due to the fact that this breather features similar characteristics regarding crest height as well as wave front steepness compared to the NYW. In Sec. 3.3 it has already been shown that this Peregrine

### 5.1. Breather-Type Freak Waves as Experimental Design Waves

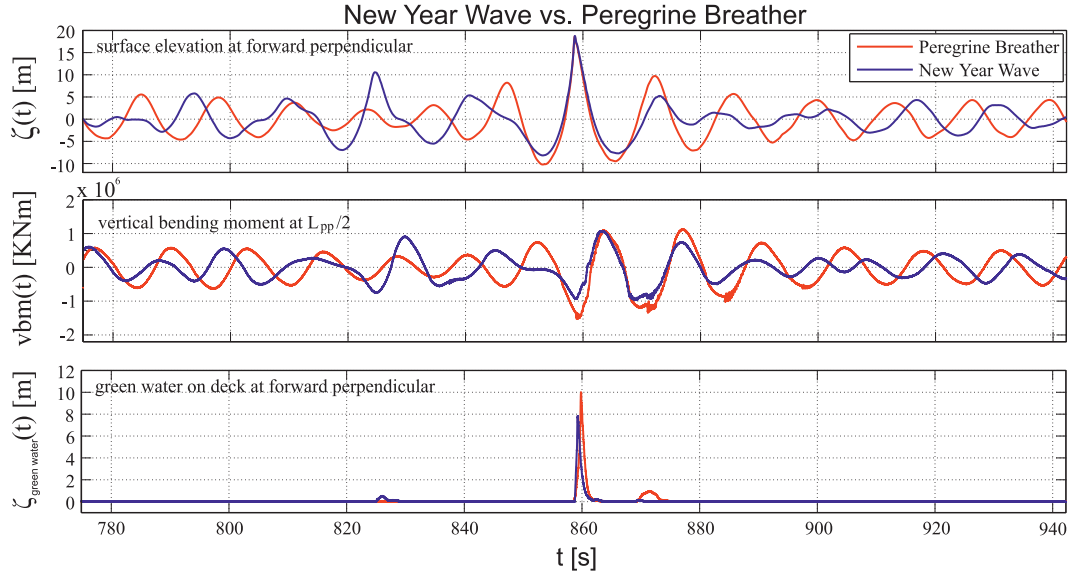


**Figure 5.2.:** Comparison of the experimental results in breather-type freak waves (red curves) and the NYW (blue curves). The top diagram displays the surface elevation, the centre diagram the corresponding vertical wave bending moment and the bottom diagram the green water column height at forward perpendicular.

breather features similar characteristics in terms of kinematics and dynamics under the wave crest. However, the Peregrine breather is also characterised by deeper preceding and following troughs as well as shorter up- and downcrossing wave periods, i.e. the Peregrine breather is higher and steeper.

Figure 5.2 compares the experimental results of the two freak waves – red curves for the Peregrine breather and blue curves for the NYW. The top diagram presents the surface elevation, followed by the corresponding vertical wave bending moment in the centre diagram and the bottom diagram shows the green water on deck column height at forward perpendicular.

Comparing the measured vertical wave bending moment and green water column on deck reveals that the impact of both freak waves is severe, but the impact of the Peregrine breather is significantly more dangerous. The main reason for this observation is the aforementioned difference of the wave characteristics in front of and behind the extraordinarily high wave crest. The Peregrine breather features a more critical characteristic in terms of wave length and height particularly in front of the freak wave crest. In addition, breather solutions feature a symmetrical shape around the freak wave crest resulting in an experimental design freak wave whose critical wave length can be adjusted precisely. This proves that breather solutions represent outstanding critical events in terms of structure response.

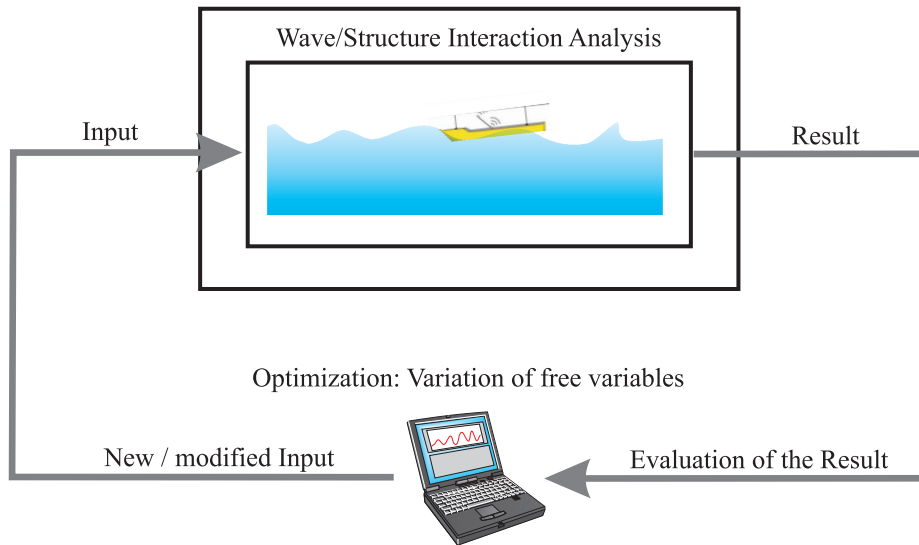


**Figure 5.3.:** General scheme of the new critical design wave concept. The fully automated procedure combines wave-structure interaction analysis programs with an optimization algorithm to find a most critical wave sequence.

## 5.2. Response-Based Identification Tool

So far, the problem of identifying and evaluating extreme responses has been exclusively employed to tailored extreme wave events being of general nature for wave-structure interaction investigations. Now, this problem is examined by a new response-based optimization procedure tailoring the response of an offshore structure (instead of the wave event) straightforward to a specific extreme value. At the end, this response-based identification tool reveals the underlying critical wave sequence leading to this extreme response value. This method enables the tailored identification of a wave sequence which causes a predefined most critical response for specific offshore structures.

Figure 5.3 presents the general scheme of the new design wave concept based on response-based optimization procedures. The general idea is to combine any wave-structure interaction analysis program with an optimization algorithm to find a most critical wave sequence with respect to predefined response levels. The core of the procedure is the selected program where the hydrodynamic problem is adequately analysed. In general, the procedure can be adapted to any hydrodynamic problem by selecting appropriate wave-structure interaction analysis tools. The level of non-linearity, to be reached, depends on the selected program as well as on the computational time available. The general functionality of the procedure as well as capability to find a global worst case wave sequence has successfully been shown by Clauss et al. (2010b, 2012b, 2013); Clauss and Klein (2013), from what revised parts are incorporated in the following.

At the beginning of the fully automated procedure the following parameters have to be defined:

- the input parameter(s) for the wave-structure interaction analysis program,
- the characteristic(s) to be considered during the optimization process,
- the target value(s) to be reached,
- the free variable(s) to be modified.

The input parameters are specified by the selected program, which also specifies the free variables. The free variables are part of the input and can be adjusted by the optimization algorithm to reach the predefined response level. The characteristics define the hydrodynamic problem to be investigated such as motion(s), global loads, local loads and so on. The target value, representing the limiting design value, defines the response level to be reached by the optimization algorithm. At each iteration step the result of the hydrodynamic calculation is evaluated regarding the target value to arrive at the worst response. Afterwards, the optimization algorithm modifies the free variables (target: worst combination) and restarts the wave-structure simulation. The optimization loop stops once the desired target value or the maximum number of iterations is reached.

The Subplex optimization method is utilized as local optimization algorithm (Rowan, 1990). This method is a generalization of the Nelder–Mead Simplex (NMS) method for unconstrained minimization. It can solve high dimensional problems by decomposing them into low dimensional subspaces. These low dimensional subspaces on the other hand can then easily be handled by NMS, preserving the advantage of NMS on noisy functions. In addition, the method is able to handle optimization constraints. Constraints are rejected as infeasible points by automatic restart which avoids a permanent collapse of the optimization.

The following sections present the application of the new concept on two typical design examples:

1. The maximum vertical bending moment a ship can experience in a certain sea state. The investigated limiting parameter is the vertical wave bending moment amidships.
2. An innovative offshore LNG transfer system consisting of a turret moored terminal barge and a shuttle carrier in tandem configuration. The investigated limiting parameter is the relative vertical motion of the coupling points of the transfer pipes between LNG carrier and barge.

### 5.2.1. Extreme Ship Response

Following, extreme ship responses to be considered in the design process are investigated. Objective of this investigation is to find a critical design wave sequence which leads to a maximum vertical wave bending moment a ship can experience in a certain sea state, as this is still a open question. In particular, due to the fact that the vertical bending moment shows a strong non-linear behaviour which cannot be covered by linear RAOs. For this purpose, the non-linear strip theory solver developed by IST (see Sec. 4.3) has been included into the optimization scheme to determine the non-linear ship response. Again, the chemical tanker investigated in Sec. 5.1 is used and the vertical wave bending moment at amidships is addressed. Thus, the results obtained are comparable to the impact of the breather-type freak waves determined in Sec. 5.1.

#### Response-Based Identification Tool

For the determination of maximum vertical wave bending moment the general scheme presented in Sec. 5.2 (cf. Fig. 5.3) has been adapted in such a way that a non-linear strip theory solver is combined with the Subplex optimization method.

The non-linear strip theory solver (see Sec. 4.3) has been chosen as *Wave-Structure Interaction Analysis Tool* in order to balance accuracy and computational time. In particular, the addressed response – the vertical wave bending moment – will show a strong non-linear behaviour in steep waves, which has to be considered for the investigation.

*Input* of the wave-structure interaction analysis tool is a sea state spectrum in terms of amplitudes and phase. Afterwards the associated surface elevation is transformed into time domain and the wave propagation is assumed to be linear. As initial *Input* a JONSWAP spectrum with an enhancement factor of  $\gamma = 3.3$  is chosen. The peak period of the investigated spectrum is identified from the linear vertical wave bending moment RAO.  $T_p = 10.5s$  is selected as this represents the wave length at the maximum magnitude of the RAO. The significant wave height is defined as  $H_s = 10m$  and the first phases are randomly distributed. Each wave spectrum realization is defined for a certain frequency bandwidth ( $\omega_s \leq \omega \leq \omega_e$ ) of relevant energy contributions, in order to reduce the number of individual waves (see Tab. 5.1 top). Figure 5.4 illustrates the *Input* (spectrum (top) and the associated phases (bottom)) used for this investigation. The simulation time is set to  $t = 100s$  to reduce the computational time needed for each iteration step. Table 5.1 (top) presents an overview of the applied sea state parameter.

The *Free Variables*, to be modified by the optimization procedure, are the phases of the input spectrum. Only the phases in the relevant bandwidth ( $\omega_1 \leq \omega \leq \omega_2$ ) of significant energy contributions are selected reducing the overall number of *Free Variables*  $n$  significantly. Figure 5.4 bottom illustrates the *Free Variables* used for

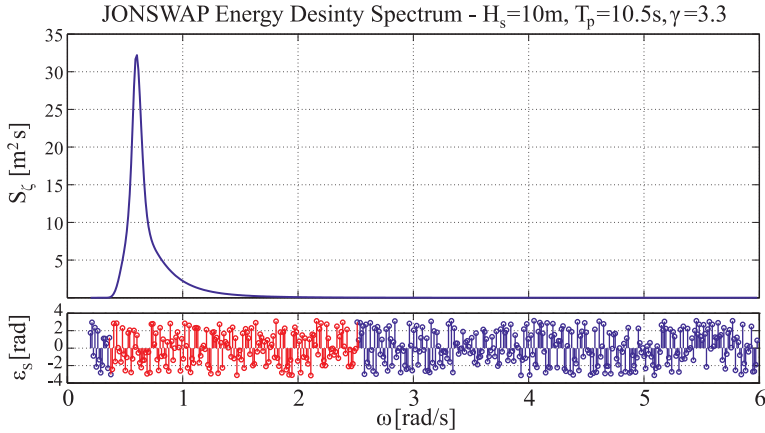


**Figure 5.4.:** Initial input: JONSWAP energy density spectrum (Clauss et al., 2012b).

the investigation (indicated in red). Table 5.1 (bottom) presents an overview of the applied optimization parameter and results.

The *Target Parameter* of the optimization is the vertical wave bending moment (worst response) of the chemical tanker in the chosen JONSWAP spectrum.

*Objective Function*, to be minimized by the Subplex optimization, reads

$$f = \left( \frac{\max|vbm(t)| - vbm_t}{vbm_t} \right)^2, \quad (5.1)$$

with  $\max|vbm(t)|$  being the maximum vertical wave bending moment of the actual realization. The target value  $vbm_t$ , to be reached by the optimization, is chosen in such a way that it marks an ultimate, exaggeratedly high value. For this purpose, the target value is set to  $vbm_t = 2.5 \cdot 10^6 kNm$  which is 2.5 times higher than the design vertical wave bending moment according the IACS Common Rules (GL, 2009). In addition to the above introduced target parameter and objective function, an inequality constraint regarding the maximum wave steepness is defined,

$$\begin{aligned} \left( \frac{\pi H}{L} \right)_{up} &\leq 0.4 \\ \left( \frac{\pi H}{L} \right)_{down} &\leq 0.4, \end{aligned} \quad (5.2)$$

due to the underlying simplified wave model. The theoretical wave height limit is  $\pi^H/L = 0.446$  (Miche, 1944), but  $\pi^H/L = 0.4$  represents a more realistic, empirical limit (Toffoli et al., 2010). Thus, the maximum allowable wave steepness is set according to Eq. 5.2, independently of zero up- or down-crossing analysis. This ensures that the optimized critical wave sequence displays a realistic shape which can be reproduced in the seakeeping basin.

In summary (cf. Fig. 5.3), the optimization starts with the initial wave spectrum using random phases. The response is calculated with the non-linear strip theory solver and the global loads as well as the wave sequence characteristics are

## 5. Extreme Responses

---

**Table 5.1.:** Overview of the parameter used for the optimization procedure.

name	sea state simulation parameter				
	$T_p$ [s]	$H_s$ [m]	$\gamma$	$\omega_s$ [rad/s]	$\omega_e$ [rad/s]
run 1	10.5	10	3.3	0.2	4
run 2	10.5	10	3.3	0.2	4
run 3	10.5	10	3.3	0.2	4.5
run 4	10.5	10	3.3	0.2	4
run 5	10.5	10	3.3	0.2	4
name	optimization parameter & results				
	$vbm_t$ [kNm]	$\omega_1$ [rad/s]	$\omega_2$ [rad/s]	n	max  vbm  [kNm]
run 1	$2.5 \cdot 10^6$	0.35	1.5	147	$1.648 \cdot 10^6$
run 2	$2.5 \cdot 10^6$	0.35	3	253	$1.638 \cdot 10^6$
run 3	$2.5 \cdot 10^6$	0.35	2.5	206	$1.569 \cdot 10^6$
run 4	$2.5 \cdot 10^6$	0.35	3	253	$1.75 \cdot 10^6$
run 5	$2.5 \cdot 10^6$	0.35	1.5	147	$1.732 \cdot 10^6$

evaluated by the Subplex algorithm (in terms of objective function and inequality constraints). Afterwards, the free variables (phases of the spectrum) are modified and the next iteration step starts. The optimization runs until either a threshold of the measure of merit ( $f \leq 10^{-3}$ ) or the maximum number of iteration steps (1200) is reached. Altogether five independent optimization runs have been performed.

Figure 5.5 illustrates the progress of the objective functions. A significant change of the residuals of the objective functions can be observed within the first 200 iteration steps showing that the Subplex algorithm quickly found an optimization strategy. After 300 iteration steps the five independent optimization runs reach an almost identical optimization level after what no significant changes can be observed. At the end, all runs result at the same response level and not one optimization reached the measure of merit. This indicates that the obtained critical wave sequences illustrate a global worst case for the defined sea state and wave steepness constraint.

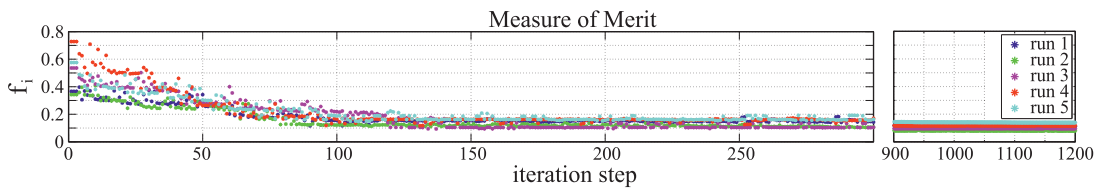


**Figure 5.5.:** Progress of the objective function.

The results of the optimization runs are presented in Fig. 5.6. The three top diagrams present the surface elevations at forward perpendicular, amidships and aft perpendicular. Afterwards, the heave and pitch motion is shown. The second diagram from bottom presents the relative surface elevation at forward perpendicular. The horizontal black dashed line represents the foredeck height above mean water level, i.e. values above denote green water on deck. The bottom diagram shows the corresponding vertical wave bending moment. The zero-downcrossing wave sequence leading to the worst response is indicated by the red rectangle and the time of maximum vertical wave bending moment is marked by the vertical black dashed line.

At first, the excellent agreement between the (maximum) vertical bending moment of each separate optimization run is remarkable. This indicates that the identified wave sequences are a global worst case for the defined input parameter. This is also reflected in the course of the critical wave sequence as well as motions.

As expected, the identified critical wave sequence is characterized by a deep wave trough neighbouring huge wave crests. The wave length almost equals the ship lengths – the classical sagging condition. The wave height of the critical wave expands to an extreme ( $H_{max}/H_s \approx 2$ ). However, the implemented maximum wave steepness limitation as well as green water on deck effects constrained the optimization in terms of encountering wave height and steepness. The effect of green water on deck results in a counteracting moment (Buchner, 1995), whereby the sagging loads are reduced or “cutted”. This effect can result in misinterpretation by the Subplex algorithm.

Figure 5.7 compares one selected optimized critical wave sequence (run 1) with its MLER/MLRW concept pendant. The target value for the vertical bending moment to be defined to calculate the MLER is chosen in such a way that the underlying MLRW results in a similar wave height compared to the critical wave sequence of run 1 focusing on the exact reproduction of the wave trough deepness. The top diagram presents the surface elevation at the main frame, whereas the bottom diagram shows the corresponding vertical bending moment. Comparing the optimization result with the classical MLER/MLRW concept reveals that critical wave sequences based on linear RAOs are significantly underestimating the vertical sagging bending moment (the hogging moments are even more overestimated), i.e. the vertical sagging bending moment is  $\approx 15\%$  higher for the non-linear simulations. It also means that the MLER/MLRW concept will lead to significant larger MLRW compared to the optimized critical wave sequences considering the same limiting response level. Optimization run 1 represents a best fit case, the other four cases feature a significantly larger discrepancy in terms of vertical sagging bending moment (up to  $\approx 30\%$ ). This proves that non-linear simulations are essential for the accurate determination of the worst case wave sequence in terms of vertical wave bending moment.

## 5. Extreme Responses

---

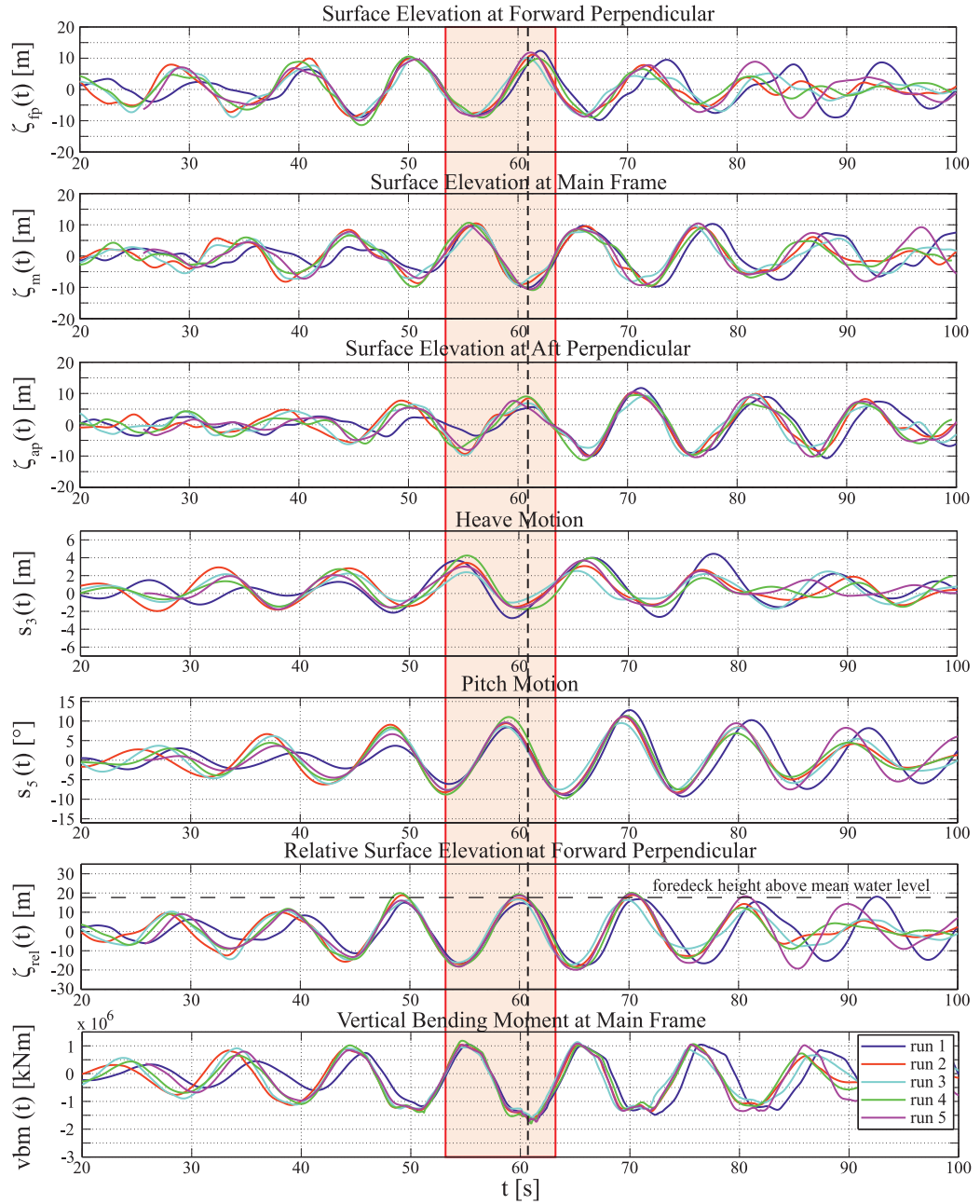


**Figure 5.6.:** Results of the optimization for the five independent realizations. The three top diagrams present the surface elevation at forward perpendicular, amidships and aft perpendicular. Afterwards, the heave and pitch motions are shown. The second diagram from bottom presents the relative surface elevation at forward perpendicular. The bottom diagram shows the corresponding vertical wave bending moment.

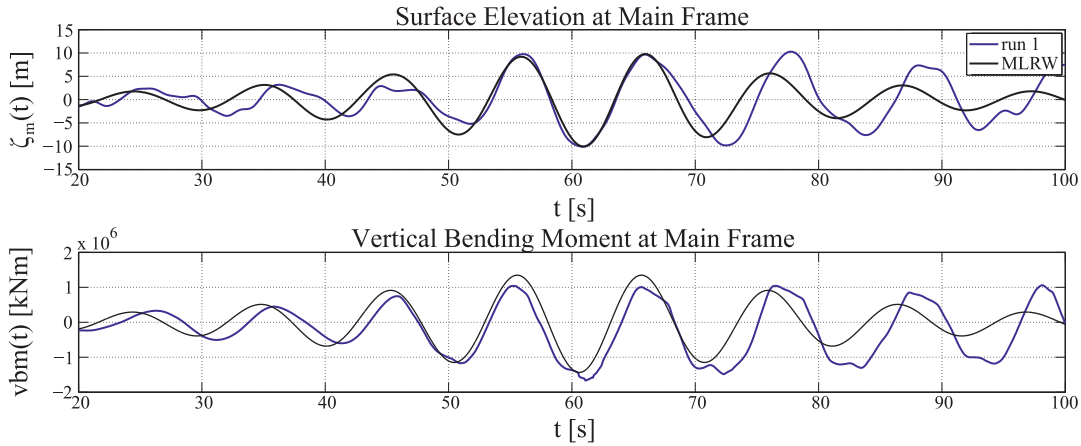


**Figure 5.7.:** Comparison between one optimized critical wave sequence and its classical MLER/MLRW concept pendant.

To prove the assumption that the identified wave sequences are worst case scenarios for the selected sea state, extensive numerical simulations are performed using the non-linear strip theory code. Thereby, 1000 random phase realizations of the above defined JONSWAP spectrum ( $H_s = 10m$ ,  $T_p = 10.5s$  and  $\gamma = 3.3$ ) are investigated, each represents an 800s registration.

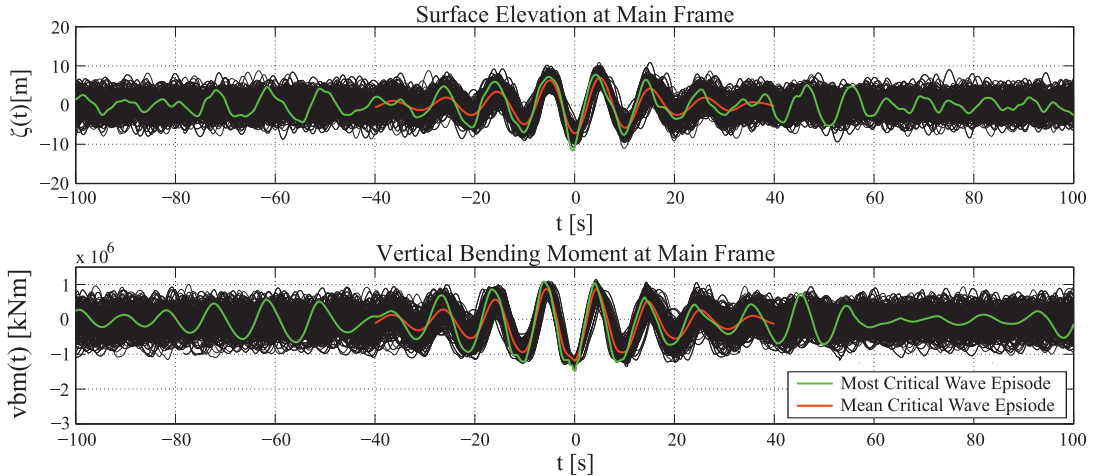
The simulations have been performed in order to evaluate the maximum vertical wave bending moment and its underlying wave sequence in relation to the optimized critical wave sequence. As a result, the quality of the optimization result can be reviewed. Therefore, the maximum vertical wave bending moment as well as the corresponding wave characteristics in terms of upcrossing wave period and wave height are determined for each simulation.

Figure 5.8 presents the critical wave sequences (similar to the linear CWE's concept) which lead to the highest vertical bending moment for each random phase realization. For clarity, only CWEs which result in loads larger than  $1.1 \cdot 10^6 kNm$  are shown. In addition, the inequality constraint regarding the maximum wave steepness (Eq. 5.2) is also applied for consistency reasons, i.e. steeper wave sequences are not considered. The red curve denotes the mean CWE and the green curve denotes the worst CWE of the non-linear simulations. The worst CWE reveals that the identified maximum vertical bending moment is  $\max|vbm_{RP}| \leq 1.48 \cdot 10^6 kNm$ , which is significantly smaller compared to the optimized critical wave sequences.

Analysing the individual results in detail, Fig. 5.9 presents the identified maximum vertical bending moments per simulation in relation to its corresponding wave period and wave height. The abscissa represents the upcrossing to peak period ratio and the ordinate the upcrossing to significant wave height ratio of the critical wave sequence which causes the maximum vertical bending moment – indicated by black crosses. For the evaluation of the maximum vertical bending moments,

## 5. Extreme Responses

---



**Figure 5.8.:** Results of the 1000 random phase realizations: The black curves represent the wave sequences of all realizations which lead to the highest vertical bending moment ( $vbm \geq 1.1 \cdot 10^6 kNm$ ). The top diagram shows the surface elevation and the bottom diagram the corresponding response. The red curve represents the mean CWE and the green curve the most critical CWE of the non-linear simulations.

values exceeding  $1.1 \cdot 10^6 kNm$  are illustrated in different colours as assigned in the colour bar below. The five optimization results are also illustrated and marked by red circles.

The diagram confirms the results obtained by the optimization runs – the critical wave length focuses around the peak period with tendency to slightly shorter waves. This denotes that also in the random phase simulations the critical wave length is close to the ship length between perpendicular. In addition, the results show an expected characteristic, the maximum vertical bending moment increases with increasing wave height. However, comparing the maximum vertical bending moment values from the random phase simulations ( $\max|vbm_{RP}| \leq 1.48 \cdot 10^6 kNm$ ) with the optimization results ( $\max|vbm_{NM}| \geq 1.57 \cdot 10^6 kNm$ ) reveals that the optimized critical wave sequences represent outstanding critical events. This proves that the optimization procedure is capable of the systematic search for critical wave sequences.

### Experimental Validation

The optimization results are validated in the seakeeping basin at Technische Universität Berlin. The test setup is identical with the one in Sec. 5.1. Figure A.3 shows the model test setup and Tab. A.2 the corresponding main dimensions. Details on the equipped model, the test setup and the suspension system can be found in Annex A.

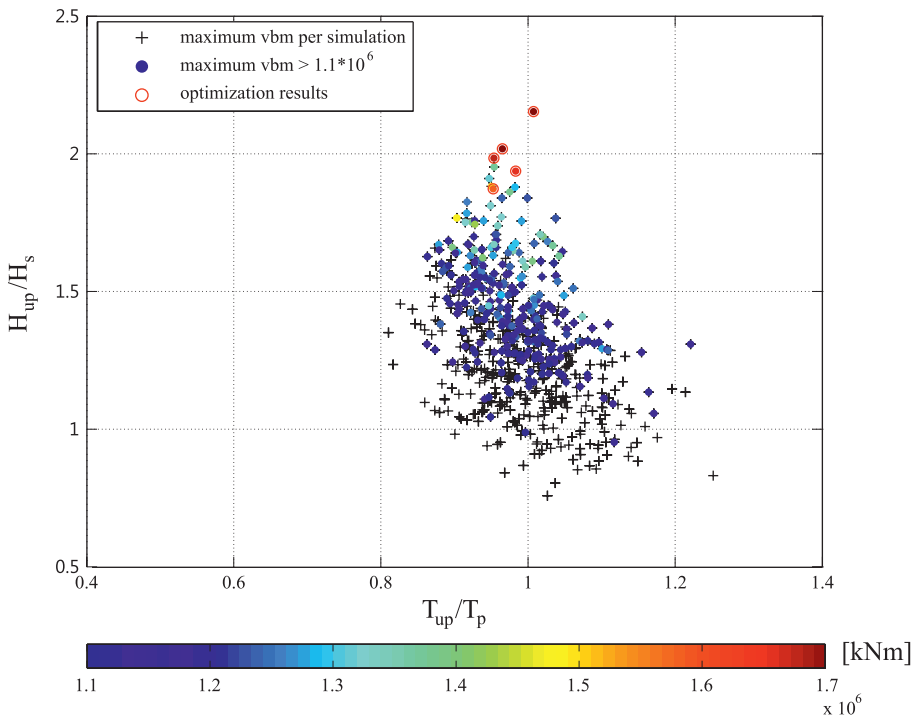


**Figure 5.9.:** Results of the 1000 random phase realizations compared to the optimization results (Clauss et al., 2012b).

The reproduction of such steep wave sequences in the seakeeping basin is a delicate issue as their propagation behaviour is characterized by strong non-linear wave-wave interactions. The almost symmetric shape in terms of crest/trough height ratio in combination with this extraordinarily high wave steepness ( $\pi H/L \approx 0.39$ ) is an almost infeasible task. As a consequence, the initial wave group at the wave board is exposed to non-linear effects during the propagation to the target location which may result in wave breaking (wave focussing effects), radiation and structural transformation. In particular, wave focussing effects of such steep wave groups (with small frequency bandwidth due to modulational instability) are the main problem depending on the propagation distance, i.e. target location. Consequently, the target location is set closer to the wave maker ( $x_t = 25m$ ) to avoid strong radiation as well as focussing effects of such steep wave group. For the reproduction of the critical wave sequences, the phase-amplitude iteration scheme is utilized (cf. Sec. 2.3.2). The fact that the five identified critical wave sequences are almost identical enabled the generation of one representative critical wave sequence in the seakeeping basin.

Figure 5.10 presents the results of the experimental validation. The top diagram compares the numerical surface elevations at the main frame with the reproduced surface elevation (black curve). The bottom diagram shows the corresponding vertical wave bending moment.

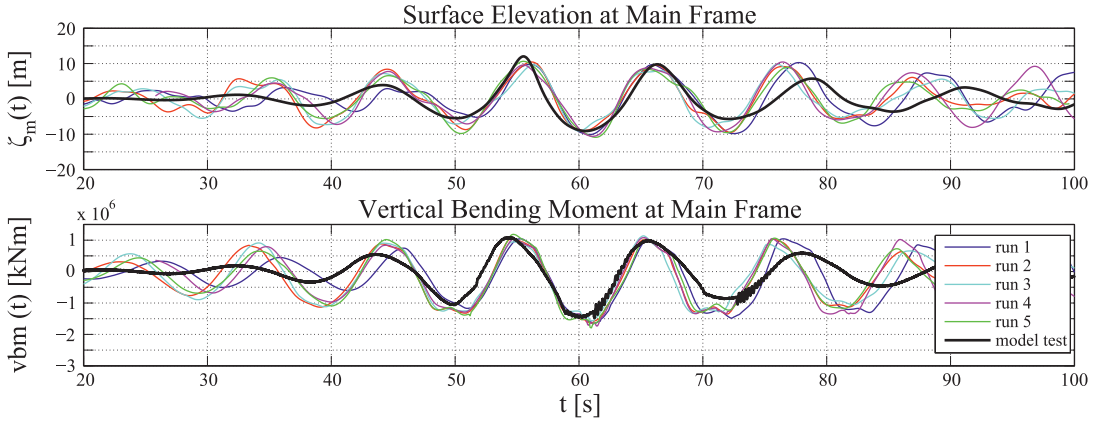


**Figure 5.10.:** Comparison of model test results and numerical simulations. The top diagram presents the surface elevation at the main frame of the chemical tanker and the bottom diagram the corresponding vertical wave bending moment.

The agreement between reproduced and numerical wave sequences is satisfactory. The differences arise from the fact that the identified numerical wave sequences are based on linear theory. Hence, in reality these very steep wave groups ( $\pi^H/L \approx 0.39$ ) show deviations with respect to crest/trough asymmetry. The reproduced wave formed an asymmetric shape in comparison to the numerical wave sequences – resulting in shorter, steeper wave crests and longer, shallower wave troughs.

The corresponding vertical bending moment features a similar agreement due to the difference between calculated and reproduced waves. In addition and in contrast to the numerical simulations, the surge motions are only restricted and not eliminated. However, the overall agreement is satisfactory, the measured large sagging loads are close to the predicted ones and confirm the numerical results. It shows that the impact of the identified wave sequence is severe and a limiting case for the investigated chemical tanker.

Comparing the identified extreme response with the results obtained in the breather-type freak waves in Sec. 5.1 reveals that the measured maximum vertical bending moment during the impact of the breather-type freak waves are also outstanding values. In particular, the two longer carrier periods reach almost the same level of maximum sagging values showing that the breather-type freak waves represent limiting cases for the vertical bending moment as well. However, this conclusion is only proved by the excellence of the new response-based identification tool in identifying global worst case critical wave sequences.

### 5.2.2. Multi-Body Offshore Operation

The functional principle of the response-based identification tool is introduced and verified with a chosen example of practical relevance. Now, a multi-body offshore

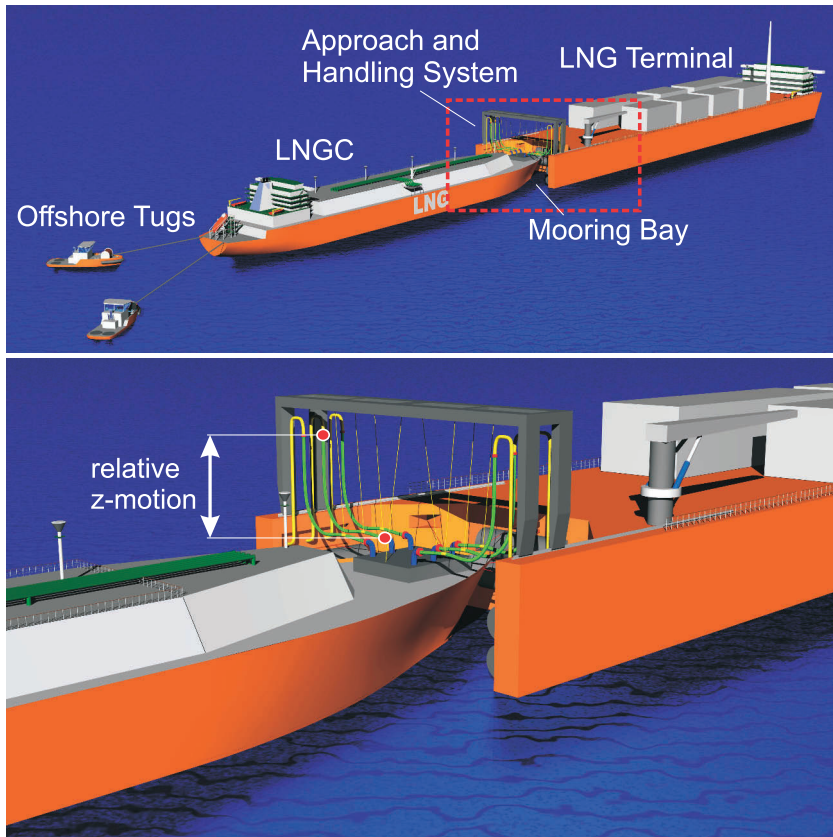


**Figure 5.11.:** The *MPLS20* concept: Illustration of the investigated tandem configuration of a turret moored terminal barge and a shuttle carrier. The top picture presents a general overview. The details of the transfer system in the red dashed rectangle of the top picture are additionally presented in the bottom picture indicating the connection points for the LNG transfer pipe.

operation in terms of LNG transfer between a turret moored terminal barge and a shuttle carrier is investigated to demonstrate the broad scope of application of the new method. The design concept proposes that both vessels operate in tandem configuration during transfer, being connected via flexible transfer pipes. This concept has been developed within the framework of the joint research project *MPLS20 – Maritime Pipe Loading System 20"* (Clauss et al., 2009; Hoog et al., 2009). Figure 5.11 provides a general overview of the LNG transfer concept.

Objective of the following investigation is an evaluation of the operability of the LNG transfer system. The limiting parameters for a safe unloading process (avoiding failure of the transfer pipe or collision) are the relative motions of the coupling points of the transfer pipes between the two vessels (see red dots in Fig. 5.11 bottom). Therefore, the target of the following investigations is the evaluation of the operational limit of the LNG transfer system in terms of operational range based on maximum tolerable relative motions. Table A.1 presents the main dimensions of the two vessels considered for the subsequent investigations. In addition, the cargo

tanks are assumed to be completely filled and the transfer distance between terminal stern and carrier bow is 10m. The site of operation chosen for this investigation is Haltenbanken in the Norwegian Sea and the long crested waves are approaching from  $\theta = 180^\circ$ . The maximum tolerable double amplitude of the vertical relative motion between the connection points is specified as  $(2s_{z,rel})_{tol} = 10m$ .

The investigations starts with a linear stochastic analysis to provide the basis for the subsequent application of the new critical design wave concept in terms of design sea state parameters. The results obtained by the new method are reviewed against classical methods – time domain investigations based on the realization of a multitude of different very long sea states (with random phases) similar to the CWE concept as well as conditioning of the phase distribution of the sea state by means of optimization procedure. At the end of the investigation all results are validated by model tests.

### Downtime Analysis

The annual downtime of the multi-body system is determined according to the method presented in Sec. 4.4.1. Starting point is the calculation of the response in terms of linear transfer functions. Therefore, WAMIT (see Sec. 4.2) has been applied to determine the RAOs for the hydrodynamically coupled multi-body problem in frequency domain. Afterwards, the characteristic RAOs for heave and pitch motion of the individual vessels are transformed to the connection points (red dots in Fig. 5.11) and combined to obtain the RAO of the relative vertical motion between these two connection points, which is the measure of merit of this investigation.

Figure 5.12 (top) presents the calculated RAO of the relative vertical motion of the connection points which is crucial for the bending behaviour of the pipes. The course of the RAO is characterised by several local maxima. These maxima, which are associated to the individual heave and pitch motions of both vessels, are primarily affected by the interaction of the individual pitch motions in amplitude and phase.

The determined RAO of the relative vertical motion of the connection points is the basis for the following downtime analysis. Applying Eqs. 4.9 and 4.10 yields the significant RAO for the relative vertical motion, which is shown in the bottom diagram in Fig. 5.12. The significant RAO is a function of the zero-upcrossing period of the surrounding sea state and specifies the significant response for arbitrary combinations of  $H_s$  and  $T_0$ . Based on the calculated significant RAO the tolerable significant wave heights  $H_{s,tol}(T_0)$  are determined (Eq. 4.13). Thereby, the corresponding tolerable significant vertical relative motion  $(2s_{z,rel})_{s,tol}$  is obtained by relating maximum to significant values (Eq. 4.11):  $(2s_{z,rel})_{max}/(2s_{z,rel})_{s,tol} = 1.86$  (most probable maximum) ... 2.0...2.3...2.4 results in  $(2s_{z,rel})_{s,tol} = 5.38m...5m...4.35m...4.17m$ , respectively.

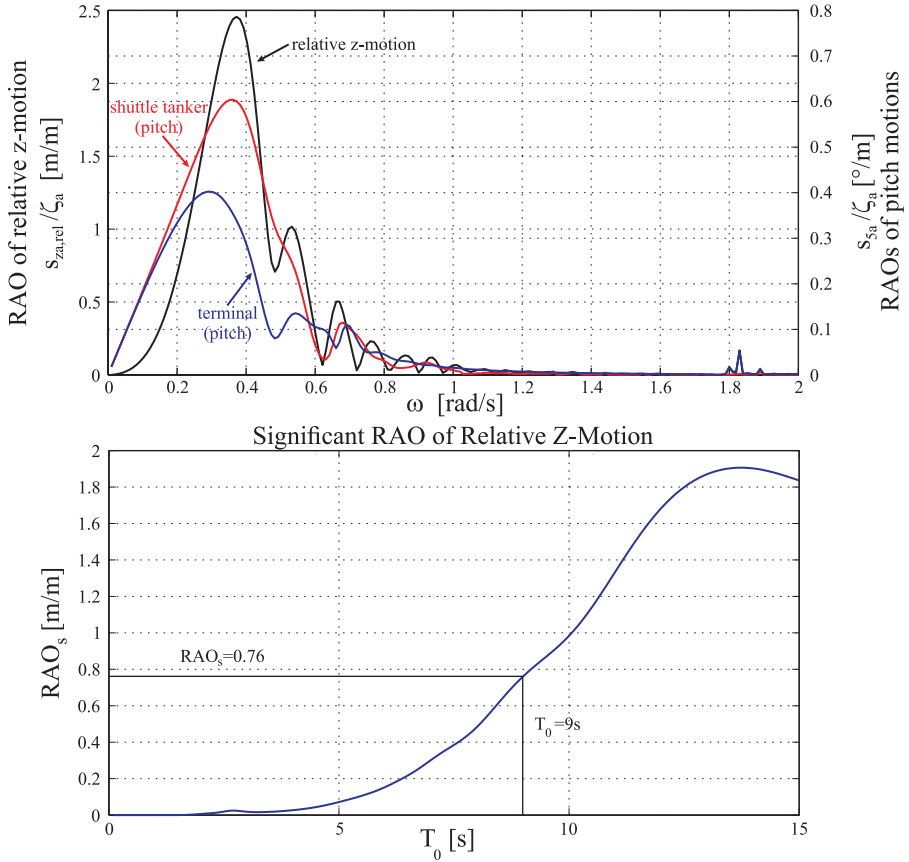


**Figure 5.12.:** The top diagram presents the RAO of the relative vertical motion between the two connection points (black curve) as well as the underlying individual pitch motion RAOs of the shuttle tanker (red curve) and the terminal barge (blue curve). The bottom diagram shows the significant RAO for the relative vertical motion between the connection points (Clauss and Klein, 2013).

Figure 5.13 presents the corresponding tolerable significant wave heights transferred into the scatter diagram for the location Haltenbanken. The unfeasible regions are indicated by the red area and the feasible sea states by the green area. For lower tolerable significant vertical relative motion  $(2s_{z,rel})_{s,tol}$  the unfeasible region increases (orange for  $(2s_{z,rel})_{max}/(2s_{z,rel})_{s,tol} = 2$ , yellow for  $(2s_{z,rel})_{max}/(2s_{z,rel})_{s,tol} = 2.3$  and blue for  $(2s_{z,rel})_{max}/(2s_{z,rel})_{s,tol} = 2.4$ ). The corresponding downtime results in 1.39% (5 days) for 1.86, 1.76% (6.5 days) for 2.0, 3.11% (11 days) for 2.3 and 3.56% (13 days) for 2.4 confirming that the maximum double amplitude values selected in the frequency domain analysis influences the operational range of the system directly. The suitable selection of this parameter is a delicate problem as it affects contrariwise safety and economy.

The scatter diagram enables a fast evaluation of a design from a statistical point of view. The next step is to conduct time domain investigations to identify the

## 5. Extreme Responses

---

		Zero-Upcrossing-Period [s]													Sum
		0-4	4-5	5-6	6-7	7-8	8-9	9-10	10-11	11-12	12-13	13-14	14-15		
significant wave height $H_s$ [m]	11,5-12,0	0	0	0	0	0	0	0,006	0	0	0	0	0	0,006	
	11,0-11,5	0	0	0	0	0	0	0	0,006	0	0	0	0	0,006	
	10,5-11,0	0	0	0	0	0	0	0	0,012	0	0	0	0	0,012	
	10,0-10,5	0	0	0	0	0	0	0	0,006	0	0	0	0	0,006	
	9,5-10,0	0	0	0	0	0	0	0,012	0,018	0,006	0	0	0	0,036	
	9,0-9,5	0	0	0	0	0	0	0,06	0,024	0,006	0	0	0	0,090	
	8,5-9,0	0	0	0	0	0	0	0,078	0,03	0	0	0	0	0,108	
	8,0-8,5	0	0	0	0	0	0	0,036	0,132	0,018	0	0	0	0,185	
	7,5-8,0	0	0	0	0	0	0	0,114	0,161	0,03	0	0	0	0,305	
	7,0-7,5	0	0	0	0	0,018	0,179	0,084	0,006	0	0	0	0	0,287	
	6,5-7,0	0	0	0	0	0,048	0,365	0,096	0,006	0	0	0	0	0,514	
	6,0-6,5	0	0	0	0	0,185	0,544	0,042	0,018	0	0	0	0	0,790	
	5,5-6,0	0	0	0	0	0,7	0,544	0,084	0,006	0	0	0	0	1,334	
	5,0-5,5	0	0	0	0,042	1,16	0,449	0,102	0	0	0	0	0	1,752	
	4,5-5,0	0	0	0	0,473	1,531	0,514	0,096	0,006	0	0	0	0	2,620	
	4,0-4,5	0	0	0,006	1,406	1,621	0,449	0,167	0,012	0	0	0	0	3,661	
	3,5-4,0	0	0	0,197	2,434	1,573	0,604	0,054	0	0	0	0	0	4,863	
	3,0-3,5	0	0	1,118	3,074	1,752	0,467	0,096	0	0	0	0	0	6,508	
	2,5-3,0	0	0,096	3,828	3,84	1,818	0,58	0,09	0,012	0	0	0	0	10,264	
	2,0-2,5	0	1,854	6,041	4,45	1,693	0,431	0,108	0,018	0	0	0	0	14,594	
	1,5-2,0	0,496	6,884	6,579	2,991	1,184	0,233	0,042	0	0	0	0	0	18,410	
	1,0-1,5	4,336	9,57	5,222	2,183	0,419	0,042	0,018	0	0	0	0	0	21,790	
	0,5-1,0	4,36	4,516	1,962	0,586	0,114	0,018	0	0	0	0	0	0	11,556	
	0,0-0,5	0,132	0,108	0,054	0,012	0	0	0	0	0	0	0	0	0,305	
Sum		9,325	23,028	25,007	21,491	13,817	5,419	1,376	0,478	0,060	0,000	0,000	0,000	100	

**Figure 5.13.:** Operational range for the multi-body offshore system at the location Haltenbanken (Norwegian Sea). The red area indicates the unfeasible sea states for  $(2s_{z,rel})_{max}/(2s_{z,rel})_{s,tol} = 1.86$ . The additional unfeasible regions for  $(2s_{z,rel})_{max}/(2s_{z,rel})_{s,tol} = 2$  are indicated in orange, for  $(2s_{z,rel})_{max}/(2s_{z,rel})_{s,tol} = 2.3$  in yellow and for  $(2s_{z,rel})_{max}/(2s_{z,rel})_{s,tol} = 2.4$  in blue (Clauss and Klein, 2013).

underlying critical wave sequences. For these investigations, the defined limiting operational significant wave height ( $H_s = 5.5m$ ) of the MPLS20 system is selected. From Fig. 5.13 follows that  $T_0 = 9s$  represents a sea state of interest (black circle in Fig. 5.13) for the following investigations due to the location at the boundary between feasible and unfeasible sea states.

### Critical Wave Episode

Figure 5.14 presents the results of the investigated sea state (JONSWAP:  $H_s = 5.5m$ ,  $T_0 = 9s$  and  $\gamma = 3.3$ ). The theoretical approach of the CWE concept is illustrated in the three top left diagrams. The top left diagram presents the investigated wave spectrum, the centre diagram the relative vertical motion RAO and the bottom diagram the respective response spectrum (cf. Eq. 4.8). The significant double amplitude of the relative vertical motion is  $(2s_{z,rel})_s = 4.18$ . To arrive at CWEs, the response spectrum is combined with 10000 random phase distributions and transformed into time domain resulting in 10000 different realizations. Afterwards, each realization is evaluated regarding the maximum response and maximum wave height. The results are illustrated in the three top right diagrams in Fig. 5.14. The top diagram presents the PDF of the 10000 individual maximum

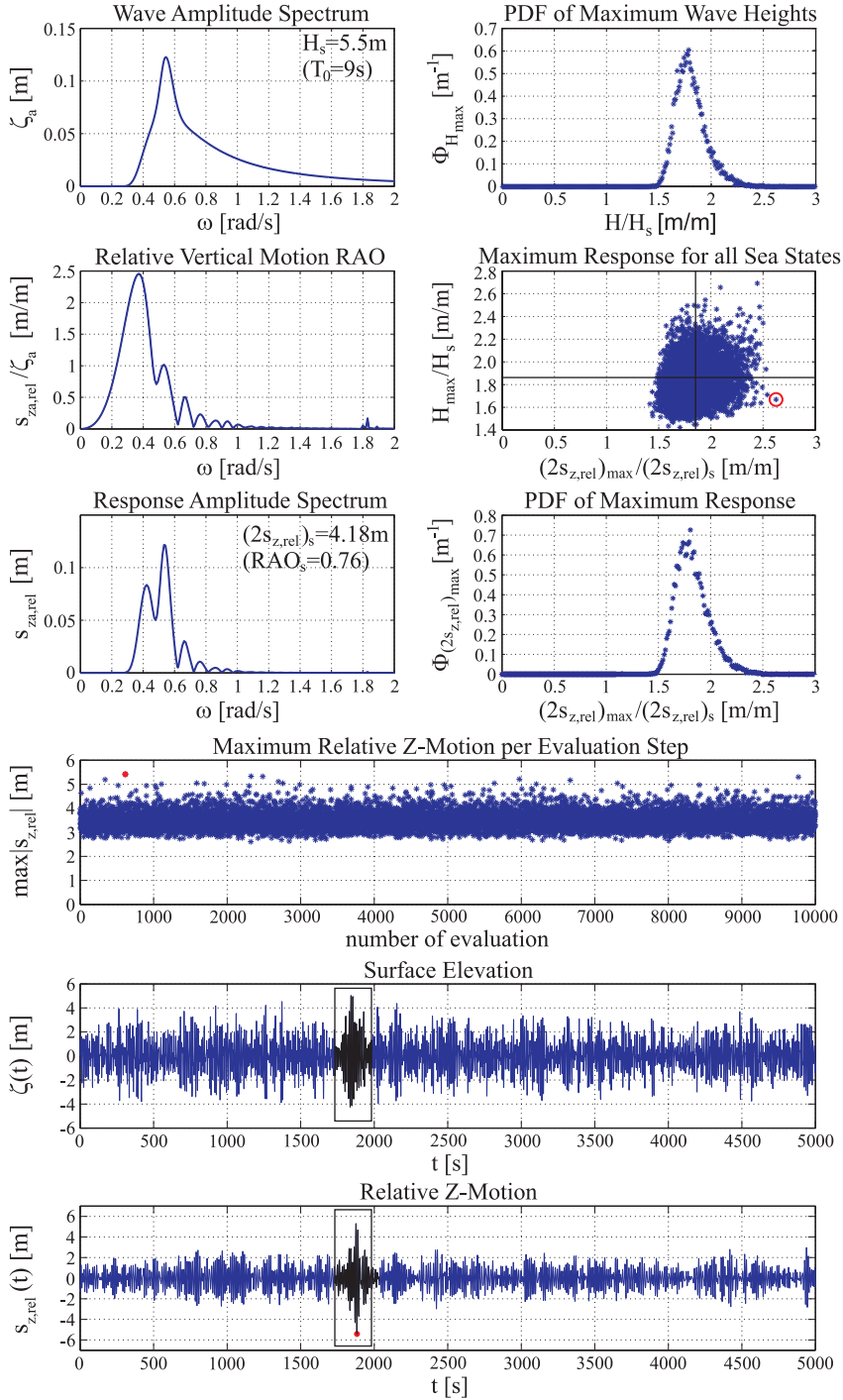


**Figure 5.14.:** Critical Wave Episode: The three top left diagrams present the general procedure. The three top right diagrams the PDF of maximum wave heights (top) and response (bottom) as well as the respective maximum wave height and response for each sea state realization (centre). The three bottom diagrams show the result of the random phase approach in detail: the maximum relative z-motion per evaluation step (top), the surface elevation of the worst wave sequence at the terminal mainframe (centre) and the associated relative z-motion at the connection points (bottom) (Clauss and Klein, 2013).

wave heights and the bottom diagram the PDF of the 10000 individual maximum relative vertical motion. The centre diagram compares the maximum to significant values for the response and wave height. This diagram illustrates that a great number of realizations (63%) exceeds the “most probable” limit of maximum to significant value of 1.86. In addition, it can be seen that the worst response (red encircled) is not associated with the maximum wave height.

The three bottom diagrams in Fig. 5.14 show the results in detail. The top diagram presents the maximum relative vertical motion per evaluation step. The worst response is indicated by the red dot. The most critical sea state realization at the terminal mainframe leading to this extraordinary response is illustrated in the centre diagram. The bottom diagram presents the associated response. The most critical wave episode is highlighted in black.

### Phase Distribution Optimization

So far, the multi-body system is analysed in frequency and time domain by random technique. Following, a procedure similar to the one presented by Alford (2008) is applied for comparison with the new method as it features the same basic idea: The sought-after critical wave sequence is determined by tailoring the encountering wave sequence by means of an optimization procedure.

In this case the phase distribution of the wave spectrum is manipulated in frequency domain to obtain the worst response. The response spectrum is determined via linear RAOs and subsequently transferred into time domain to evaluate the maximum response (of each realization). For this purpose the Subplex optimization method is utilized. The optimization algorithm manipulates the phases of the wave spectrum and evaluates the corresponding response based on target parameters. As aforementioned, the target is to find the maximum relative z-motion amplitude  $(s_{z,rel})_{max_{PD}}$  for the multi-body offshore operation. The objective function to be minimized reads

$$f = \left( \frac{(s_{z,rel})_{max_{PD}} - max|(s_{z,rel})(t)|}{(s_{z,rel})_{max_{PD}}} \right)^2, \quad (5.3)$$

with  $max|(s_{z,rel})(t)|$  as the maximum relative vertical motion of the actual realization. Based on the random phase approach result – see red dot in Fig. 5.14 (third from bottom) – this value is set to  $(s_{z,rel})_{max_{PD}} = 7m$ . To exclude that the optimization ends with the simplest solution (all component waves are in phase), which would result in non-physical wave heights, the most probable maximum wave height  $H_{max}/H_s \leq 1.86$  is defined as inequality constraint.

Figure 5.15 presents the results of the phase distribution optimization. The most critical sea state obtained by the previous random variation of phase distribution (Fig. 5.14 – second from bottom) has been used as starting point of the optimization (initial input sea state). The top diagram presents the objective function.

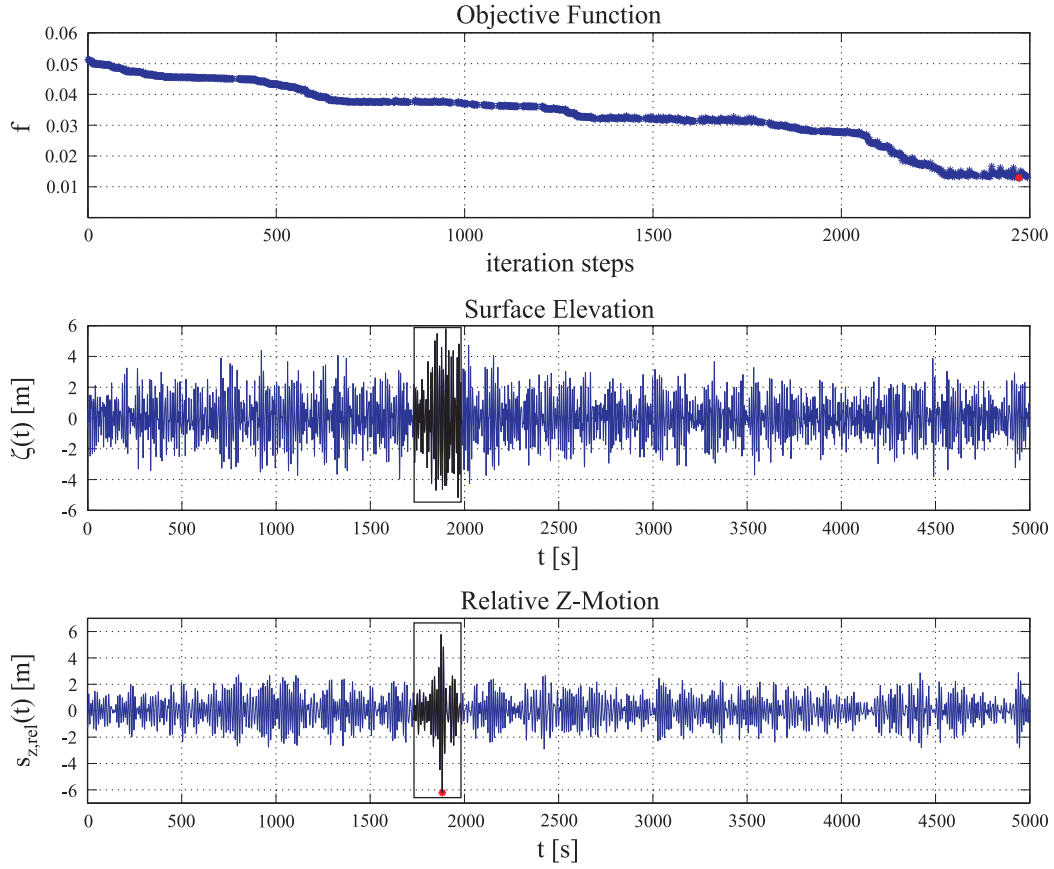


**Figure 5.15.:** Result of the phase distribution optimization. The top diagram presents the objective function, the centre diagram the (optimized) most critical wave sequence at the terminal mainframe (black highlighted) and the bottom diagram the corresponding worst response (Clauss et al., 2010b).

The exit value for the objective function has been set to  $f \leq 10^{-6}$  with a maximum number of 2500 iterations. The course of the objective function reveals that the optimization algorithm found an optimization strategy and improves the objective function until approximately 2250 iteration steps are reached. Afterwards, the objective function fluctuates around the optimum but does not reach the set threshold within the maximum number of iterations. The centre diagram presents the optimized sea state at the terminal mainframe. The critical wave sequence leading to the worst response is highlighted in black. The corresponding response is illustrated in the bottom diagram. The response due to the critical wave sequence is also highlighted in black. The maximum response is indicated by the red dot. The maximum relative vertical motion has been increased by  $\approx 15\%$  resulting in  $|(s_{z,rel})_{max_{PD}}| = 6.20m$  (compared to the random phase approach  $|(s_{z,rel})_{max_{RP}}| = 5.41m$ ).

### Response-Based Identification Tool

Now, the new design wave concept is adapted to this multi-body offshore system (cf. Fig. 5.3). The fundamental questions to be answered by this investigation are:

1. Is the new method able to detect similar extreme responses?
2. Are even more critical wave sequences (higher maximum response) possible within the selected sea state?

For the determination of the structure response a hybrid *Wave-Structure Interaction Analysis Tool* has been developed. The tool combines the non-linear wave tank WAVETUB (Sec. 2.5), for the accurate description of the waves, and the spectral approach for the determination of the corresponding multi-body response. The application of a non-linear numerical wave tank enables an accurate representation of the water waves in terms of wave propagation, steepening and shape of steep wave groups. In particular, the accurate representation of the shape of steep waves in terms of crest/trough asymmetry produces significantly more realistic results compared to the linear wave approach. In addition, non-physical waves with regard to wave steepness are not considered by WAVETUB and excluded from the sample space. Furthermore, the numerical wave tank can be adjusted to the geometry of the physical wave tank including the wave board enabling a fast transformation of the detected critical wave sequence to the physical wave tank for validation purposes. Altogether, applying a non-linear numerical wave tank for the encountering wave field represents an improvement compared to the classical methods. The second part of the *Wave-Structure Interaction Analysis Tool*, the calculation of the multi-body response is again based on the linear RAO approach introduced above (Eq. 4.8). The application of the linear approach for the determination of the response is an adequate compromise between accuracy and computational time as in head seas only heave and pitch motions contribute to the relative vertical motion. At each iteration step the wave sequence calculated by WAVETUB is transformed in frequency domain to determine the response spectrum. Afterwards, the response spectrum is transformed back in time domain to evaluate the result in terms of the objective function (maximization of the relative vertical motion) as well as inequality constraints.

*Input* for the wave-structure interaction analysis tool is the surface elevation at the wave board of the numerical wave tank. The surface elevation at the wave board is transformed into frequency domain (FFT), multiplied with the wave maker RAO and subsequently transformed back into time domain obtaining the wave board motion (see Sec. 2.3.2). The initial *Input* is the critical wave sequence detected by the random phase approach (see Fig. 5.14 second from bottom). For this investigation, only the short interval around the maximum response is used – the black highlighted curve in Fig. 5.14 second from top – to reduce the computational time per iteration step.

The wave board stroke is used as a *Free Variable*, i.e. it is optimized in order to modify the surface elevation at the wave board leading to a critical wave sequence in the course of propagation to the (virtual) location of the multi-body system. Therefore, the discrete wavelet transform (Daubechies, 1988) is introduced for the modification of the wave board stroke. In contrast to the phase optimization approach, where the phases of the spectrum are modified via FFT, affecting the whole time series, the discrete wavelet transform offers the punctual change of the wave board stroke in time domain. The discrete wavelet transform samples the signal into several decomposition levels and each coefficient describes the wave within a specific time range and frequency bandwidth. Consequently, the optimization algorithm can focus on a short part of the control signal changing the wave board stroke locally, close to the embedded critical wave group. For this investigation, the three scale wavelet transform is applied. To reduce the number of free variables (the wavelet coefficients), only the first two decomposition levels are modified.

The *Target Parameter* of the optimization is still the maximization of the relative vertical motion  $(s_{z,rel})_{max_{NM}}$  of the multi-body system for the given JONSWAP spectrum.

The *Objective Function* to be minimized reads

$$f = \left( \frac{(s_{z,rel})_{max_{NM}} - max|(s_{z,rel})(t)|}{(s_{z,rel})_{max_{NM}}} \right)^2, \quad (5.4)$$

with  $max|(s_{z,rel})(t)|$  as the maximum relative vertical motion of the actual realization. Again, based on the random phase approach result (Fig. 5.14 – bottom) as well as the phase optimization result (Fig. 5.15 – bottom) the target value is still set to  $(s_{z,rel})_{max_{PD}} = 7m$ . In addition to the above target parameter, the following inequality constraints are defined to ensure a smooth operation:

- most probable maximum wave height  $H_{max}/H_s \leq 1.86$ ;
- maximum wave board velocity;
- maximum wave board acceleration and
- termination condition due to instabilities of the numerical calculation (wave breaking).

Based on Fig. 5.3, the optimization starts with the calculation of the initial wave board motion, followed by the calculation of the encountering wave sequences as well as the respective response. The Subplex algorithm is used for the optimization, which evaluates the results at each iteration step in terms of objective function as well as inequality constraints. Afterwards, the free variables are modified before starting the next iteration step. Again, this procedure is repeated until either the measure of merit ( $f \leq 10^{-6}$ ) or the maximum number of iteration steps (2500) is reached.

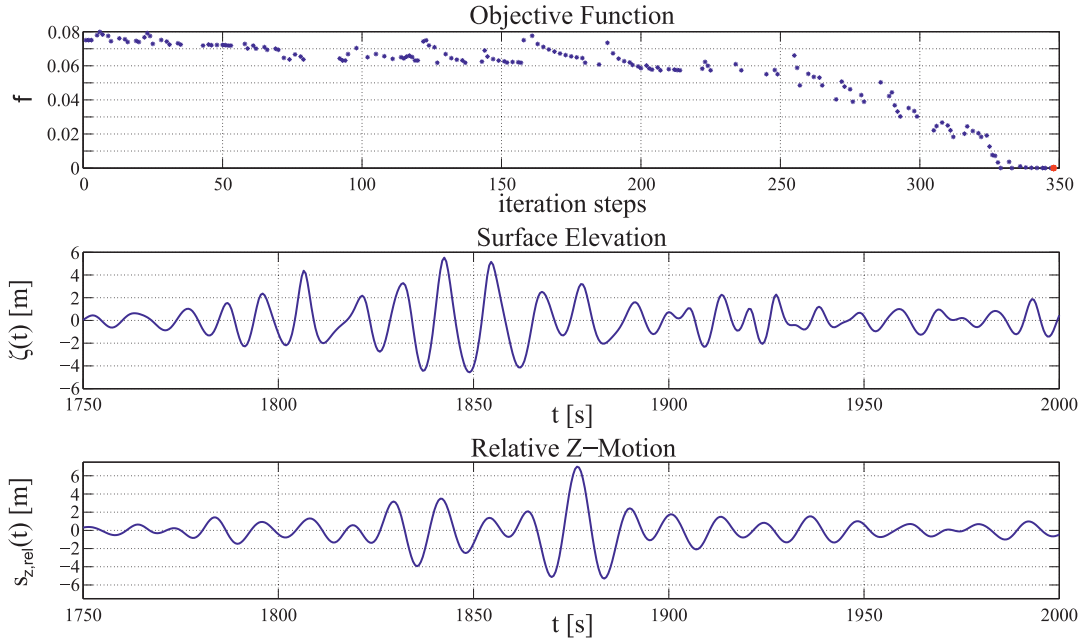


**Figure 5.16.**: Result of the response-based identification tool (Clauss et al., 2010b). The top diagram presents the course of the objective function, the centre diagram the (optimized) most critical wave sequence at the terminal mainframe and the bottom diagram the corresponding worst response.

Figure 5.16 illustrates the results of the new response-based identification tool. The top diagram presents the course of the objective function. The measure of merit decreases very fast and reaches the threshold ( $f \leq 10^{-6}$ ) after approximately 350 iteration steps. The gaps in the course of the objective function are associated with inequality constraints ( $f = 9$ ). The centre diagram presents the (optimized) worst critical wave sequence and the bottom diagram the corresponding response. The maximum relative vertical motion  $|(s_{z,rel})_{max_{NM}}| = 7m$  has been further increased compared to the phase optimization approach ( $|(s_{z,rel})_{max_{PD}}| = 6.2m$ ) and random phase approach ( $|(s_{z,rel})_{max_{RP}}| = 5.41m$ ). This shows that the new method not only found a similar extreme response level compared to classical methods, but also even significantly higher responses.

Next, the identified critical wave sequences obtained by the three different methods are compared to each other. Figure 5.17 presents the three identified wave groups leading to a maximum response (black encircled). All wave sequences show a similar trend – the dominating frequency of the three critical wave groups is  $\omega = 0.57rad/s$  which is related to the secondary peak in the relative vertical motion RAO in Fig. 5.12. A particular remarkable result is that marginal changes of the wave sequences obtained by the random phase approach (blue curve) cause significant changes of the response ( $\approx 30\%$ ) as the worst wave sequence obtained by the response-based identification tool (red curve) does not differ significantly.

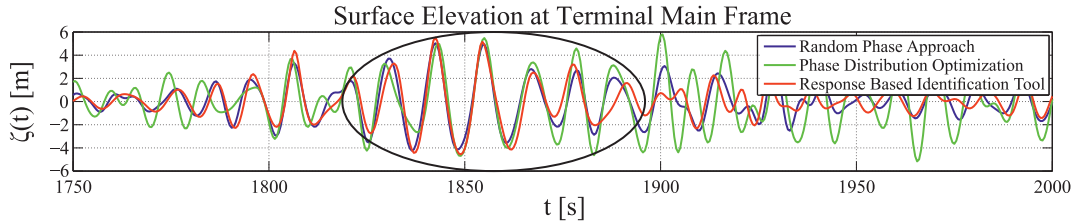


**Figure 5.17.:** Comparison of the three identified critical wave sequences. The wave groups leading the the maximum response are black encircled.

### Experimental Validation

So far, the three methods identified critical wave sequences leading to higher maximum relative vertical motions than predicted by the stochastic analysis. In particular, the worst critical wave sequence, which is identified with the new introduced method, exceeds the tolerable value by 23% within the “feasible” region in Fig. 5.13. As this alarming result follows from numerical analysis the identified critical wave sequences are reproduced in the wave tank to validate the results by model tests.

The experiments have been performed in the seakeeping basin at Technische Universität Berlin. Figure A.2 shows the model test setup – LNG carrier and terminal in tandem configuration where the carrier model is soft-moored. A detailed description of the seakeeping basin, the test setup and equipment can be found in Annex A.

For the reproduction of the waves, different procedures are available as summarized in Sec. 2.3.2. This case focuses on the fast reproduction of wave groups, hence, the phase-amplitude iteration scheme is utilized.

Figure 5.18 presents the model test results. The top black rectangle presents the results for the random phase approach, the centre black rectangle the results for the phase distribution optimization and the bottom black rectangle the results for the new response-based identification tool. Each block comprises two diagrams, the top diagram presents the surface elevation at the terminal mainframe and the bottom diagram the corresponding relative vertical motion. The theoretical results are illustrated in black and the model test results in red. The diagrams reveal that the overall agreement for the reproduction of the wave sequences as well as the respective response is excellent in phase and magnitude. The identified maximum relative vertical motions are confirmed for all three methods. It can be seen that for each case the model test even slightly exceeds the numerical maxima.

Altogether, it has been shown that the introduced response-based identification tool is generally applicable for systematic identification and evaluation of critical wave scenarios.

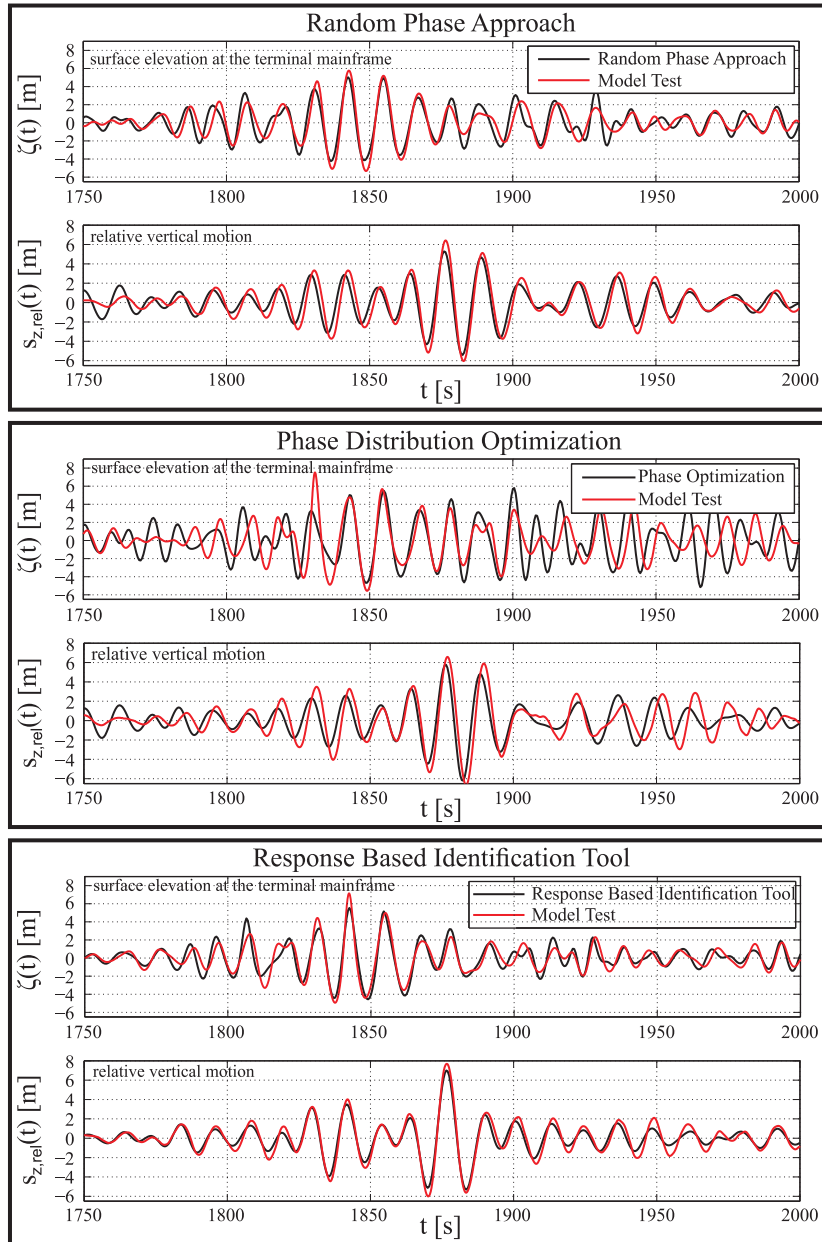


**Figure 5.18.:** Comparison between numerical calculations and measurements. The top black rectangle presents the results for the random phase approach, the centre black rectangle the results for the phase distribution optimization and the bottom black rectangle the results for the new response-based identification tool. Each block comprises two diagrams, the top diagram presents the surface elevation at the terminal mainframe and the bottom diagram the corresponding relative vertical motion. The theoretical results are illustrated in black and the model test results in red.

## 6. Conclusions

This thesis presents two innovative concepts in the field of tailoring critical wave sequences for response-based design:

- Analytical breather solutions of the NLS equation are applied as new experimental design freak waves;
- A response-based identification tool is introduced as new design wave concept.

The general applicability of breather solutions is addressed in Sec. 3. In this context the propagation, kinematics and dynamics of extreme wave events is investigated. Therefore, one real-world freak wave reproduction, namely the NYW, as well as the Kusnetzov-Ma breather are systematically investigated in the wave tank. The results obtained are compared in terms of wave propagation, kinematics and dynamics to conclude if breather solutions are a realistic representation of extreme wave events.

The experiments verify that the theoretical model of the breather solutions can be transferred into the wave tank, i.e. freak waves up to the maximum possible wave height have been generated. In addition, it has been shown that the modulation instability leads to extraordinarily large waves even in intermediate water depth ( $k_0 d > 1.36$ ) but influences the non-linear wave evolution significantly. In this context it has been shown that the fully non-linear numerical wave tank WAVETUB is applicable for accurate simulation as well as systematic investigation of such steep wave events which cannot be covered by weakly non-linear wave models. Weakly non-linear wave models such as NLS equation and its analytical breather solutions offers a fast qualitatively evaluation of non-linear wave propagation at the expense of accuracy (in particular for steeper wave sequences).

The breather-type freak waves show a very similar freak wave characteristic compared to the NYW. The potential span of application has been demonstrated by integrating a breather solution into an irregular sea state resulting in a freak wave within a random wave field. Altogether, this investigation revealed that the breather solutions are applicable for the deterministic generation of tailored extreme waves. Consequently, breather solutions are a efficient alternative for wave-structure investigations.

The application of breather solutions to model tests is presented in Sec. 5.1. For this purpose, a chemical tanker is investigated in three known breather solutions, namely the Kusnetzov-Ma breather, Akhmediev breather and Peregrine breather, as well as in the NYW. Evaluating the structure response reveals that the impact of the breather-type freak waves is severe resulting in outstanding extreme values for

## 6. Conclusions

---

the vertical wave bending moment. This is confirmed by the measured green water column heights at the forward perpendicular which also reaches impressive values. Comparing the structure response in the breather-type freak waves with the results obtained in the NYW demonstrated that the impact of the breather is significantly more dangerous. This result does not denote that real-world reproductions are useless for the evaluation of wave-structure interaction as they represent abnormal wave events which happened on sea, excluding any doubt regarding discussions on possible unrealistic, artificial wave sequences. Thus, real-world freak wave investigations are indispensable for a complete understanding of wave-structure interactions.

However, the investigations prove that the breather-type freak waves are experimental design waves to be considered for wave-structure investigations on different subjects, e.g. local and global loads, green water effects as well as air gap investigations. The major benefits are the potential to generate freak waves of certain frequency up to the physically possible wave height, the symmetrical shape of the freak wave and the availability of an analytical solution. Altogether, the breather solutions are an invaluable tool for the portfolio of test facilities dealing with wave-structure investigations in tailored critical wave sequences and should be established as standard procedure perspective.

The response-based identification tool is introduced as a new design wave concept in Sec. 5.2. The general applicability for finding global worst case wave sequences is shown for two typical design examples. The first application addresses extreme ship response to be considered in the design process: the critical parameter is the maximum vertical wave bending moment of a chemical tanker. The second application examines a multi-body offshore operation in terms of an innovative LNG transfer system: the relevant limiting parameter is the maximum relative vertical motion between a turret moored terminal barge and a shuttle carrier. In both cases, the implemented wave-structure interaction tools are chosen in such a way that the task is in balance between the need of sufficient accuracy, simple transformation to the physical wave tank and least amount of computational time.

The chemical tanker is investigated in terms of extreme ship response with the objective to identify a critical design wave sequence leading to a maximum vertical wave bending moment. The design sea state parameters are chosen from the linear vertical bending moment RAO, whereby the selected peak period represents the wave length of the maximum of the RAO. However, a non-linear strip theory solver has been introduced into the optimization scheme considering non-linear effects on the vertical wave bending moment. In addition, the maximum allowable wave steepness has been restricted to ensure that the optimized critical wave sequence displays a realistic shape. The critical wave sequences identified by the response-based identification tool result in the classical sagging condition – a deep wave trough surrounded by huge wave crests. The results are reviewed

---

against a multitude of random realizations of the design sea state, revealing that the optimized wave sequences are global worst cases. The optimized (worst case) maximum vertical wave bending moments are between 6% and 18% higher than the worst response of 1000 non-linear simulations of the design sea state with random phase realizations. Comparison with the classical MLER/MLRW concepts show that the adaption of the level of non-linearity is essential for the accurate description of the investigated wave-structure interaction problem.

For the multi-body offshore operation investigation the results obtained are reviewed against two classical design wave concepts. All three methods identify critical wave sequences within the feasible sea state resulting in higher motions than the tolerable value with regard to the linear stochastic analysis. It has been shown that the highest response must not be related to the highest wave. Contrariwise, the identified underlying wave sequences fulfil the (stochastic) most probable maximum wave height limit. This denotes that focussing on wave height only may not result in detecting the worst wave sequence.

Comparing the three different critical wave sequences reveal that the new response-based identification tool identifies the worst critical wave sequence resulting in 23% higher relative vertical motions (double amplitude) compared to the tolerable value. In addition, it is remarkable that marginal changes of the wave sequences can cause significant changes of the response. The worst wave sequence obtained by the response-based identification tool does not differ significantly from the CWE concept wave sequence but the response is  $\approx 30\%$  higher.

Altogether, the excellence and general applicability of the introduced response-based identification tool has been verified. The new response-based identification tool offers the systematic identification and evaluation of critical wave scenarios. Thereby, the level of non-linearity of the analysis can be adapted by selecting the appropriate tools inevitable for an accurate description of the investigated wave-structure problem. By means of this procedure, the identification and evaluation of critical design conditions can be conducted more systematically, accurately and efficiently.

Perspectively, the new tool is predestined for investigations of non-linear processes in terms of structure response. In particular, effects in steeper wave sequences which can not be covered by spectral analysis such as effects due to the existing hull structure above still water level as well as local effects. In particular, the alternate changing of the submerged part of the moving vessel causes significant changes of the response characteristics. This thesis demonstrates that the existing hull structure above still water level contributes significantly to the vertical bending moment which has to be taken into account. In this respect, a further prominent and dangerous aspect, which can be examined with the response-based identification tool, is the impact of waves on the stability of ships resulting in large (parametric) roll motions up to capsizing.

## *6. Conclusions*

---

Summing up, this thesis presented two innovative design wave concepts. All verifications show that both methods are not only suitable but also essential for the evaluation of offshore structures.

## Bibliography

- Adegeest, L. ., Braathen, A. ., and Vada, T. (2000). Evaluation of methods for estimation of extreme nonlinear ship responses based on numerical simulations and model tests. *Twenty-Second Symposium on Naval Hydrodynamics*, pages 84–99.
- Airy, G. (1845). Tides and Waves. *Encycl. Metrop.*, (Art. 192):241–396.
- Akhmediev, N., Ankiewicz, A., and Taki, M. (2009). Waves that appear from nowhere and disappear without a trace. *Physics Letters A*, 373(6), pages 675–678.
- Akhmediev, N., Eleonskii, V., and Kulagin, N. (1985). Generation of periodic trains of picosecond pulses in an optical fiber: exact solutions. *Sov. Phys. JETP*, 62(5), pages 894–899.
- Akhmediev, N., Eleonskii, V., and Kulagin, N. (1987). Exact first-order solutions of the nonlinear schrödinger equation. *Theoretical and Mathematical Physics*, 72(2), pages 809–818.
- Akhmediev, N. and Korneev, V. (1986). Modulation instability and periodic solutions of the nonlinear schrödinger equation. *Theoretical and Mathematical Physics*, 69(2), pages 1089–1093.
- Alford, L. K. (2008). *Estimating Extreme Responses using a Non-uniform Phase Distribution*. PhD thesis, The University of Michigan.
- Andonowati, Karjanto, N., and van Groesen, E. (2006). Extreme wave phenomena in down-stream running modulated waves. *Applied Mathematical Modelling*, 31(7):1425–1443.
- Benjamin, T. and Feir, J. (1967). The disintegration of wave trains on deep water. *Journal of Fluid Mechanics*, Vol. 27(3), pages 417–430.
- Bertotti, L. and Cavalieri, L. (2008). Analysis of the Voyager storm. *Ocean Engineering*, Vol. 35(1), pages 1 – 5.
- Biésel, F. and Suquet, F. (1951). Les appareils génératrices de houle en laboratoire. *La Houille Blanche*, (2):147–165.
- Boccotti, P. (2000). *Wave Mechanics for Ocean Engineering*, volume 64. Elsevier Oceanography Series.

## Bibliography

---

- Buchner, B. (1995). On the Impact of Green Water Loading on Ship and Offshore Unit Design. In *PRADS95 - 6th Symposium on Practical Design of Ships and Mobile Units*, Seoul, Korea.
- Buchner, B., van Dijk, R., and Voogt, A. (2007). The Spatial Analysis of an Extreme Wave in a Model Basin. In *OMAE 2007-26th International Conference on Offshore Mechanics and Arctic Engineering*, San Diego, USA. OMAE2007-29409.
- Cartwright, D. and Longuet-Higgins, M. (1956). The Statistical Distribution of the Maxima of a Random Function. In *Proc. Royal Society*, pages p.212–232. A237 (1209).
- Chabchoub, A., Hoffmann, N., and Akhmediev, N. (2011). Rogue wave observation in a water wave tank. *Physical Review Letters*, 106(20).
- Chabchoub, A., Hoffmann, N., Onorato, M., and Akhmediev, N. (2012). Super rogue waves: Observation of a higher-order breather in water waves. *Phys. Rev. X*, 2:011015.
- Chakrabarti, S. K. . (1971). Discussion on "Dynamics of single point mooring in deep water". In *Journal of Waterways, Harbour and Coastal Engr. Divison, ASCE*, pages 588–590, ASCE 1971, 97 (WW3).
- Chakrabarti, S. K. (1987). *Hydrodynamics of Offshore Structures*. Springer-Verlag. ISBN 3-540-17319-6.
- Chaplin, J. R. (1996). On Frequency-Focusing Unidirectional Waves. *International Journal of Offshore and Polar Engineering*, 6(2), pages 131–137.
- Cherneva, Z. and Guedes-Soares, C. (2008). Non-linearity and non-stationarity of the new year abnormal wave. *Applied Ocean Research*, Vol. 30, (3):215 – 220.
- Clauss, G. (2001). Synthesis of Deterministic Rogue Waves in Extreme Seas. In *RINA Design and Operation for Abnormal Conditions II*, London.
- Clauss, G. and Klein, M. (2009). The New Year Wave: Spatial Evolution of an Extreme Sea State. *JOMAE 2009 - Journal of Offshore Mechanics and Arctic Engineering*, 131(4).
- Clauss, G. and Klein, M. (2011). The new year wave in a seakeeping basin: Generation, propagation, kinematics and dynamics. *Ocean Engineering*, 38(14–15):1624 – 1639.
- Clauss, G. and Klein, M. (2013). How safe is 'safe'? Ship dynamics in critical sea states. *Ocean Engineering*, 72:87–97.
- Clauss, G., Klein, M., and Dudek, M. (2010a). Influence of the Bow Shape on Loads in High and Steep Waves. In *OMAE 2010 - 29<sup>th</sup> International Conference on Offshore Mechanics and Arctic Engineeringn*, Shanghai, China.

- Clauss, G., Klein, M., Guedes Soares, C., and Fonseca, N. (2013). Response based Identification of Critical Wave Scenarios. *JOMAE 2013 - Journal of Offshore Mechanics and Arctic Engineering*, 135.
- Clauss, G., Klein, M., Sprenger, F., and Testa, D. (2010b). Evaluation of Critical Conditions in Offshore Vessel Operation by Response Based Optimization Procedures. In *OMAE 2010 - 29th International Conference on Offshore Mechanics and Arctic Engineering*, Shanghai, China. ASME. OMAE2010-21071.
- Clauss, G. and Kühnlein, W. (1995). Seakeeping tests in transient wave packets. *Discussion on the Report of Seakeeping Committee — 21<sup>st</sup> International Towing Tank Conference*.
- Clauss, G. and Kühnlein, W. (1997). A new tool for seakeeping tests – nonlinear transient wave packets. In *Proceedings of the 8<sup>th</sup> Int. Conference on the Behaviour of Offshore Structures (BOSS)*, pages 269–285, Delft, The Netherlands.
- Clauss, G., Lehmann, E., and Östergaard, C. (1992). *Offshore Structures*, volume 1: Conceptual Design and Hydrodynamics. Springer Verlag London.
- Clauss, G., Sprenger, F., Testa, D., Hoog, S., and Huhn, R. (2009). Motion Behaviour of a New Offshore LNG Transfer System at Harsh Operational Conditions. In *OMAE 2009 - 28th Conference on Ocean, Offshore and Arctic Engineering*, Honolulu, USA.
- Clauss, G., Stempinski, F., and Klein, M. (2007). Experimental and Numerical Analysis of Steep Wave Groups. In *IMAM 2007 - 12<sup>th</sup> Congress of Intl. Maritime Assoc. of Mediterranean*, Varna, Bulgaria.
- Clauss, G. F. (2008). The Taming of the Shrew: Tailoring Freak Wave Sequences for Seakeeping Tests. In *Journal of Ship Research*, Vol. 52, Nr. 3, pages 194–226, [www.naoe.tu-berlin.de/MT](http://www.naoe.tu-berlin.de/MT).
- Clauss, G. F., Klein, M., Dudek, M., and Onorato, M. (2012a). Application of Breather Solutions for the Investigation of Wave/Structure Interaction in High Steep Waves. In *OMAE 2012 - 31th International Conference on Ocean, Offshore and Arctic Engineering*, Rio de Janeiro, Brazil. OMAE2012-83244.
- Clauss, G. F., Klein, M., Guedes Soares, C., and Fonseca, N. (2012b). Response based identification of critical wave scenarios. In *OMAE 2012 - 31<sup>st</sup> International Conference on Ocean, Offshore and Arctic Engineering*, Rio de Janeiro, Brazil. OMAE2012-83861.
- Clauss, G. F., Klein, M., and Onorato, M. (2011). Formation of Extraordinarily High Waves in Space and Time. In *OMAE 2011 - 30th International Conference on Ocean, Offshore and Arctic Engineering*, Rotterdam, The Netherlands. OMAE2011-49545.

## Bibliography

---

- Clauss, G. F. and Schmittner, C. E. (2005). Experimental Optimization of Extreme Wave Sequences for the Deterministic Analysis of Wave/Structure Interaction. In *OMAE 2005 - 24th International Conference on Offshore Mechanics and Arctic Engineering*, Halkidiki, Greece. OMAE2005-67049.
- Clauss, G. F., Schmittner, C. E., Hennig, J., Guedes Soares, C., Fonseca, N., and Pascoal, R. (2004). Bending Moments of an FPSO in Rogue Waves. In *OMAE 2004 - 23rd International Conference on Offshore Mechanics and Arctic Engineering*, Vancouver, Canada. OMAE2004-51504.
- Clauss, G. F., Schmittner, C. E., and Klein, M. (2006). Generation of Rogue Waves with Predefined Steepness. In *OMAE 2006-25th International Conference on Offshore Mechanics and Arctic Engineering*, Hamburg, Germany. OMAE2006-92272.
- Cooley, J. and Tukey, J. (1965). An Algorithm for the Machine Calculation of Complex Fourier Series. *Mathematics of Computation*, Vol. 19:297.
- Craik, A. D. (2004). The Origins of Water Wave Theory. *Annual Review of Fluid Mechanics*, 36(1):1–28.
- Cummins, W. (1962). The Impulse Response Function and Ship Motions. *Schiffstechnik*, Band 9(Heft 47):101–109.
- Daubechies, I. (1988). Orthonormal bases of compactly supported wavelets. *Communications on Pure and Applied Mathematics*, 41:909–996.
- Dietz, J. S. (2004). *Application of Conditional Waves as Critical Wave Episodes for Extreme Loads on Marine Structure*. PhD thesis, Technical University of Denmark, Department of Mechanical Engineering.
- Drummen, I. ., Wu, M. ., and Moan, T. (2009). Numerical and experimental investigations into the application of response conditioned waves for long-term nonlinear analyses. *Marine Structures*, 22:576–593.
- Dysthe, K. B. and Trulsen, K. (1999). Note on breather type solutions of the nls as models for freak-waves. *Physica Scripta*, T82, pages 48–52.
- Faulkner, D. (2000). Rogue Waves – Defining their Characteristics for Marine Design. In *Rogue Waves 2000*, Brest, France.
- Ferziger, J. H. and Peric, M. (2002). *Computational Methods for Fluid Dynamics*. Springer-Verlag, 3<sup>rd</sup> edition. ISBN 3-540-42074-6.
- Fonseca, N. . and Guedes Soares, C. (1998a). Time-Domain Analysis of Large-Amplitude Vertical Motions and Wave Loads. *Journal of Ship Research*, 42(2):100–113.
- Fonseca, N. and Guedes Soares, C. (1998b). Nonlinear Wave Induced Responses of Ships in Irregular Seas. *Proceedings 17<sup>th</sup> International Conference on Offshore Mechanics and Arctic Engineering (OMAE 98)*, New York.

- Fonseca, N. and Guedes Soares, C. (2002). Comparison of numerical and experimental results of nonlinear wave-induced vertical ship motions and loads. In *Journal of Marine Science and Technology*, pages 193–204.
- Fonseca, N., Guedes Soares, C., and Pascoal, R. (2006). Ship Structural Loads Induced by Abnormal Wave Conditions on a Containership. In *Journal of Marine Science and Technology*, Vol. 11, pages 245–259.
- Fonseca, N., Pascoal, R., and Guedes Soares, C. (2008). Global Structural Loads Induced by Abnormal Waves and Design Storms on a FPSO. In *Journal of Offshore Mechanics and Arctic Engineering*, Vol. 130, Iss. 2, page pp. 9.
- Friis-Hansen, P. . and Nielsen, L. P. . (1995). On the new wave model for the kinematics of large ocean waves. In *OMAE 1995 - 14th International Conference on Offshore Mechanics and Arctic Engineering*, Copenhagen, Denmark.
- Gardner, C. S., Greene, J. M., Kruskal, M. D., and Miura, R. M. (1967). Method for solving the Korteweg-deVries equation. *Phys. Rev. Lett.*, 19:1095–1097.
- GL (2009). Germanischer Lloyd. In *Rules & Guidelines*, Hamburg, Germany.
- Gonzales Sanches, S., Gonzales Prelic, N., and Garcia Galan, S. (1996). Uvi-Wave, Wavelet Toolbox for use with Matlab, Departamento de Tecnoloxias das Communicacions, Universidade de Vigo, 2nd edition. Technical report.
- Gorf, P., Barltrop, N., Okan, B., Hodgson, T., and Rainey, R. (2000). FPSO Bow Damage in Steep Waves. In *Rogue Waves 2000*, Brest, France.
- Gudmestad, O. T. und Connor, J. J. (1986). Engineering approximations to nonlinear deepwater waves. *Applied Ocean Research*, 8(2).
- Guedes Soares, C., Cherneva, Z., and Antão, E. M. (2004a). Abnormal Waves during the Hurricane Camille. *Journal of Geophysical Research*.
- Guedes Soares, C., Cherneva, Z., and Antão, E. M. (2004b). Characteristics of Abnormal Waves in North Sea Storm Sea States. *Applied Ocean Research*.
- Hasimoto, H. and Ono, H. (1972). Nonlinear modulation of gravity waves. *Journal of Physical Society of Japan*, Vol. 33, pages 805–811.
- Haver, S. and Anderson, O. J. (2000). Freak Waves: Rare Realization of a Typical Population or Typical Realization of a Rare Population? In *Proceedings of the 10th International Offshore and Polar Engineering Conference (ISOPE)*, pages 123–130, Seattle, USA.
- Henderson, K. L., Peregrine, D. H., and Dold, J. W. (1999). Unsteady water wave modulations: Fully nonlinear solutions and comparison with the nonlinear schrödinger equation.
- Hennig, J. (2005). Generation and Analysis of Harsh Wave Environments. *Dissertation*, Technische Universität Berlin (D 83).

## Bibliography

---

- Hoog, S., Koch, H., Huhn, R., Frohne, C., Homann, J., Clauss, G., Sprenger, F., and Testa, D. (2009). LNG Transfer in Harsh Environments — Introduction of a New Concept. In *Offshore Technology Conference*, Houston, Texas, USA. OTC 19866.
- Huijsmans, R. H. M., Klopman, G., Karjanto, N., and Andonowati (2005). Experiments on extreme wave generation using the Soliton on Finite Background. In Olagnon, M. and Prevosto, M., editors, *Rogue Waves 2004*, Ifremer, Brest, France.
- Jacobsen, K. (2005). Hydrodynamisch gekoppelte mehrkörpersysteme im seegang – bewegungssimulationen im frequenz- und zeitbereich. *Dissertation*, Technische Universität Berlin (D 83).
- Janssen, P. (2003). Nonlinear four-wave interactions and freak waves. *Journal of Physical Oceanography*, Vol. 33, pages 863–884.
- Johnson, R. S. (1997). *A Modern Introduction to the Mathematical Theory of Water Waves*. Cambridge texts in applied mathematics. Cambridge University Press. ISBN 0 521 591724.
- Journée, J. M. J. and Massie, W. W. (August 2000). *Offshore Hydromechanics*. Delt University of Technology.
- Karjanto, N. (2006). *Mathematical Aspects of Extreme Water Waves*. PhD thesis, University of Twente.
- Karjanto, N. and van Groesen, E. (2007). Derivation of the NLS Breather Solutions using Displaced Phase-Amplitude Variables. In *Proceedings of SEAMS-GMU Conference*.
- Karunakaran, D., Baerheim, M., and Leira, B. J. (1997). Measured and simulated dynamic response of a jacket platform. In *Proceedings of the 16th International Conference on Offshore Mechanics and Arctic Engineering*, Vol. II, pages 157–164.
- Kharif, C., Pelinovsky, E., and Slunyaev, A. (2009). *Rogue Waves in the Ocean*. Springer-Verlag Berlin Heidelberg.
- Kinsman, B. (1965). *Wind Waves*. Prentice Hall Inc., Englewood Cliffs, New York.
- Kjeldsen, S. P. (1990). Breaking Waves. In Tørum, A. and Gudmestad, O., editors, *Proceedings of the NATO Advanced Research Workshop on Water Wave Kinematics*, pages 453–473, Molde, Norway. Kluwer Academic Publishers, Dordrecht. NATO ASI Series, Series E - Volume 178.
- Kurkin, A. and Pelinovsky, E. (2004). Freak waves: Facts, theory and modeling. In *Techn Univ Printing House, in Russian*, page 158.
- Kuznetsov, E. (1977). Solitons in a parametrically unstable plasma. In *Akademiia Nauk SSSR Doklady*, Vol. 236, pages 575–577.

- Lee, C. (1995). WAMIT Theory Manual. Technical report, Massachusetts Institute of Technology. Preliminary Copy.
- Lemire, J. (2005). Freak wave rocks cruise. <http://www.cbmu.com/news.php?articleID=228>.
- Lewis, E., editor (1989). *Principles of Naval Architecture*, volume III – Motions in Waves and Controllability. The Society of Naval Architects and Marine Engineers, Jersey City, NJ, 2<sup>nd</sup> edition.
- Longuet-Higgins, M. (1975). On the Statistical Distribution of the Periods and Amplitudes in Sea Waves. *Journal of Geophysical Research*, 80:2688–2694.
- Ma, Y. (1979). The perturbed plane-wave solutions of the cubic schrödinger equation. *Studies in Applied Mathematics*, 60, pages 43–58.
- Mansard, E. P. D. and Funke, E. R. (1988). On the fitting of parametric models to measured wave spectra. *Procs. of 2<sup>nd</sup> International Symposium on Wave Research and Coastal Engineering, Hannover, Germany*, SFB 205, Universität Hannover:363–383.
- Osborne, A. R., Onorato, M., and Serio, M. (2000). The nonlinear dynamics of rogue waves and holes in deep-water gravity wave trains. *Physics Letters A*, Vol. 275, pages 386–393.
- Schmittner, C., Kosleck, S., and Hennig, J. (2009). A Phase-Amplitude Iteration Scheme for the Optimization of Deterministic Wave Sequences. In *OMAE 2009 - 28th International Conference on Ocean, Offshore and Arctic Engineering*, Honolulu, Hawaii. OMAE2009-80131.
- Schmittner, C. E. (2005). Rogue Wave Impact on Marine Structures. *Dissertation*, Technische Universität Berlin (D 83).
- Steinhagen, U. (2001). Synthesizing Nonlinear Transient Gravity Waves in Random Seas. *Dissertation*, Technische Universität Berlin (D83).
- Mei, C. (1983). *The applied dynamics of ocean surface waves*. A wiley-Interscience publication. Wiley.
- Mei, C. (1989). *The applied dynamics of ocean surface waves*, volume 1 of *Advanced Series on Ocean Engineering*. World Scientific, 2 edition.
- Miche, A. (1944). *Mouvements ondulatoires de la mer en profondeur constante de décroissante*. Ann. Ponts et Chaussees.
- Mori, N., Yasuda, T., and Nakayama, S. (2000). Statistical Properties of Freak Waves Observed in the Sea of Japan. In *Proceedings of the 10th Interational Offshore and Polar Engineering Conference (ISOPE)*, Vol. III, pages 109–122, Seattle, USA.

## Bibliography

---

- Morison, J., O'Brian, M., Johnson, J., and Schaaf, S. (1950). The force exerted by surface waves on piles. *Pet. Trans. AIME*, 189(T.P. 2846):149–157.
- Newman, J. (1977). *Marine Hydrodynamics*. The MIT Press, Cambridge, Massachusetts.
- Newman, J. (1986). Distributions of sources and dipoles over a quadrilateral panel. *Journal of Engineering Mathematics*, 20:113–126.
- Newman, J. N. (1985). Algorithms for the Free-Surface Green function. *Journal of Engineering Mathematics*, 19:57–67.
- Onorato, M., Osborne, A., Serio, M., Cavaleri, L., Brandini, C., and Stansberg, C. (2006). Extreme waves, modulational instability and second order theory: wave flume experiments on irregular waves. *European Journal of Mechanics-B/Fluids*, Vol. 25, (5):586–601.
- Onorato, M., Osborne, A., Serio, M., and Damiani, T. (2000). Occurrence of freak waves from envelope equations in random ocean wave simulation. In Olagnon, M., editor, *Rogue Waves 2000*, Brest, France.
- Onorato, M., Osborne, A. R., Serio, M., and Bertone, S. (2001a). Freak waves in random oceanic sea states. *Physical Review Letter*, Vol. 86, (25):5831–5834.
- Onorato, M., Osborne, A. R., Serio, M., and Bertone, S. (2001b). Freak waves in random oceanic sea states. *Phys. Rev. Lett.*, Vol. 86, (25):5831–5834.
- Onorato, M., Osborne, A. R., Serio, M., and Cavaleri, L. (2005). Modulational instability and non-gaussian statistics in experimental random water-wave trains. *Physics of Fluids* 17, 078101.
- Onorato, M., Osborne, A. R., Serio, M., Cavaleri, L., Brandini, C., and Stansberg, C. T. (2003). Extreme waves and modulational instability: wave flume experiments on irregular waves. *ArXiv Nonlinear Sciences e-prints*.
- Peregrine, D. (1983). Water waves, nonlinear Schrödinger equations and their solutions. *J. Austral. Math. Soc. Ser. B*, 25(1), pages 16–43.
- Petrova, P. G., Arena, F., and Soares, C. G. (2011). Space-time evolution of random wave groups with high waves based on the quasi-determinism theory. *Ocean Engineering*, 38:1640 – 1648.
- Rajendran, S., Fonseca, N., Guedes Soares, C., Clauss, G., and Klein, M. (2011). Time Domain Comparison with Experiments for Ship Motions and Strural Loads on a Container Vessel in Abnormal Waves. In *OMAE 2011 - 30th International Conference on Offshore Mechanics and Arctic Engineering*, Rotterdam, The Netherlands. OMAE2011-50316.
- Rowan, T. (1990). *Functional Stability Analysis of Numerical Algorithms*. PhD thesis, University of Texas at Austin.

- Salvesen, N., Tuck, E., and Faltinsen, O. (1970). Ship motions and sea loads. In *Trans. SNAME 78*.
- Sand, S. E., Ottesen, H. N. E., Klinting, P., Gudmestadt, O. T., and Sterndorff, M. J. (1990). *Freak Wave Kinematics*, pages 535–549. Kluwer Academic Publisher, NATO ASI Series edition.
- Scardovelli, R. and Zaleski, S. (1999). Direct numerical simulation of free-surface and interfacial flow. *Annu. Rev. Fluid Mech.*, 31:567–603.
- Schäffer, H. A. (1996). Second-Order Wavemaker Theory for Irregular Waves. *Ocean Engineering*, 23(1):47–88.
- Schmittner, C. and Hennig, J. (2012). Optimization of short-crested deterministic wave sequences via a phase-amplitude iteration scheme. In *OMAE 2012 - 31st International Conference on Ocean, Offshore and Arctic Engineering*, Rio de Janeiro, Brazil. OMAE2012-83150.
- Schulz, M. (2001). "Ich spürte den Atem Gottes". *Der Spiegel*. No. 51/2001.
- Serio, M., Onorato, M., Osborne, A., and Janssen, P. (2005). On the computation of the benjamin-feir index. *Nuovo Cimento della Societa Italiana di Fisica C - Geophysics and Space Physics*, 28(6):893–903.
- Shrira, V. and Geogjaev, V. (2010). What makes the peregrine soliton so special as a prototype of freak waves? *Journal of Engineering Mathematics*, 67(1), pages 11–22.
- Skjelbreia, L. and Hendrickson, J. A. . (1961). Fifth order gravity wave theory. In *Proc. 7th Conf. Coastal Engineering*, pages 184–196, The Hague, Netherlands.
- Slunyaev, A., Clauss, G. F., Klein, M., and Onorato, M. (2013). Simulations and experiments of short intense envelope solitons of surface water waves. *Physics of Fluids (1994-present)*, 25(6):–.
- Slunyaev, A., Pelinovsky, E., and C., G. S. (2005). Modeling freak waves from the North Sea. In *Applied Ocean Research* 27, pages 12–22.
- Sobey, P. J. (1997). Linear and nonlinear Wave Theory. Course Notes, Leichtweiß - Institut für Wasserbau, Braunschweig.
- Sobey, R. (1999). Real Sea States. *Advanced Short Course*. Lecture notes, Braunschweig.
- Sobey, R. and Young, I. (1986). Hurricane wind waves - a discrete spectral model. *Journal of Waterway, Port, Coastal, and Ocean Engineering*, 112:370–389.
- St. Denis, M. and Pierson, W. (1953). On the motions of ships in confused seas. *Transactions, SNAME*. 61.

## Bibliography

---

- Stansberg, C. T. (1997). On the Nonlinear Behaviour of Ocean Wave Groups. In *The third International Symposium on Ocean Wave Measurement and Analysis*, Virginia Beach, VA, USA.
- Stokes, G. G. (1849). On the Theory of Oscillatory Waves. In *Trans. Cambridge Philos. Soc.*, pages 441–455.
- Svendsen, I. A. (1985). *Physical modeling of in coastal engineering*, chapter Physical modeling of water waves, pages 13–47. Balkema.
- Toffoli, A., Babanin, A., Onorato, M., and Waseda, T. (2010). Maximum steepness of oceanic waves: Field and laboratory experiments. *Geophysical Research Letters*, 37(5), pages 790–795.
- Torhaug, R., Winterstein, S. R., and Braathen, A. (1998). Nonlinear ship loads: stochastic models for extreme response. In *Journal of Ship Research*, volume 42(1), pages 46–55.
- Tromans, P. S., Anaturk, A. R., and Hagemeijer, P. (1991). A new model for the kinematics of large ocean waves - application as a design wave. In *Proceedings of the First International Offshore and Polar Engineering Conference (ISOPE)*, pages 64–71, Edinburgh, United Kingdom.
- Trulsen, K. (2001). Simulating the Spatial Evolution of a Measured Time Series of a Freak Wave. In *Proc. of the Workshop "Rogue Waves 2000"*, ed. M. Olagnon and G.A. Athanassoulis, pages 265–274, Brest, France.
- Trulsen, K. and Dysthe, K. B. (1997). Freak Waves - a three-dimensional Wave Simulation. In *Proceedings of the 21st Symposium on Naval Hydrodynamics*, pages 550–560, Washington, DC.
- van Groesen, E., Andonowati, A., and Karjanto, N. (2006). Displaced phase-amplitude variables for waves on finite background. *Physics Letters A*, Vol. 354, (4):312–319.
- WAMIT (1994). *WAMIT Version 5.1 – A Radiation-Diffraction Panel Program For Wave-Body Interactions*. Department of Ocean Engineering, MIT. User-guide.
- Watanabe, I., Keno, M., and Sawada, H. (1989). Effect of bow flare on shape to wave loads of a container ship. *J Soc Nav Archit Jpn*, 166:259–266.
- Westhuis, J. H. (2001). *The numerical simulation of nonlinear waves in a hydrodynamic model test basin*. PhD thesis, Universiteit Twente.
- Wheeler, J. (1970). Method of calculating forces produced by irregular waves. *J. of Petroleum Technology*, pages 359–367.
- Wolfram, J., Linfoot, B., and Stansell, P. (2000). Long- and short-term extreme Wave Statistics in the North Sea: 1994–1998. In *Rogue Waves 2000*, pages 363–372, Brest, France.

- Yuen, H. C. and Lake, B. M. (1975). Nonlinear deep water waves: Theory and experiments. *Physics of Fluids*, Vol. 18, pages 956–960.
- Yuen, H. C. and Lake, B. M. (1980). Instabilities of waves on deep water. *Annual Review of Fluid Mechanics*, 12(1):303–334.
- Zakharov, V. E. (1968). Stability of periodic waves of finite amplitude on the surface of a deep fluid. *translated in: Journal of Applied Mechanics and Technical Physics*, Vol. 9, pages 190–194.
- Zakharov, V. E. and Ostrovsky, L. (2009). Modulation instability: the beginning. *Physica D: Nonlinear Phenomena*, 238(5), pages 540–548.
- Zakharov, V. E. and Shabat, A. B. (1971). Exact theory of two-dimensional self-focussing and one-dimensional self-modulating waves in nonlinear media. *translated in: Journal of Experimental and Theoretical Physics (JETP 34 ":" 62-69)*, Vol. 2, pages 118–134.



## List of Abbreviations

<b>AAF</b>	Amplitude Amplification Factor
<b>BFI</b>	Benjamin-Feir Index
<b>CEHIPAR</b>	Canal de Experiencias Hidrodinámicas de El Pardo
<b>CFD</b>	Computational Fluid Dynamics
<b>CRRW</b>	Conditional Random Response Wave
<b>CWE</b>	Critical Wave Episode
<b>FEM</b>	Finite Element Method
<b>FFT</b>	Fast Fourier Transform
<b>FPSO</b>	Floating Production, Storage and Offloading
<b>F2T+</b>	Improved Frequency to Time Domain
<b>GRP</b>	Glass-fibre Reinforced Plastic
<b>IFFT</b>	Inverse Fast Fourier Transform
<b>IST</b>	Instituto Superior Técnico
<b>JONSWAP</b>	Joint North Sea Wave Observation Project
<b>LNG</b>	Liquefied Natural Gas
<b>MLER</b>	Most Likely Extreme Response
<b>MLRW</b>	Most Likely Response Wave
<b>MLW</b>	Most Likely Wave
<b>MPLS20</b>	Maritime Pipe Loading System 20"
<b>MTA</b>	Maximum Temporal Amplitude
<b>NLS</b>	Non-Linear Schrödinger-type
<b>NM</b>	New Method
<b>NYW</b>	New Year Wave
<b>PD</b>	Phase Distribution
<b>PDF</b>	Probability Density Function

*List of Abbreviations*

---

<b>RAO</b>	Response Amplitude Operator
<b>RP</b>	RandomPhases
<b>SFB</b>	Soliton on Finite Background
<b>TNLS</b>	Time Non-Linear Schrödinger-type
<b>TUB</b>	Technische Universität Berlin
<b>WAMIT</b>	Wave Analysis at Massachusetts Institute of Technology
<b>WAVETUB</b>	WAVE simulation tool developed at Technische Universität Berlin

## Nomenclature

$(2s)_s$	Significant double amplitude	
$(2s)_{max}$	Probable maximum double amplitude	
$(2s)_{s,tol}$	Tolerable significant double amplitude	
$(2s_{z,rel})_{max}$	Probable maximum double amplitude of the vertical relative motion	[m]
$(2s_{z,rel})_{s,tol}$	Tolerable significant double amplitude of the vertical relative motion	[m]
$(2s_{z,rel})_{tol}$	Maximum tolerable double amplitude of the vertical relative motion	[m]
$(s_{z,rel})$	Amplitude of the vertical relative motion	[m]
$A$	Matrix of added masses	
$A_B$	Breather envelope	[m]
$A_S$	Envelope Soliton	[m]
$A_c$	Carrier wave envelope	[m]
$B$	Matrix of potential damping	
$C$	Matrix of restoring forces	
$C_g$	Group velocity	[ $\frac{m}{s}$ ]
$C_p$	Wave celerity	[ $\frac{m}{s}$ ]
$C_{\bar{E}}$	Celerity of mean energy propagation	[ $\frac{m}{s}$ ]
$C_a$	Hydrodynamic mass coefficient	[ $-$ ]
$C_{crest}$	Wave crest celerity	[ $\frac{m}{s}$ ]
$C_d$	Drag coefficient	[ $-$ ]

## Nomenclature

---

$C_m$	Mass coefficient	[−]
$D$	Characteristic dimension of a structure	[m]
$E$	Wave energy	[ $m^2$ ]
$E_H$	Energy envelope	[ $m^2$ ]
$F$	Fourier transform	[ms]
$F_N$	Normal force	[N]
$F_{dyn}$	Force due to dynamic pressure	[N]
$F_x$	Horizontal force	[N]
$H$	Wave height	[s]
$H_s$	Significant wave height	[m]
$H_{max}$	Maximum wave height	[m]
$H_{s,tol}$	Tolerable significant wave height	[m]
$K$	Impulse response function	
$KC$	Keulegan-Carpenter-Coefficient	[−]
$L$	Wave length	[m]
$L_c$	Carrier wave length	[m]
$L_{pp}$	Length between perpendicular	[m]
$M$	Matrix of rigid body masses	
$N$	Number of waves	[−]
$RAO$	Response amplitude operator	
$RAO_s$	Significant response amplitude operator	
$S_S$	Response spectrum	[ $m^2 s; rad^2 s$ ]
$S_\zeta$	Energy density spectrum	[ $m^2 s$ ]
$S_b$	Wetted surface of submerged body	[ $m^2$ ]
$T$	Period	[s]

$T_0$	Zero-upcrossing wave period	[s]
$T_1$	Modal wave period	[s]
$T_P$	Zero-upcrossing period	[s]
$T_c$	Carrier wave period	[s]
$U$	Velocity	$[\frac{m^2}{s}]$
$\Phi$	Flow potential	$[\frac{m^2}{s}]$
$\Phi_0$	Incident wave field potential	$[\frac{m^2}{s}]$
$\Phi_7$	Scattering wave field potential	$[\frac{m^2}{s}]$
$\Phi_R$	Cumulative Rayleigh distribution function	[−]
$\Phi_S$	Steady perturbation potential	$[\frac{m^2}{s}]$
$\Phi_j$	Radiation wave field potential	$[\frac{m^2}{s}]$
$\Phi_{(2s)max}$	Cumulative Rayleigh density function of maximum response	
$\Phi_{H_{max}}$	Cumulative Rayleigh density function of maximum wave heights	$[m^{-1}]$
$\alpha$	NLS coefficient for finite water depth in space domain	[−]
$\alpha'$	NLS coefficient for finite water depth in time domain	$[\frac{s^2}{m}]$
$\beta$	NLS coefficient for finite water depth in space domain	[−]
$\beta'$	NLS coefficient for finite water depth in time domain	$[m^{-3}]$
$\chi$	Space variable	[−]
$\delta$	Perturbation parameter	[−]
$\delta$	Shallowness parameter	[−]
$\dot{u}$	Horizontal particle acceleration	$[\frac{m}{s^2}]$

## Nomenclature

---

$\dot{w}$	Vertical particle acceleration	$[\frac{m}{s^2}]$
$\epsilon$	Wave steepness	$[ - ]$
$\eta$	Modulation wave number	$[\frac{1}{m}]$
$\gamma$	Spectrum enhancement factor	$[ - ]$
$\hat{F}$	Hilbert transform	$[ms]$
$\hat{\alpha}$	NLS coefficient for finite water depth in space domain	$[ - ]$
$\hat{\beta}$	NLS coefficient for finite water depth in space domain	$[ - ]$
$\hat{\epsilon}$	Amplitude parameter	$[ - ]$
$\hat{\phi}$	Phase shift between response and excitation	$[rad]$
$\hat{\tau}$	Time variable	$[s]$
$\mu$	Relative spectral bandwidth	$[ - ]$
$\nu$	Group velocity correction term in finite water depth	$[ - ]$
$\omega$	Wave frequency	$[\frac{rad}{s}]$
$\omega_1$	Modal wave frequency	$[\frac{rad}{s}]$
$\omega_P$	Peak wave frequency	$[\frac{rad}{s}]$
$\omega_c$	Carrier wave frequency	$[\frac{rad}{s}]$
$\bar{E}$	Mean energy distribution	$[\frac{kg}{s^2}]$
$\partial$	Partial derivative	
$\phi$	Wave phase angle	$[rad]$
$\phi_R$	Rayleigh distribution	$[m^{-1}]$
$\phi_{(2s)max}$	PDF of maximum response	
$\phi_{H_{max}}$	PDF of maximum wave heights	$[m^{-1}]$
$\rho$	Density of the fluid	$[\frac{kg}{m^3}]$

$\sigma$	Modulation wave number	$[\frac{1}{m}]$
$\sigma$	Standard deviation	$[m]$
$\sigma^2$	Variance of the sea state	$[m^2]$
$\tau$	Time variable	$[-]$
$\theta$	Wave direction	$[rad]$
$\tilde{\Phi}$	Non-dimensional potential	$[-]$
$\tilde{\epsilon}$	Spectral Width	$[-]$
$\tilde{\eta}$	Normalized modulation wave number	$[-]$
$\tilde{\nu}$	Normalized modulation frequency	$[-]$
$\tilde{\nu}$	Spectral Width	$[-]$
$\tilde{\sigma}$	Normalized modulation wave number	$[-]$
$\tilde{\vartheta}$	Normalized modulation frequency	$[-]$
$\tilde{\zeta}$	Non-dimensional surface elevation	$[-]$
$\tilde{t}$	Non-dimensional time	$[-]$
$\tilde{x}, \tilde{z}$	Non-dimensional cartesian coordinates	$[-]$
$\Delta k$	Spectral bandwidth	$[\frac{rad}{m}]$
$\Delta k$	Wave number shift	$[\frac{rad}{s}]$
$\Delta t$	Time shift	$[s]$
$\Delta$	Laplace operator	
$\Delta\omega$	Frequency shift	$[\frac{rad}{s}]$
$\underline{F}_e$	Vector of excitation forces	
$\ddot{\underline{s}}$	Vector of body accelerations	
$\dot{\underline{s}}$	Vector of body velocities	
$\underline{s}$	Vector of body motions	
$v$	Modulation frequency	$[\frac{1}{s}]$

## Nomenclature

---

$\vartheta$	Modulation frequency	$[\frac{1}{s}]$
$\hat{\zeta}$	Complex analytical signal	$[m]$
$\xi$	Space variable	$[-]$
$\zeta$	Surface elevation	$[m]$
$\zeta_H$	Real part of the Hilbert transformation	$[m]$
$\zeta_a$	Wave amplitude	$[m]$
$\zeta_c$	Wave crest height	$[m]$
$\zeta_{WG}$	Wave group elevation	$[m]$
$a_c$	Carrier wave amplitude	$[m]$
$c_{med}$	Mean energy distribution centroid	$[s]$
$d$	Water depth	$[m]$
$f_d$	Viscous force	$[N]$
$f_m$	Inertia force	$[N]$
$g$	Acceleration of gravity	$[\frac{m}{s^2}]$
$k$	Wave number	$[\frac{rad}{m}]$
$k_c$	Carrier wave number	$[\frac{rad}{m}]$
$m_j$	Spectral moment	
$p_{dyn}$	Dynamic pressure	$[Pa]$
$s$	Structure response	$[m]$
$s_a$	Response amplitude	$[m]$
$t$	Time	$[s]$
$u$	Horizontal particle velocity	$[\frac{m}{s}]$
$vbm$	Vertical wave bending moment	$[kNm]$
$w$	Vertical particle velocity	$[\frac{m}{s}]$

$x, y, z$	Cartesian coordinates	[m]
$x_B$	Wave board motion	[m]
$x_t$	target location	[m]



## A. Test Facilities

The experiments performed for this thesis are conducted in the seakeeping basin at Technische Universität Berlin (TUB) and at Canal de Experiencias Hidrodinámicas de El Pardo (CEHIPAR).

### A.1. Seakeeping Basin at TUB

The seakeeping basin (Fig. A.1) at TUB is 110m long, with a measuring range of 90m. The width is 8m and the water depth is 1m. On the one side an electrically driven wave generator is installed which can be utilized in flap-type and piston-type mode. The wave generator is fully computer controlled and a software is implemented which enables the generation of regular waves, transient wave packages, deterministic irregular sea states with defined characteristics as well as tailored critical wave sequences. On the opposite side, a wave damping slope is installed to suppress disturbing wave reflections.

#### A.1.1. Multi-Body Offshore Operation

Figure A.2 presents the test setup of the investigated multi-body offshore operation addressing the LNG transfer between a turret moored terminal barge and a shuttle carrier. Table A.1 presents the main dimensions of the investigated multi-body offshore system. For the model tests glass-fibre reinforced plastic (GRP) models of the LNG carrier and the terminal barge are built at a scale of 1 : 100 (see Fig. A.2). The carrier model is soft-moored and both vessels are equipped with four wireless, individually pulsed infrared sensors each. The body motions in six degrees of freedom are tracked by five cameras mounted on a carriage above the basin with a tracking range of 8m × 10m.

#### A.1.2. Chemical Tanker

The investigated chemical tanker model is made of glass-fibre reinforced plastic (GRP) at a scale of 1 : 70 (see Fig. A.3). Figure A.3 shows the model test setup and Tab. A.2 the corresponding main dimensions. The model is segmented at  $L_{pp}/2$  and connected with three force transducers. Two are mounted on deck; one on each side, the third one is mounted underneath the keel. The force transducers register the longitudinal forces during the model tests. Based on the measured forces and the given geometrical arrangement of the three force transducers, the

## A. Test Facilities

---



**Figure A.1.:** TUB seakeeping basin.

resulting vertical wave bending moment at water line level and the longitudinal forces are obtained. The strain gauges feature a nominal load of 200kg and a protection class of IP68 (100h at 1m water column). In addition, the model is equipped with pressure transducers at bow and stern. Furthermore, two wave gauges are installed on deck at the forecastle to detect the green water impact on deck - absolute, measurable green water height on deck is approx. 13m (front gauge) and 9m (rear gauge) at full scale (cf. Fig. A.3). The ship motions are recorded by an optical tracking system consisting of five cameras with a tracking range of 8m × 10m.

During the tests, the chemical tanker is towed with an elastic suspension system using a triangular towing arrangement. The longitudinal motions are restricted by a spring in front of and a counter weight behind the model. The suspension system is connected with the ship model by a thin elastic cross bar, which is mounted on deck of the aft segment (centre of gravity in x-direction). With this arrangement, heave and pitch motions remain unrestrained.

For the evaluation of the suspension system, i.e. to ensure that the measurements are unaffected, the chemical tanker is investigated with different suspension system configurations. Thereby, the model is tested in regular and irregular waves in four different configurations – suspension system mounted at the fore ship, at the aft ship, rigid suspension (without spring) and free floating. Firstly, the chemical



**Figure A.2.:** Model test setup of the multi-body offshore system.

tanker is investigated in a high, steep regular wave ( $H = 13m$ ) with a wave length of  $L_w/L_{pp} = 1.1$  to select a worst case wave length regarding maximum vertical bending moment as well as asymmetry of the vertical bending moment. Afterwards, the suspension system is checked in irregular sea states as well as in the NYW.

Figure A.4 illustrates the measured vertical bending moment at  $L_{pp}/2$  with (blue curve) and without the suspension system (red curve). Comparing the mean values between  $t = 85s$  and  $t = 130s$  reveal a variance of less than 2% for the absolute vertical bending moment.

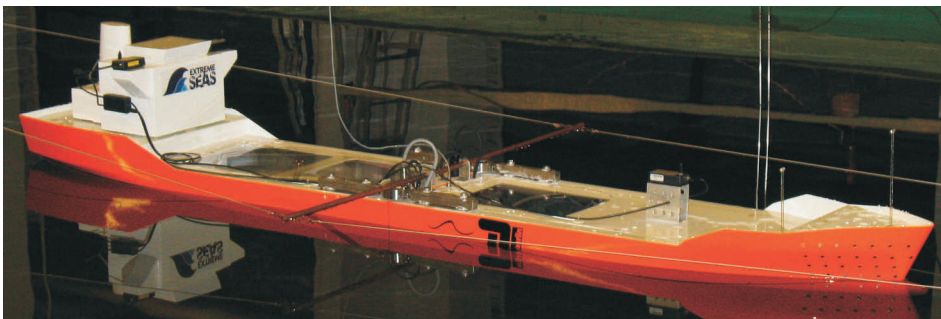


**Figure A.3.:** Model test setup of the chemical tanker model.

## A. Test Facilities

---

**Table A.1.:** Main Dimensions of the LNG Carrier and the Terminal.

Parameter	Terminal	Carrier
Length over all	360m (+ 40m mooring wings)	282m
Breadth	65m	42m
Draught	12m	12m
Height	33m	26m
Displacement	275087m <sup>3</sup>	103921m <sup>3</sup>

**Table A.2.:** Main Dimensions of the Chemical Tanker.

			Chemical Tanker
Length	[m]	$L_{pp}$	161
Breadth	[m]	$B_{WL}$	28
Draught	[m]	$D_{ms}$	9
Displacement	[t]	$\Delta$	30666
Block coefficient	[ $-$ ]	$c_B$	0.75

Figure A.5 presents the results in irregular waves. This diagram compares results obtained with rigid suspension (without spring), with suspension mounted at fore and aft ship as well as free floating. The two top diagrams compare the results for the spring suspension system and the rigid suspension system for the cruising vessel. The next two diagrams compare the vertical bending moment with spring suspension system mounted at fore and aft ship for the cruising vessel and the last two diagrams present the results for fore ship mounted suspension system with the free floating ship at stationary conditions. The diagrams reveal that all configurations lead to the same result, i.e. the type of suspension system does not influence the vertical bending moment results significantly. Phase shifts and slight deviations are explainable with slightly different encountering wave fields due to small differences of the ship's position during the different tests. Altogether, this investigations proof that the influence of the suspension system is negligible.

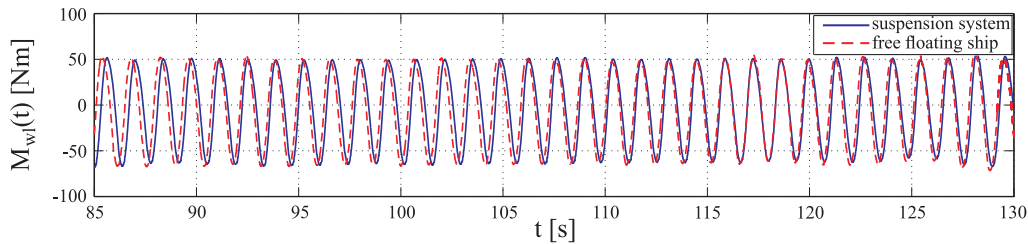


**Figure A.4.:** Test of the suspension system in regular waves.

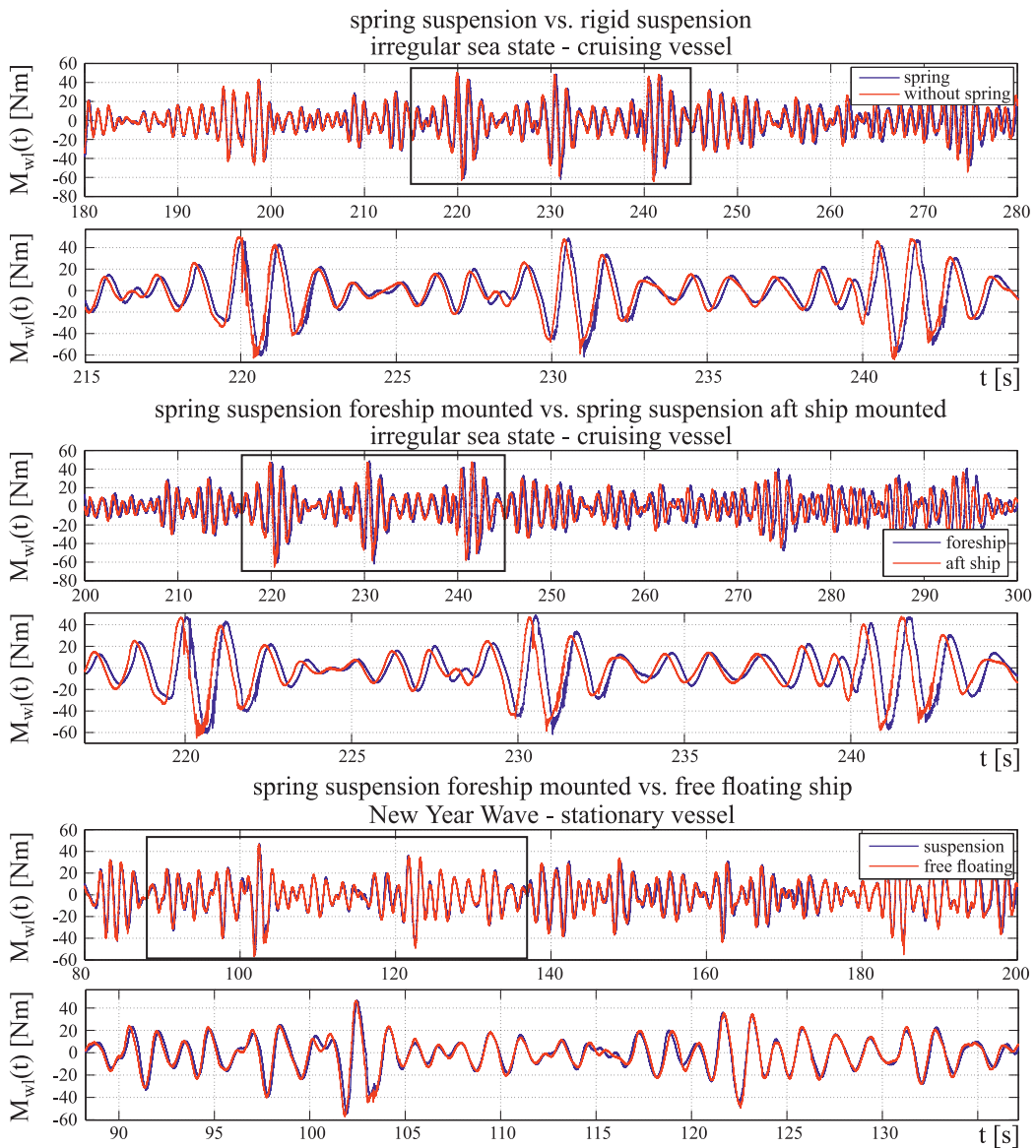


**Figure A.5.:** Test of the suspension system with different configurations in irregular sea states.



*Figure A.6.: CEHIPAR seakeeping basin.*

## A.2. Seakeeping Basin at CEHIPAR

The seakeeping basin at CEHIPAR (Fig. A.6) is 150m long, 30m wide and the water depth is 5m. For very deep water experiments such as testing of fixed platforms, a pit of  $10m \times 10m$  and 10m water depth is located near the wave maker. The flap-type wave maker is located on one of the smaller sides, feature the same wide (30m) and consist of 60 individual flaps, which enables also the generation of short-crested sea states. On the opposite side, a wave damping slope is installed. The wave generator is fully computer controlled and the installed software enables the generation of regular and irregular waves.

## B. Derivation of the Non-Linear Schrödinger-Type Equation

This chapter presents a detailed derivation of the NLS equation following the procedure presented by Johnson (1997). The NLS equation can be formally derived from the potential water wave equations under the hypothesis of small amplitudes and quasi-monochromatic waves. The starting point is potential theory under the assumption that the Newtonian fluid is incompressible, inviscid and irrotational resulting in the following governing equations for the two-dimensional water wave problem

$$\begin{aligned} \Phi_{xx} + \Phi_{zz} &= 0, \\ \Phi_z &= \Phi_x \zeta_x + \zeta_t, & z &= \zeta(x, t) \\ g\zeta + \frac{1}{2} [(\Phi_x)^2 + (\Phi_z)^2] + \Phi_t &= 0, & z &= \zeta(x, t) \\ \Phi_z &= 0. & z &= -d \end{aligned} \quad (\text{B.1})$$

The bottom of the fluid domain is considered to be level, rigid and impermeable.

At the beginning, the following non-dimensionalisations are introduced

$$x \rightarrow \frac{1}{k} \cdot \tilde{x}; \quad z \rightarrow d \cdot \tilde{z}; \quad t \rightarrow \frac{1}{\omega} \cdot \tilde{t}; \quad \zeta = a \cdot \tilde{\zeta}; \quad \Phi = a \frac{\omega}{k^2 d} \tilde{\Phi}; \quad (\text{B.2})$$

where  $a$  is a typical amplitude,  $k$  defines a typical wave length and  $\omega/k$  is the characteristic speed with  $\omega = k\sqrt{gd}$  for the speed scale. The choice of the shallow water speed scale “is still useful even if we do not study, specifically, long gravity waves” (Johnson, 1997).

The following transformations are now used

$$\begin{aligned} \zeta_x &= \frac{\partial}{\partial \tilde{x}} a \tilde{\zeta} \frac{\partial \tilde{x}}{\partial x} & = a k \tilde{\zeta}_{\tilde{x}}; \\ \zeta_t &= \frac{\partial}{\partial \tilde{t}} a \tilde{\zeta} \frac{\partial \tilde{t}}{\partial t} & = a \omega \tilde{\zeta}_{\tilde{t}}. \\ \Phi_x &= \frac{\partial}{\partial \tilde{x}} a \frac{\omega}{k} \tilde{\Phi} \frac{\partial \tilde{x}}{\partial x} & = a \frac{\omega}{kd} \tilde{\Phi}_{\tilde{x}}; \\ \Phi_z &= \frac{\partial}{\partial \tilde{z}} a \frac{\omega}{k} \tilde{\Phi} \frac{\partial \tilde{z}}{\partial z} & = a \frac{\omega}{k^2 d^2} \tilde{\Phi}_{\tilde{z}}; \\ \Phi_t &= \frac{\partial}{\partial \tilde{t}} a \frac{\omega}{k} \tilde{\Phi} \frac{\partial \tilde{t}}{\partial t} & = a \frac{\omega^2}{k^2 d} \tilde{\Phi}_{\tilde{t}}; \\ \Phi_{xx} &= \frac{\partial}{\partial \tilde{x}} \left( \frac{\partial}{\partial \tilde{x}} a \frac{\omega}{k} \tilde{\Phi} \frac{\partial \tilde{x}}{\partial x} \right) \frac{\partial \tilde{x}}{\partial x} & = a \frac{\omega}{d} \tilde{\Phi}_{\tilde{x}\tilde{x}}; \\ \Phi_{zz} &= \frac{\partial}{\partial \tilde{z}} \left( \frac{\partial}{\partial \tilde{z}} a \frac{\omega}{k} \tilde{\Phi} \frac{\partial \tilde{z}}{\partial z} \right) \frac{\partial \tilde{z}}{\partial z} & = a \frac{\omega}{k^2 d^3} k \tilde{\Phi}_{\tilde{z}\tilde{z}}; \end{aligned} \quad (\text{B.3})$$

to arrive at the non-dimensional governing equations

$$\begin{aligned}\tilde{\Phi}_{\tilde{z}\tilde{z}} + \delta^2 \tilde{\Phi}_{\tilde{x}\tilde{x}} &= 0, \\ \tilde{\Phi}_{\tilde{z}} &= \delta^2 \left( \tilde{\zeta}_{\tilde{t}} + \hat{\epsilon} \tilde{\Phi}_{\tilde{x}} \tilde{\zeta}_{\tilde{x}} \right), \quad \tilde{z} = \hat{\epsilon} \tilde{\zeta}(\tilde{x}, \tilde{t}) \\ \tilde{\zeta} + \tilde{\Phi}_{\tilde{t}} + \frac{1}{2} \hat{\epsilon} \left( \tilde{\Phi}_{\tilde{x}}^2 + \frac{1}{\delta^2} \tilde{\Phi}_{\tilde{z}}^2 \right) &= 0, \quad \tilde{z} = \hat{\epsilon} \tilde{\zeta}(\tilde{x}, \tilde{t}) \\ \tilde{\Phi}_{\tilde{z}} &= 0, \quad \tilde{z} = -1\end{aligned}\tag{B.4}$$

with  $\delta = kd$  as “shallowness” parameter and  $\hat{\epsilon} = ka/kd = a/d$  as amplitude parameter for fixed water depth  $d$  (Johnson, 1997).

The so far unknown solution is allowed to evolve slowly on scales determined by  $\hat{\epsilon}$  (Johnson, 1997). The following relevant scales are introduced

$$\xi = \tilde{x} - C_p \tilde{t}; \quad \chi = \hat{\epsilon}(\tilde{x} - C_g \tilde{t}); \quad \tau = \hat{\epsilon}^2 \tilde{t}\tag{B.5}$$

resulting in the following transformations

$$\begin{aligned}\tilde{\zeta}_{\tilde{x}} &= \tilde{\zeta}_{\xi} + \hat{\epsilon} \tilde{\zeta}_{\chi}, \\ \tilde{\zeta}_{\tilde{t}} &= \hat{\epsilon}^2 \tilde{\zeta}_{\tau} - C_p \tilde{\zeta}_{\xi} - \hat{\epsilon} C_g \tilde{\zeta}_{\chi}, \\ \tilde{\Phi}_{\tilde{x}} &= \tilde{\Phi}_{\xi} + \hat{\epsilon} \tilde{\Phi}_{\chi}, \\ \tilde{\Phi}_{\tilde{t}} &= \hat{\epsilon}^2 \tilde{\Phi}_{\tau} - C_p \tilde{\Phi}_{\xi} - \hat{\epsilon} C_g \tilde{\Phi}_{\chi}, \\ \tilde{\Phi}_{\tilde{x}\tilde{x}} &= \tilde{\Phi}_{\xi\xi} + 2\hat{\epsilon} \tilde{\Phi}_{\xi\chi} + \hat{\epsilon}^2 \tilde{\Phi}_{\chi\chi}.\end{aligned}\tag{B.6}$$

Thus, the governing equations become

$$\begin{aligned}\tilde{\Phi}_{\tilde{z}\tilde{z}} + \delta^2 \left( \tilde{\Phi}_{\xi\xi} + 2\hat{\epsilon} \tilde{\Phi}_{\xi\chi} + \hat{\epsilon}^2 \tilde{\Phi}_{\chi\chi} \right) &= 0, \\ \tilde{\Phi}_{\tilde{z}} &= \delta^2 \left[ \hat{\epsilon}^2 \tilde{\zeta}_{\tau} - C_p \tilde{\zeta}_{\xi} - \hat{\epsilon} C_g \tilde{\zeta}_{\chi} + \hat{\epsilon} \left( \tilde{\Phi}_{\xi} + \hat{\epsilon} \tilde{\Phi}_{\chi} \right) \left( \tilde{\zeta}_{\xi} + \hat{\epsilon} \tilde{\zeta}_{\chi} \right) \right], \\ \tilde{\zeta} + \hat{\epsilon}^2 \tilde{\Phi}_{\tau} - C_p \tilde{\Phi}_{\xi} - \hat{\epsilon} C_g \tilde{\Phi}_{\chi} + \frac{1}{2} \hat{\epsilon} \left( \left( \tilde{\Phi}_{\xi} + \hat{\epsilon} \tilde{\Phi}_{\chi} \right)^2 + \frac{1}{\delta^2} \tilde{\Phi}_{\tilde{z}}^2 \right) &= 0, \\ \tilde{\Phi}_{\tilde{z}} &= 0,\end{aligned}\tag{B.7}$$

with  $\tilde{z} = \hat{\epsilon} \tilde{\zeta}$  for the surface boundary conditions and  $\tilde{z} = -1$  for the bottom boundary condition. The unknown potential  $\tilde{\Phi}$  and surface elevation  $\tilde{\zeta}$  can be approximated by asymptotic perturbation expansions

$$\tilde{\Phi} \approx \sum_{n=0}^{\infty} \hat{\epsilon}^n \tilde{\Phi}^{(n)}(\xi, \chi, \tau, \tilde{z}); \quad \tilde{\zeta} \approx \sum_{n=0}^{\infty} \hat{\epsilon}^n \tilde{\zeta}^{(n)}(\xi, \chi, \tau, \tilde{z}).\tag{B.8}$$

Applying the perturbation expansions in the governing equations (B.7) and truncation at order  $\mathcal{O}(\hat{\epsilon}^2)$  gives:

Laplace Equation

$$\begin{aligned}\tilde{\Phi}_{\tilde{z}\tilde{z}}^{(0)} + \hat{\epsilon} \tilde{\Phi}_{\tilde{z}\tilde{z}}^{(1)} + \hat{\epsilon}^2 \tilde{\Phi}_{\tilde{z}\tilde{z}}^{(2)} + \delta^2 \left[ \tilde{\Phi}_{\xi\xi}^{(0)} + \hat{\epsilon} \tilde{\Phi}_{\xi\xi}^{(1)} + \hat{\epsilon}^2 \tilde{\Phi}_{\xi\xi}^{(2)} \right. \\ \left. + 2\hat{\epsilon} \left( \tilde{\Phi}_{\xi\chi}^{(0)} + \hat{\epsilon} \tilde{\Phi}_{\xi\chi}^{(1)} + \hat{\epsilon}^2 \tilde{\Phi}_{\xi\chi}^{(2)} \right) + \hat{\epsilon}^2 \left( \tilde{\Phi}_{\chi\chi}^{(0)} + \hat{\epsilon} \tilde{\Phi}_{\chi\chi}^{(1)} + \hat{\epsilon}^2 \tilde{\Phi}_{\chi\chi}^{(2)} \right) \right] &= 0\end{aligned}\tag{B.9}$$

---

### Kinematic Boundary Condition

$$\begin{aligned} \tilde{\Phi}_{\tilde{z}}^{(0)} + \hat{\epsilon} \tilde{\Phi}_{\tilde{z}}^{(1)} + \hat{\epsilon}^2 \tilde{\Phi}_{\tilde{z}}^{(2)} &= \delta^2 \left[ \hat{\epsilon}^2 \left( \tilde{\zeta}_\tau^{(0)} + \hat{\epsilon} \tilde{\zeta}_\tau^{(1)} + \hat{\epsilon}^2 \tilde{\zeta}_\tau^{(2)} \right) \right. \\ &\quad - C_p \left( \tilde{\zeta}_\xi^{(0)} + \hat{\epsilon} \tilde{\zeta}_\xi^{(1)} + \hat{\epsilon}^2 \tilde{\zeta}_\xi^{(2)} \right) - \hat{\epsilon} C_g \left( \tilde{\zeta}_\chi^{(0)} + \hat{\epsilon} \tilde{\zeta}_\chi^{(1)} + \hat{\epsilon}^2 \tilde{\zeta}_\chi^{(2)} \right) \\ &\quad \left. + \hat{\epsilon} \left( \tilde{\Phi}_\xi^{(0)} + \hat{\epsilon} \tilde{\Phi}_\xi^{(1)} + \hat{\epsilon}^2 \tilde{\Phi}_\xi^{(2)} + \hat{\epsilon} \left( \tilde{\Phi}_\chi^{(0)} + \hat{\epsilon} \tilde{\Phi}_\chi^{(1)} + \hat{\epsilon}^2 \tilde{\Phi}_\chi^{(2)} \right) \right) \right. \\ &\quad \cdot \left. \left( \tilde{\zeta}_\xi^{(0)} + \hat{\epsilon} \tilde{\zeta}_\xi^{(1)} + \hat{\epsilon}^2 \tilde{\zeta}_\xi^{(2)} + \hat{\epsilon} \left( \tilde{\zeta}_\chi^{(0)} + \hat{\epsilon} \tilde{\zeta}_\chi^{(1)} + \hat{\epsilon}^2 \tilde{\zeta}_\chi^{(2)} \right) \right) \right] \end{aligned} \quad (\text{B.10})$$

### Dynamic Boundary Condition

$$\begin{aligned} \tilde{\zeta}^{(0)} + \hat{\epsilon} \tilde{\zeta}^{(1)} + \hat{\epsilon}^2 \tilde{\zeta}^{(2)} + \hat{\epsilon}^2 \left( \tilde{\Phi}_\tau^{(0)} + \hat{\epsilon} \tilde{\Phi}_\tau^{(1)} + \hat{\epsilon}^2 \tilde{\Phi}_\tau^{(2)} \right) \\ - C_p \left( \tilde{\Phi}_\xi^{(0)} + \hat{\epsilon} \tilde{\Phi}_\xi^{(1)} + \hat{\epsilon}^2 \tilde{\Phi}_\xi^{(2)} \right) - \hat{\epsilon} C_g \left( \tilde{\Phi}_\chi^{(0)} + \hat{\epsilon} \tilde{\Phi}_\chi^{(1)} + \hat{\epsilon}^2 \tilde{\Phi}_\chi^{(2)} \right) \\ + \frac{1}{2} \hat{\epsilon} \left[ \left( \tilde{\Phi}_\xi^{(0)} + \hat{\epsilon} \tilde{\Phi}_\xi^{(1)} + \hat{\epsilon}^2 \tilde{\Phi}_\xi^{(2)} + \hat{\epsilon} \left( \tilde{\Phi}_\chi^{(0)} + \hat{\epsilon} \tilde{\Phi}_\chi^{(1)} + \hat{\epsilon}^2 \tilde{\Phi}_\chi^{(2)} \right) \right)^2 \right. \\ \left. + \frac{1}{\delta^2} \left( \tilde{\Phi}_{\tilde{z}}^{(0)} + \hat{\epsilon} \tilde{\Phi}_{\tilde{z}}^{(1)} + \hat{\epsilon}^2 \tilde{\Phi}_{\tilde{z}}^{(2)} \right)^2 \right] = 0 \end{aligned} \quad (\text{B.11})$$

In addition, the boundary conditions at the unknown free surface  $\tilde{z} = \hat{\epsilon} \tilde{\zeta}(\xi, \chi, \tau)$  are simplified by Taylor series expansions about  $\tilde{z} = 0$ ,

$$f(\xi, \chi, \tilde{\zeta}, \tau) = \sum_{n=0}^{\infty} \frac{(\hat{\epsilon} \tilde{\zeta})^n}{n!} \frac{\partial^{(n)} f}{\partial \tilde{z}^{(n)}}|_0. \quad (\text{B.12})$$

Applying Eq. B.12 in the two surface boundary conditions (Eq. B.10 and Eq. B.11) and truncation at order  $\mathcal{O}(\hat{\epsilon}^{(2)})$  gives for  $\tilde{z} = 0$ :

### Kinematic Boundary Condition

$$\begin{aligned} \tilde{\Phi}_{\tilde{z}}^{(0)} + \hat{\epsilon} \tilde{\zeta}^{(0)} \tilde{\Phi}_{\tilde{z}\tilde{z}}^{(0)} + \hat{\epsilon}^2 \tilde{\zeta}^{(1)} \tilde{\Phi}_{\tilde{z}\tilde{z}}^{(0)} + \frac{1}{2} \hat{\epsilon}^2 (\tilde{\zeta}^{(0)})^2 \tilde{\Phi}_{\tilde{z}\tilde{z}\tilde{z}}^{(0)} + \hat{\epsilon} \tilde{\Phi}_{\tilde{z}}^{(1)} \\ + \hat{\epsilon}^2 \tilde{\zeta}^{(0)} \tilde{\Phi}_{\tilde{z}\tilde{z}}^{(1)} + \hat{\epsilon}^2 \tilde{\Phi}_{\tilde{z}}^{(2)} = \delta^2 \left[ \hat{\epsilon}^2 \tilde{\zeta}_\tau^{(0)} - C_p \tilde{\zeta}_\xi^{(0)} - C_p \hat{\epsilon} \tilde{\zeta}_\xi^{(1)} \right. \\ \left. - C_p \hat{\epsilon}^2 \tilde{\zeta}_\xi^{(2)} - C_g \hat{\epsilon} \tilde{\zeta}_\chi^{(0)} - C_g \hat{\epsilon}^2 \tilde{\zeta}_\chi^{(1)} + \hat{\epsilon} \tilde{\zeta}_\xi^{(0)} \tilde{\Phi}_\xi^{(0)} + \hat{\epsilon}^2 \tilde{\zeta}_\xi^{(1)} \tilde{\Phi}_\xi^{(0)} \right. \\ \left. + \hat{\epsilon}^2 \tilde{\zeta}_\chi^{(0)} \tilde{\Phi}_\xi^{(0)} + \hat{\epsilon}^2 \tilde{\zeta}^{(0)} \tilde{\zeta}_\xi^{(0)} \tilde{\Phi}_{\xi\tilde{z}}^{(0)} + \hat{\epsilon}^2 \tilde{\zeta}_\xi^{(0)} \tilde{\Phi}_\xi^{(1)} + \hat{\epsilon}^2 \tilde{\zeta}_\xi^{(0)} \tilde{\Phi}_\chi^{(0)} \right] \end{aligned} \quad (\text{B.13})$$

### Dynamic Boundary Condition

$$\begin{aligned} \tilde{\zeta}^{(0)} + \hat{\epsilon} \tilde{\zeta}^{(1)} + \hat{\epsilon}^2 \tilde{\zeta}^{(2)} + \hat{\epsilon}^2 \tilde{\Phi}_\tau^{(0)} - C_p \left( \tilde{\Phi}_\xi^{(0)} + \hat{\epsilon} \tilde{\zeta}^{(0)} \tilde{\Phi}_{\xi\tilde{z}}^{(0)} \right. \\ \left. + \hat{\epsilon}^2 \tilde{\zeta}^{(1)} \tilde{\Phi}_{\xi\tilde{z}}^{(0)} + \frac{1}{2} \hat{\epsilon}^2 (\tilde{\zeta}^{(0)})^2 \tilde{\Phi}_{\xi\tilde{z}\tilde{z}}^{(0)} + \hat{\epsilon} \tilde{\Phi}_\xi^{(1)} + \hat{\epsilon}^2 \tilde{\zeta}^{(0)} \tilde{\Phi}_{\xi\tilde{z}}^{(1)} + \hat{\epsilon}^2 \tilde{\Phi}_\xi^{(2)} \right) \\ - C_g \left( \hat{\epsilon} \tilde{\Phi}_\chi^{(0)} + \hat{\epsilon}^2 \tilde{\zeta}^{(0)} \tilde{\Phi}_{\chi\tilde{z}}^{(0)} + \hat{\epsilon}^2 \tilde{\Phi}_\chi^{(1)} \right) + \frac{1}{2} \hat{\epsilon} \left( \tilde{\Phi}_\xi^{(0)} \right)^2 \\ + \hat{\epsilon}^2 \tilde{\Phi}_\xi^{(0)} \left( \tilde{\zeta}^{(0)} \tilde{\Phi}_{\xi\tilde{z}}^{(0)} + \tilde{\Phi}_\xi^{(1)} + \tilde{\Phi}_\chi^{(0)} \right) \\ + \frac{1}{\delta^2} \tilde{\Phi}_{\tilde{z}}^{(0)} \left( \frac{1}{2} \hat{\epsilon} \tilde{\Phi}_{\tilde{z}}^{(0)} + \hat{\epsilon}^2 \tilde{\zeta}^{(0)} \tilde{\Phi}_{\tilde{z}\tilde{z}}^{(0)} + \hat{\epsilon}^2 \tilde{\Phi}_{\tilde{z}}^{(1)} \right) = 0 \end{aligned} \quad (\text{B.14})$$

The above boundary value problem can be separated into the different orders  $\mathcal{O}(\hat{\epsilon}^{(n)})$  and solved sequentially from the lowest order to the highest order. The procedure for solving the boundary value problem is similar at each order. At the beginning ansatz functions are defined and introduced into the Laplace equation and bottom boundary condition resulting in general solutions for the boundary value problem. Afterwards, this general solutions are introduced into the surface boundary conditions to determine the exact solution (for each order).

The leading order problem ( $\mathcal{O}(\hat{\epsilon}^{(0)})$ ) summarizes as:

Laplace equation

$$\tilde{\Phi}_{\tilde{z}\tilde{z}}^{(0)} + \delta^2 \tilde{\Phi}_{\xi\xi}^{(0)} = 0 \quad (\text{B.15})$$

Kinematic Boundary Condition ( $\tilde{z} = 0$ )

$$\tilde{\Phi}_{\tilde{z}}^{(0)} = -\delta^2 C_p \tilde{\zeta}_\xi^{(0)} \quad (\text{B.16})$$

Dynamic Boundary Conditions ( $\tilde{z} = 0$ )

$$\tilde{\zeta}^{(0)} - C_p \tilde{\Phi}_\xi^{(0)} = 0 \quad (\text{B.17})$$

Bottom Boundary Condition ( $\tilde{z} = -1$ )

$$\tilde{\Phi}_{0\tilde{z}} = 0 \quad (\text{B.18})$$

The following functions are introduced in order to determine the leading order solution,

$$\tilde{\zeta}^{(0)} = A^{(0)} E + \text{c.c.}, \quad \tilde{\Phi}^{(0)} = f^{(0)} + F^{(0)} E + \text{c.c.}, \quad (\text{B.19})$$

with  $E = e^{ik\xi}$ ,  $A^{(0)} = A^{(0)}(\chi, \tau)$ ,  $F^{(0)} = F^{(0)}(z, \chi, \tau)$ ,  $f^{(0)} = f^{(0)}(\chi, \tau)$  and c.c. denotes the complex conjugate. The term  $f^{(0)}(\chi, \tau)$  represents the mean drift component. Insertion of Eq. B.19 in Eq. B.15 results in

$$F_{\tilde{z}\tilde{z}}^{(0)} E^1 + F_{\tilde{z}\tilde{z}}^{*(0)} E^{-1} - \delta^2 k^2 (F^{(0)} E^1 + F^{*(0)} E^{-1}) = 0, \quad (\text{B.20})$$

where asterisk denote the complex conjugate. Separating the  $E^1$  and  $E^{-1}$  terms yields for  $E^1$  (Eq. B.20)

$$E^1 : F_{\tilde{z}\tilde{z}}^{(0)} - \delta^2 k^2 F^{(0)} = 0, \quad (\text{B.21})$$

which is fulfilled with the following function

$$F^{(0)} = G^{(0)}(\chi, \tau) \cosh(\delta k(\tilde{z} + 1)), \quad (\text{B.22})$$

satisfying the bottom boundary condition (Eq. B.18). Insertion of Eq. B.19 and Eq. B.22 into the two surface boundary conditions (Eqs. B.16 & B.17,  $\tilde{z} = 0$ ) yield

$$\begin{aligned} \delta k G^{(0)} \sinh(\delta k) E^1 + \delta k G^{*(0)} \sinh(\delta k) E^{-1} = \\ - ik \delta^2 C_p (A^{(0)} E^1 - A^{*(0)} E^{-1}) \end{aligned} \quad (\text{B.23})$$

---

and

$$C_p \left( ikG^{(0)} \cosh(\delta k) E^1 - ikG^{*(0)} \cosh(\delta k) E^{-1} \right) = A^{(0)} E^1 + A^{(0)} E^{-1}. \quad (\text{B.24})$$

Again, separating the  $E^1$  term results in:

Kinematic Boundary Condition

$$E^1 : \delta k G^{(0)} \sinh(\delta k) = -ik\delta^2 C_p A^{(0)} \quad (\text{B.25})$$

Dynamic Boundary Condition

$$E^1 : ikC_p G^{(0)} \cosh(\delta k) = A^{(0)}, \quad (\text{B.26})$$

from which  $C_p$  and  $G^{(0)}$  can be determined

$$G^{(0)} = -\frac{iA^{(0)}}{kC_p} \operatorname{sech}(\delta k); \quad C_p^2 = \frac{\tanh(\delta k)}{\delta k} \quad (\text{B.27})$$

resulting in

$$F^{(0)} = -i\delta C_p A^{(0)} \frac{\cosh(\delta k(z+1))}{\sinh(\delta k)}. \quad (\text{B.28})$$

So far, the amplitude function  $A^{(0)}$  is unknown and the next step is to proceed with the next order ( $\mathcal{O}(\hat{\epsilon})$ ).

The  $\mathcal{O}(\hat{\epsilon})$  order problem is:

Laplace equation

$$\tilde{\Phi}_{\tilde{z}\tilde{z}}^{(1)} + \delta^2 \left[ \tilde{\Phi}_{\xi\xi}^{(1)} + 2\tilde{\Phi}_{\xi\chi}^{(0)} \right] = 0 \quad (\text{B.29})$$

Kinematic Boundary Condition ( $\tilde{z} = 0$ )

$$\tilde{\zeta}^{(0)} \tilde{\Phi}_{\tilde{z}\tilde{z}}^{(0)} + \tilde{\Phi}_{\tilde{z}}^{(1)} = \delta^2 \left[ -C_p \tilde{\zeta}_{\xi}^{(1)} - C_g \tilde{\zeta}_{\chi}^{(0)} + \tilde{\zeta}_{\xi}^{(0)} \tilde{\Phi}_{\xi}^{(0)} \right] \quad (\text{B.30})$$

Dynamic Boundary Conditions ( $\tilde{z} = 0$ )

$$\begin{aligned} \tilde{\zeta}^{(1)} - C_p \left( \tilde{\zeta}^{(0)} \tilde{\Phi}_{\xi\tilde{z}}^{(0)} + \tilde{\Phi}_{\xi}^{(1)} \right) - C_g \tilde{\Phi}_{\chi}^{(0)} + \\ \frac{1}{2} \left( \left( \tilde{\Phi}_{\xi}^{(0)} \right)^2 + \frac{1}{\delta^2} \left( \tilde{\Phi}_{\tilde{z}}^{(0)} \right)^2 \right) = 0 \end{aligned} \quad (\text{B.31})$$

Bottom Boundary Condition ( $\tilde{z} = -1$ )

$$\tilde{\Phi}_{1\tilde{z}} = 0 \quad (\text{B.32})$$

Based on the procedure presented above, it is clear that these equations will produce the additional terms  $E^2$ ,  $E^{-2}$  and  $E^0$  (from  $E^1 E^{-1}$ ). The terms  $E^2$  and  $E^{-2}$

(conjugate complex) are the first of the higher harmonics which are created by the non-linear interaction. The fundamental term  $E^1$  (with  $E^{-1}$ ) is already introduced (Eq. B.19). The term  $E^0$  is not a harmonic (oscillatory) function, but does not destroy the periodicity in  $\xi$  (Johnson, 1997).

For the higher-order problem the following periodic structures are introduced

$$\tilde{\Phi}^{(n)} = \sum_{m=0}^{n+1} F_m^{(n)} E^m + c.c.; \quad \zeta^{(n)} = \sum_{m=0}^{n+1} A_m^{(n)} E^m + c.c. \quad (\text{B.33})$$

where  $F_m^{(n)}$  and  $A_m^{(n)}$  are to be determined and  $m$  represents the harmonic component. From Eq. B.33 follows

$$\begin{aligned} \tilde{\Phi}^{(1)} &= F_0^{(1)} E^0 + F_1^{(1)} E^1 + F_1^{*(1)} E^{-1} + F_2^{(1)} E^2 + F_2^{*(1)} E^{-2}, \\ \zeta^{(1)} &= A_0^{(1)} E^0 + A_1^{(1)} E^1 + A_1^{*(1)} E^{-1} + A_2^{(1)} E^2 + A_2^{*(1)} E^{-2}. \end{aligned} \quad (\text{B.34})$$

Insertion of Eqs. B.34 in the Laplace equation (B.29) results in

$$\begin{aligned} F_{0\bar{z}\bar{z}}^{(1)} E^0 + F_{1\bar{z}\bar{z}}^{(1)} E^1 + F_{1\bar{z}\bar{z}}^{*(1)} E^{-1} + F_{2\bar{z}\bar{z}}^{(1)} E^2 + F_{2\bar{z}\bar{z}}^{*(1)} E^{-2} \\ - \delta^2 \left[ k^2 \left( F_1^{(1)} E^1 + F_1^{*(1)} E^{-1} + 4F_2^{(1)} E^2 + 4F_2^{*(1)} E^{-2} \right) \right. \\ \left. + 2ik \left( F_\chi^{(0)} E^1 - F_\chi^{*(0)} E^{-1} \right) \right] = 0. \end{aligned} \quad (\text{B.35})$$

Separation of the  $E^{(n)}$  terms gives:

$$\begin{aligned} E^0 : \quad F_{0\bar{z}\bar{z}}^{(1)} &= 0, \\ E^1 : \quad F_{1\bar{z}\bar{z}}^{(1)} - \delta^2 k^2 F_1^{(1)} + 2i\delta^2 k F_\chi^{(0)} &= 0, \\ E^2 : \quad F_{2\bar{z}\bar{z}}^{(1)} - 4\delta^2 k^2 F_2^{(1)} &= 0. \end{aligned} \quad (\text{B.36})$$

General solutions for these equations, satisfying the bottom boundary condition (Eq. B.32), are

$$\begin{aligned} F_0^{(1)} &= G_0^{(1)}, \quad F_2^{(1)} = G_2^{(1)} \cosh(2\delta k(z+1)) \\ F_1^{(1)} &= G_1^{(1)} \cosh(\delta k(z+1)) - i\delta G_\chi^{(0)}(z+1) \sinh(\delta k(z+1)). \end{aligned} \quad (\text{B.37})$$

At this stage  $G_m^{(1)}$  are arbitrary functions. The results are now incorporated into the two surface boundary conditions (Eq. B.30 and Eq. B.31),

Kinematic Boundary Condition:

$$\begin{aligned} &A^{(0)} F_{\bar{z}\bar{z}}^{(0)} E^2 + A^{(0)} F_{\bar{z}\bar{z}}^{*(0)} + A^{*(0)} F_{\bar{z}\bar{z}}^{(0)} + A^{*(0)} F_{\bar{z}\bar{z}}^{*(0)} E^{-2} \\ &+ F_{1\bar{z}}^{(1)} E^1 + F_{1\bar{z}}^{*(1)} E^{-1} + F_{2\bar{z}}^{(1)} E^2 + F_{2\bar{z}}^{*(1)} E^{-2} \\ &= \delta^2 \left[ -ikC_p \left( A_1^{(1)} E^1 - A_1^{*(1)} E^{-1} + A_2^{(1)} E^2 - A_2^{*(1)} E^{-2} \right) \right. \\ &\left. - C_g \left( A_\chi^{(0)} E^1 + A_\chi^{*(0)} E^{-1} \right) + k^2 \left( -A^{(0)} F^{(0)} E^2 + A^{(0)} F^{*(0)} \right. \right. \\ &\left. \left. + A^{*(0)} F^{(0)} - A^{*(0)} F^{*(0)} E^{-2} \right) \right] \end{aligned} \quad (\text{B.38})$$

---

Dynamic Boundary Condition:

$$\begin{aligned}
& A_0^{(1)} + A_1^{(1)} E^1 + A_1^{*(1)} E^{-1} + A_2^{(1)} E^2 + A_2^{*(1)} E^{-2} \\
& - ikC_p \left( A^{(0)} F_{\tilde{z}}^{(0)} E^2 - A^{(0)} F_{\tilde{z}}^{*(0)} + A^{*(0)} F_{\tilde{z}}^{(0)} \right. \\
& \left. - A^{*(0)} F_{\tilde{z}}^{*(0)} E^{-2} \right) - ikC_p \left( F_1^{(1)} E^1 - F_1^{*(1)} E^{-1} + 2F_2^{(1)} E^2 \right. \\
& \left. - 2F_2^{*(1)} E^{-2} \right) - C_g \left( f_\chi^{(0)} + F_\chi^{(0)} E^1 + F_\chi^{*(0)} E^{-1} \right) \\
& + \frac{1}{2} \left[ -k^2 \left( F^{(0)} \right)^2 E^2 + 2k^2 F^{(0)} F^{*(0)} - k^2 \left( F^{*(0)} \right)^2 E^{-2} \right. \\
& \left. + \frac{1}{\delta^2} \left( \left( F_{\tilde{z}}^{(0)} \right)^2 E^2 + 2F_{\tilde{z}}^{(0)} F_{\tilde{z}}^{*(0)} + \left( F_{\tilde{z}}^{*(0)} \right)^2 E^{-2} \right) \right] = 0
\end{aligned} \tag{B.39}$$

Separating the different  $E^{(n)}$  terms and inserting the corresponding  $F_m^{(n)}$  (Eq. B.22 and B.37) and its derivatives, respectively, results in six equations for the two boundary conditions:

Dynamic Boundary Condition

$$\begin{aligned}
E^0 : & \delta^2 k^2 \left( A^{(0)} G^{*(0)} + A^{*(0)} G^{(0)} \right) \cosh(\delta k) \\
& = \delta^2 k^2 \left( A^{(0)} G^{*(0)} + A^{*(0)} G^{(0)} \right) \cosh(\delta k)
\end{aligned} \tag{B.40}$$

$$\begin{aligned}
E^1 : & \delta k G_1^{(1)} \sinh(\delta k) - i\delta G_\chi^{(0)} (\sinh(\delta k) - \delta k \cosh(\delta k)) \\
& = -i\delta^2 k C_p A_1^{(1)} - \delta^2 C_g A_\chi^{(0)}
\end{aligned} \tag{B.41}$$

$$\begin{aligned}
E^2 : & \delta^2 k^2 A^{(0)} G^{(0)} \cosh(\delta k) + 2\delta k G_2^{(1)} \sinh(2\delta k) \\
& = -2i\delta^2 k C_p A_2^{(1)} - \delta^2 k^2 A^{(0)} G^{(0)} \cosh(\delta k)
\end{aligned} \tag{B.42}$$

Kinematic Boundary Condition

$$\begin{aligned}
E^0 : & A_0^{(1)} + i\delta k^2 C_p \left( A^{(0)} G^{*(0)} - A^{*(0)} G^{(0)} \right) \sinh(\delta k) \\
& - C_g f_\chi^{(0)} + k^2 G^{(0)} G^{*(0)} \left( \cosh^2(\delta k) + \sinh^2(\delta k) \right) = 0
\end{aligned} \tag{B.43}$$

$$\begin{aligned}
E^1 : & -C_g G_\chi^{(0)} \cosh(\delta k) - ikC_p \left( G_1^{(1)} \cosh(\delta k) \right. \\
& \left. - i\delta G_\chi^{(0)} \sinh(\delta k) \right) + A_1^{(1)} = 0
\end{aligned} \tag{B.44}$$

$$\begin{aligned}
E^2 : & -ikC_p \left( 2G_2^{(1)} \cosh(2\delta k) + \delta k A^{(0)} G^{(0)} \sinh(\delta k) \right) \\
& + A_2^{(1)} - \frac{1}{2} k^2 (G^{(0)})^2 = 0.
\end{aligned} \tag{B.45}$$

Equation B.40 is identically satisfied and from Eqs. B.43 & B.44 follows directly

$$A_0^{(1)} = -\frac{2\delta k}{\sinh(2\delta k)} A^{(0)} A^{*(0)} + C_g f_\chi^{(0)} \quad (\text{B.46})$$

and

$$\begin{aligned} A_1^{(1)} = & C_g G_\chi^{(0)} \cosh(\delta k) \\ & + ikC_p \left( G_1^{(1)} \cosh(\delta k) - i\delta G_\chi^{(0)} \sinh(\delta k) \right). \end{aligned} \quad (\text{B.47})$$

Invoking Eq. B.47 in Eq. B.41 yields that  $G_1^{(1)}$  cancels identically and that  $A_\chi^{(0)}$  ( $\neq 0$ ) cancels also. At the end, the group speed for gravity waves is obtained,

$$C_g = \frac{1}{2} C_p (1 + 2\delta k \operatorname{cosech}(2\delta k)) \quad (\text{B.48})$$

Finally,  $G_2^{(1)}$  (Eq. B.42) and  $A_2^{(1)}$  (Eq. B.45) are solved resulting in

$$G_2^{(1)} = -\frac{3i}{4} \frac{\delta^2 k C_p (A^{(0)})^2}{\sinh^4(\delta k)} \quad (\text{B.49})$$

and

$$A_2^{(1)} = \frac{\delta k \cosh(\delta k)}{2 \sinh^3(\delta k)} (2 \cosh^2(\delta k) + 1) (A^{(0)})^2. \quad (\text{B.50})$$

The amplitude function  $A^{(0)}(\chi, \tau)$  is still undetermined. Thus, the next step is to deduce the  $\mathcal{O}(\hat{\epsilon}^{(2)})$  order and to determine the equation for  $A^{(0)}(\chi, \tau)$ .

The  $\mathcal{O}(\hat{\epsilon}^{(2)})$  order problem is:

Laplace equation

$$\tilde{\Phi}_{\tilde{z}\tilde{z}}^{(2)} + \delta^2 \tilde{\Phi}_{\xi\xi}^{(2)} + 2\delta^2 \tilde{\Phi}_{\xi\chi}^{(1)} + \delta^2 \tilde{\Phi}_{\chi\chi}^{(0)} = 0 \quad (\text{B.51})$$

Kinematic Boundary Condition ( $\tilde{z} = 0$ )

$$\begin{aligned} \tilde{\zeta}^{(1)} \tilde{\Phi}_{\tilde{z}\tilde{z}}^{(0)} + \frac{1}{2} (\tilde{\zeta}^{(0)})^2 \tilde{\Phi}_{\tilde{z}\tilde{z}\tilde{z}}^{(0)} + \tilde{\zeta}^{(0)} \tilde{\Phi}_{\tilde{z}\tilde{z}}^{(1)} + \tilde{\Phi}_{\tilde{z}}^{(2)} \\ = \delta^2 \left[ \tilde{\zeta}_\tau^{(0)} - C_p \tilde{\zeta}_\xi^{(2)} - C_g \tilde{\zeta}_\chi^{(1)} + \tilde{\Phi}_\xi^{(0)} \left( \tilde{\zeta}_\xi^{(1)} + \tilde{\zeta}_\chi^{(0)} \right) \right. \\ \left. + \tilde{\zeta}_\xi^{(0)} \left( \tilde{\zeta}^{(0)} \tilde{\Phi}_{\xi\tilde{z}}^{(0)} + \tilde{\Phi}_\xi^{(1)} + \tilde{\Phi}_\chi^{(0)} \right) \right] \end{aligned} \quad (\text{B.52})$$

Dynamic Boundary Conditions ( $\tilde{z} = 0$ )

$$\begin{aligned} \tilde{\zeta}^{(2)} + \tilde{\Phi}_\tau^{(0)} - C_p \left( \tilde{\zeta}^{(1)} \tilde{\Phi}_{\xi\tilde{z}}^{(0)} + \frac{1}{2} (\tilde{\zeta}^{(0)})^2 \tilde{\Phi}_{\xi\tilde{z}\tilde{z}}^{(0)} + \tilde{\zeta}^{(0)} \tilde{\Phi}_{\xi\tilde{z}}^{(1)} \right. \\ \left. + \tilde{\Phi}_\xi^{(2)} \right) - C_g \left( \tilde{\zeta}^{(0)} \tilde{\Phi}_{\chi\tilde{z}}^{(0)} + \tilde{\Phi}_\chi^{(1)} \right) + \tilde{\Phi}_\xi^{(0)} \left( \tilde{\zeta}^{(0)} \tilde{\Phi}_{\xi\tilde{z}}^{(0)} + \tilde{\Phi}_\xi^{(1)} \right. \\ \left. + \tilde{\Phi}_\chi^{(0)} \right) + \frac{1}{\delta^2} \tilde{\Phi}_{\tilde{z}}^{(0)} \left( \tilde{\zeta}^{(0)} \tilde{\Phi}_{\tilde{z}\tilde{z}}^{(0)} + \tilde{\Phi}_{\tilde{z}}^{(1)} \right) = 0 \end{aligned} \quad (\text{B.53})$$

---

Bottom Boundary Condition ( $\tilde{z} = -1$ )

$$\tilde{\Phi}_{2\tilde{z}} = 0 \quad (\text{B.54})$$

The periodic functions (Eq. B.33) are now used for  $n = 2$ , whereby the higher harmonic  $E^3$  term appears for the first time. From Eq. B.33 follows

$$\begin{aligned} \tilde{\Phi}^{(2)} = F_0^{(2)}E^0 + F_1^{(2)}E^1 + F_1^{*(2)}E^{-1} + F_2^{(2)}E^2 + F_2^{*(2)}E^{-2} \\ + F_3^{(2)}E^3 + F_3^{*(2)}E^{-3} \end{aligned} \quad (\text{B.55})$$

and

$$\begin{aligned} \zeta^{(2)} = A_0^{(2)}E^0 + A_1^{(2)}E^1 + A_1^{*(2)}E^{-1} + A_2^{(2)}E^2 + A_2^{*(2)}E^{-2} \\ + A_3^{(2)}E^3 + A_3^{*(2)}E^{-3}. \end{aligned} \quad (\text{B.56})$$

Insertion of Eq. B.55 and Eq. B.56 in the Laplace equation (B.51) results in

$$\begin{aligned} & F_{0\tilde{z}\tilde{z}}^{(2)}E^0 + F_{1\tilde{z}\tilde{z}}^{(2)}E^1 + F_{1\tilde{z}\tilde{z}}^{*(2)}E^{-1} + F_{2\tilde{z}\tilde{z}}^{(2)}E^2 + F_{2\tilde{z}\tilde{z}}^{*(2)}E^{-2} \\ & + F_{3\tilde{z}\tilde{z}}^{(2)}E^3 + F_{3\tilde{z}\tilde{z}}^{*(2)}E^{-3} + \delta^2 \left( -k^2 F_1^{(2)}E^1 - k^2 F_1^{*(2)}E^{-1} \right. \\ & \left. - 4k^2 F_2^{(2)}E^2 - 4k^2 F_2^{*(2)}E^{-2} - 9k^2 F_3^{(2)}E^3 - 9k^2 F_3^{*(2)}E^{-3} \right) \\ & + 2\delta^2 \left( ikF_{1\chi}^{(1)}E^1 - ikF_{1\chi}^{*(1)}E^{-1} + 2ikF_{2\chi}^{(1)}E^2 - 2ikF_{2\chi}^{*(1)}E^{-2} \right) \\ & + \delta^2 \left( f_{\chi\chi}^{(0)} + F_{\chi\chi}^{(0)}E^1 + F_{\chi\chi}^{(0)}E^{-1} \right) = 0. \end{aligned} \quad (\text{B.57})$$

Separation of the  $E^{(n)}$  terms yields:

$$\begin{aligned} E^0 : & F_{0\tilde{z}\tilde{z}}^{(2)} + \delta^2 f_{\chi\chi}^{(0)} = 0, \\ E^1 : & F_{1\tilde{z}\tilde{z}}^{(2)} - \delta^2 k^2 F_1^{(2)} + 2i\delta^2 k F_{1\chi}^{(1)} + \delta^2 F_{\chi\chi}^{(0)} = 0, \\ E^2 : & F_{2\tilde{z}\tilde{z}}^{(2)} - 4\delta^2 k^2 F_2^{(2)} + 4i\delta^2 k F_{2\chi}^{(1)} = 0, \\ E^3 : & F_{3\tilde{z}\tilde{z}}^{(2)} - 9\delta^2 k^2 F_3^{(2)} = 0. \end{aligned} \quad (\text{B.58})$$

The target of this derivation is to arrive at a equation for  $A^{(0)}$ , which “appears at this stage from the terms that arises at  $E^1$ ” (Johnson, 1997). Hence, only the  $E^1$  terms are examined in detail in the following. The solution for  $F_1^{(2)}$  (Eq. B.58), satisfying the bottom boundary condition (Eq. B.54), reads (Johnson, 1997)

$$\begin{aligned} F_1^{(2)} = & G_1^{(2)} \cosh(\delta k(z+1)) \\ & - \left( i\delta G_{1\chi}^{(1)} + \frac{\delta}{2k} G_{\chi\chi}^{(0)} \right) (z+1) \sinh(\delta k(z+1)) \\ & + \frac{1}{2} \delta^2 G_{\chi\chi}^{(0)} \left( \frac{1}{\delta k} (z+1) \sinh(\delta k(z+1)) \right. \\ & \left. - (z+1)^2 \cosh(\delta k(z+1)) \right). \end{aligned} \quad (\text{B.59})$$

This result is now incorporated into the two surface boundary conditions (Eqs. B.52 & B.53) and separated only for the  $E^1$  term resulting in two equations,

$$\begin{aligned} F_{1\bar{z}}^{(2)} + A^{*(0)}F_{2\bar{z}\bar{z}}^{(1)} + \frac{1}{2} \left( (A^{(0)})^2 F_{\bar{z}\bar{z}\bar{z}}^{*(0)} + 2A^{(0)}A^{*(0)}F_{\bar{z}\bar{z}\bar{z}}^{(0)} \right) \\ + A_0^{(1)}F_{\bar{z}\bar{z}}^{(0)} + A_2^{(1)}F_{\bar{z}\bar{z}}^{*(0)} = \delta^2 \left[ A_\tau^{(0)} - C_g A_{1\chi}^{(1)} - ikC_p A_1^{(2)} \right. \\ \left. + 2k^2 A_2^{(1)}F^{*(0)} - k^2 A^{(0)} \left( A^{*(0)}F_{\bar{z}}^{(0)} - A^{(0)}F_{\bar{z}}^{*(0)} \right) \right. \\ \left. + k^2 A^{*(0)} \left( A^{(0)}F_{\bar{z}}^{(0)} + 2F_2^{(1)} \right) \right] \end{aligned} \quad (\text{B.60})$$

and

$$\begin{aligned} F_\tau^{(0)} - C_g F_{1\chi}^{(1)} - ikC_p F_1^{(2)} - 2ikC_p A^{*(0)}F_{2\bar{z}}^{(1)} \\ - ikC_p \left( A_0^{(1)}F_{\bar{z}}^{(0)} - A_2^{(1)}F_{\bar{z}}^{*(0)} \right) - \frac{1}{2}ikC_p \left( 2A^{(0)}A^{*(0)}F_{\bar{z}\bar{z}}^{(0)} \right. \\ \left. - (A^{(0)})^2 F_{\bar{z}\bar{z}}^{*(0)} \right) + A_1^{(2)} + \frac{1}{\delta^2} \left[ \left( A^{(0)}F_{\bar{z}\bar{z}}^{*(0)} + A^{*(0)}F_{\bar{z}\bar{z}}^{(0)} \right) F_{\bar{z}}^{(0)} \right. \\ \left. + \left( A^{(0)}F_{\bar{z}\bar{z}}^{(0)} + F_{2\bar{z}}^{(1)} \right) F_{\bar{z}}^{*(0)} \right] - k^2 \left( A^{*(0)}F_{\bar{z}}^{(0)} \right. \\ \left. - A^{(0)}F_{\bar{z}}^{*(0)} \right) F^{(0)} + k^2 \left( A^{(0)}F_{\bar{z}}^{(0)} + 2F_2^{(1)} \right) F^{*(0)} = 0. \end{aligned} \quad (\text{B.61})$$

The following steps are to be performed to obtain the equation for  $A^{(0)}(\chi, \tau)$ ,

- eliminate  $A_2^{(1)}$  between Eqs B.60 and Eq. B.61
- introduction and simplification of the already identified functions
- introduction of  $C_p$  (Eq. B.27) and  $C_g$  (Eq. B.48) whereby  $G_1^{(2)}$  and  $A_1^{(1)}$  cancels,

which results in the Non-linear Schrödinger-type equation,

$$-2ikC_p A_\tau^{(0)} + \hat{\alpha} A_{\chi\chi}^{(0)} + \hat{\beta} A^{(0)} |A^{(0)}|^2 = 0, \quad (\text{B.62})$$

for finite depth and moving coordinate system. Eq. 2.25 is obtained by retransforming Eq. B.62 to its dimensional form applying Eq. B.2 and Eq. B.5.